Doctoral Dissertation

Conversion of Biomass Waste into Functional Carbon Materials for Sustainable Energy Applications

持続可能なエネルギー利用のためのバイオマス廃棄物の機能性炭素材料への変換

FREDINA DESTYORINI

October 2023

Research Center for Advanced Materials

National Research and Innovation Agency (BRIN)

Table of Contents

General Introduction

Fossil fuels (coal, petroleum, and natural gas) play a dominant role in global energy systems with several adverse impacts in producing carbon dioxide and the largest driving in global climate change. With the increasing energy crisis and the threat of global warming are driving high demand for clean and renewable energy technologies with sustainable methods. Energy conversion and storage technologies taking into account the sustainability aspect, become more essential to overcome these issues. Sustainable energy, including considerations of environmental aspects has been attracting researchers to reduce carbon emissions and fossil fuel pollutions by considering renewable energy sources such as solar energy, wind power, hydroelectric power, etc. Among these technologies, fuel cells and batteries have emerged as key players in the transition to a sustainable energy future. Fuel cells are promising alternative energy converting devices on account of their high efficiency and low pollutant emission that electrochemically convert chemical energy of fuel i.e., hydrogen and oxygen gaseous resources into electrical power. Additionally, batteries enable efficient storage of energy in chemical form, allowing for its controlled release as electricity when needed.

In electrochemical energy conversion and storage such as battery and fuel cell, electrode is widely recognized as component that plays a crucial role in energy mechanism conversion. However, issues related to nonrenewable fossil-based materials, high costs, low yields, complex manufacturing processes, and high energy consumption are key considerations for energy sustainability and environmental impact perspectives. In order to make a significant contribution to renewable energy conversion and storage technology, it is important to develop alternative electrode materials from "sustainable resources" using a cheap and simple synthesis approach.

Fuel cell technology offers a feasible alternative to combustion-based power generation. One of the most widely studied and commercially viable types of fuel cells is the Proton exchange membrane fuel cells (PEMFCs) [1]. PEMFCs are an ideal candidate energy source unit for a wide range of stationary and mobile applications due to their high efficiency (about 40–50%, compared with 20–30% for the combustion engine), high power density, lightweight, simple structure, and fast start-up [2]. PEMFCs operate on the principle of electrochemical reactions, where hydrogen fuel is oxidized at the anode and oxygen from the air is reduced at the cathode, generating electricity and water as the only byproduct [3] (**Figure 1**). The electrode component that plays an important role is the gas diffusion layer (GDL), which facilitates the transport of reactant gases and ensures efficient reaction kinetics. GDL acts as a porous medium, enabling the uniform distribution of reactant gases across the electrode surface and providing electrical conductivity. It also plays a crucial role in water management and humidity balance to achieve good water transport in the system [4]. Commercially available GDLs are generally woven carbon cloth, felt or fiber-based carbon paper. However, the current production of commercial GDLs predominantly relies on polyacrylonitrile (PAN)-based materials, which are derived from a petroleum-based precursor material [5,6]. This dependence on non-renewable fossil fuel-derived PAN raises concerns regarding resource depletion and environmental sustainability. Moreover, PAN is an expensive base material (>$10/kg) [7], and to produce carbon fiber mats of GDL with proper porosity, hydrophobicity, and conductivity requires a complex production process [4,8] including high-temperature graphitization (>2500 °C) and multiple advanced treatments [9,10], makes it costly and time-consuming.

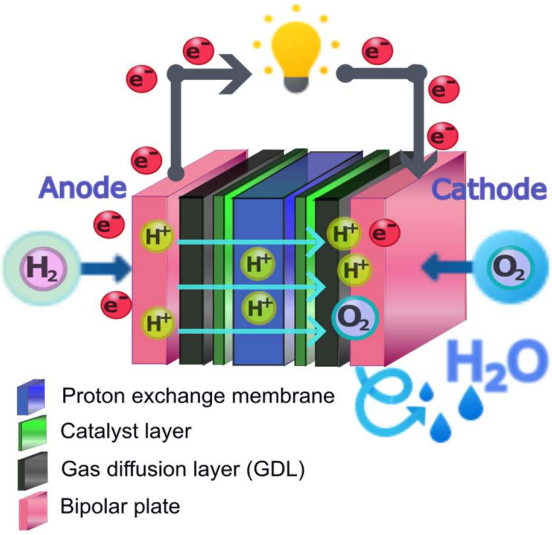

Figure 1. Schematic illustration of main components of PEMFC

Lithium-ion batteries (LIBs) are the most popular battery technology that uses lithium-ion as a key component of its electrochemistry. A LIB consists of a negative electrode (anode), positive electrode (cathode), separator, electrolyte, and two current collectors (positive and negative), as shown in **Figure 2**. During discharging of a battery, the anode releases lithium-ions to the cathode, generating a flow of electrons from one side to the other, and, while in charging mode, the opposite happens: lithium-ions are released by the cathode and received by the anode [11]. These batteries offer high energy density, longer cycle life, and lightweight characteristics, making them the preferred choice a wide range of applications, from small electronic component of portable device such as cellular phones, laptops, and wearable devices to large-scale applications in electric vehicles (EVs) [12]. The rapid growth of the electronics industry, particularly in EVs and portable electronics, has led to an increased demand for LIBs [13,14]. This condition directly affects the increasing need for graphite as an active material for LIBs anode on the market. Graphite has remained one of the most commercially desirable anode materials for LIBs due to its reversibility for lithium-ion intercalation/deintercalation, low operation potential (~0.1 V vs Li/Li^+), small volume expansion rate, stable cycle life, and relatively high specific capacity (372 mA h/g) [15,16]. In fact, each lithium-ion battery requires

10-15 times more graphite than lithium itself. To meet the demand for the projected 12 million electric vehicles by 2025, approximately 900,000 tons of graphite will be necessary [17]. However, its manufacture uses nonrenewable fossil fuel-based raw materials, a complex process, and a high-temperature graphitization step (up to 3000 °C) [18] with high energy consumption, resulting in a high impact on climate change and the environment.

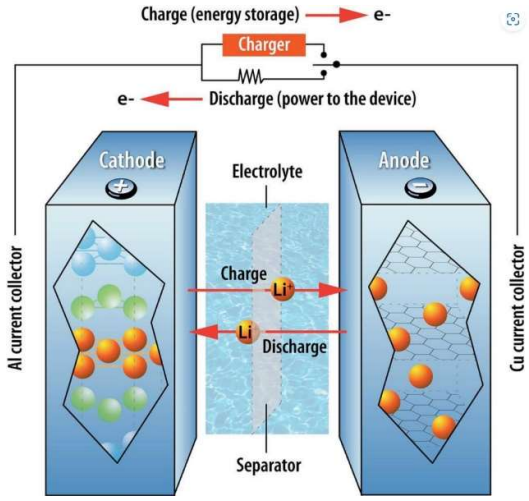

Figure 2. A schematic diagram showing how a lithium-ion battery works [12]

Taking into consideration the challenges that were previously outlined. Therefore, substantial efforts in research need to be made to reduce the environmental impact and the threat of global warming attributed to the fabrication of carbon paper for PEMFC electrodes and the production of graphite for LIB electrodes. This can be accomplished by making use of raw materials derived from low-cost and renewable carbon sources, as well as by developing production lines that are more straightforward and effective. This fabrication approach will not only promote environmental sustainability by utilizing renewable carbon sources but can also reduce the electrode production costs.

Global statistics indicate that an impressive 104.9 billion metric tons of carbon from biomass are generated each year [19]. Plant biomass is a widely recognized and abundant form of biomass, derived from the process of photosynthesis by converting carbon dioxide, water,

and solar energy into organic compounds. Indonesia as tropical country with a geographic location crossed by the equator, has an ideal climate for the growth of various species of plants. Indonesia is blessed with abundant and diverse plant biomass resources spread across its various islands. As reported by BPS-Statistics Indonesia in 2023, it has more than 125 million hectares of forest area and 12.8 million hectares of agricultural land, offering an enormous potential for renewable plant biomass resources [20]. In addition to forest products providing a profitable source of wood and other organic matter, the agricultural sector also contributes significantly to biomass production with commodities such as oil palm, sugarcane, rice, maize, tea, coffee, rubber, and coconut.

Figure 3. Map of the distribution of Indonesian coconut plantations (according to the Directorate General of Plantations report in 2022[21]) and coconut coir waste that is piled up openly.

Indonesia, as one of the largest coconut-producing country, produced approximately 2.9 million tons of coconuts in 2022[21] from plantations spread over several of its islands (**Figure**

3). Coconut *(Cocos nucifera*) is a fairly large Indonesia's export commodity which a significant contribution to the national economy. Consequently, the national coconut industry produces a lot of agricultural waste that has not been utilized optimally. Coconut coir is one of the waste products from around 35% of the coconut fruit, whereas in 2022, around one million tons of coconut coir waste are thrown away, burned, or left in open piles, resulting in environmental pollution [21], which unconsciously contributes greatly to global warming. Effective waste management practices are crucial to mitigate the negative impacts of such disposal methods. With the abundance of coconut coir waste, several industries use this waste as industrial raw material for various products such as mattresses and accessories, ropes, brooms, and crafts. Limited product development, limited functionality that are not able to reach a wider market has resulted in the undeveloped coconut coir industry to date as a main issue due to a lack of product innovation and processing technology.

Therefore, the utilization of coconut coir into useful and more innovative products is important to be carried out. Derived from the fibrous coating of the coconut fruit, coconut coir represents a lignocellulosic material primarily composed of cellulose, lignin, and hemicellulose. The degradation of lignocellulosic compounds occurs through a thermo-chemical process, resulting in the formation of solid carbon-rich charcoal [22,23]. Among these three lignocellulosic components, coconut coir contains the greatest proportion of lignin at 30-59.5%, followed by cellulose and hemicellulose at 15.7-36% and 5.4-22.5%, respectively [24–26]. These proportions provide a good starting point for generating carbon materials with porous and graphitic features, which are beneficial for their applications in the fields of energy conversion and storage.

Lignin, as an aromatic polymer composed of benzene rings in its building block, exhibits a high aromaticity and low oxygen content [27,28] that play a crucial role for graphite-like structures formation at high temperature with a high degree of graphitization [29]. High aromaticity of lignin provides an abundance of π electrons, enabling the formation of

delocalized bonds between carbon atoms. Additionally, planar and rigid structures of lignin promote easy stacking [30], which is fundamental for graphite-like structures development. Moreover, the low oxygen content of lignin reduces its polarity and reactivity, minimizing the introduction of defects and cross-linking that could hinder the formation of graphite-like structures. Furthermore, low oxygen content limits the presence of heteroatoms that could interfere with the crucial π bonding between carbon atoms, further promoting the development of graphite-like structures [31]. On the other hand, cellulose and hemicellulose contribute to the formation of porous structure on carbon products, due to a large amount of oxygen-containing functional groups. During heat treatment these oxygen-containing functional groups, such as hydroxyl and carbonyl groups tend to be eliminated as H_2O, CO_2, and CO resulting in three-dimensional and interconnect structures on solid carbon products [29,32].

In the process of converting biomass into functional carbon materials, an appropriate technique is needed to produce biomass-based functional carbon materials with beneficial characteristics for various applications. At an early stage, biomass feedstock can be converted into solid residue with high carbon content through carbonization processes including pyrolysis, gasification and hydrothermal carbonization [33]. Among these methods, pyrolysis stands out due to its simplicity, efficiency, and sustainability [5]. Pyrolysis is a thermochemical process that involves the decomposition of materials through heating in the absence of oxygen. Compared to hydrothermal carbonization, pyrolysis offers distinct advantages. For instance, eliminating the need for water during its process results in significant energy and cost savings in solid-liquid separation and waste-water treatment processes. Additionally, pyrolysis is capable of producing higher porosity and surface area compared to hydrothermal carbonization [34]. Properties of carbon materials obtained through pyrolysis can be finely tuned by adjusting factors such as temperature, reaction time, and the incorporation of additives.

Therefore, a series of biomass conversion strategies in this dissertation uses pyrolysis to produce functional carbon materials. In addition, further exploration and innovation on biomass conversion is still needed to further improve the performance and characteristics of the functional carbon materials. The continuous improvement of performance and characteristics is essential to generate innovation and deliver outstanding carbon performance, especially in energy conversion and storage systems.

Contents of dissertation

In the aforementioned background, this dissertation focuses on developing effective methods for converting coconut coir waste into functional carbon materials for energy conversion and storage fields. A cost-effective synthesis technology approach to efficiently convert Indonesia's biomass waste, underutilized coconut coir waste, into high-value products will be presented. First, solid carbon produced from a simple direct pyrolysis process of coconut coir as a porous and conductive carbon composite paper is applied to the catalytic support layer in the energy conversion devices of proton exchange membrane fuel cells (PEMFCs) (Chapter I). The chapter concerned the characteristics of carbon composite paper importantly contributing in PEMFC performance. Technological innovation on biomass conversion is further developed for the improvement of carbon structural properties, focusing on the development of graphitic carbon (Chapter II) and porous graphitic carbon materials (Chapter III) that exhibit good performance for anodes material in energy storage systems of lithium-ion batteries. The objective of this study to develop an effective and sustainable technology for converting biomass into functional carbon materials from coconut coir waste as a promising electrode material for potential application in the field of energy conversion and storage.

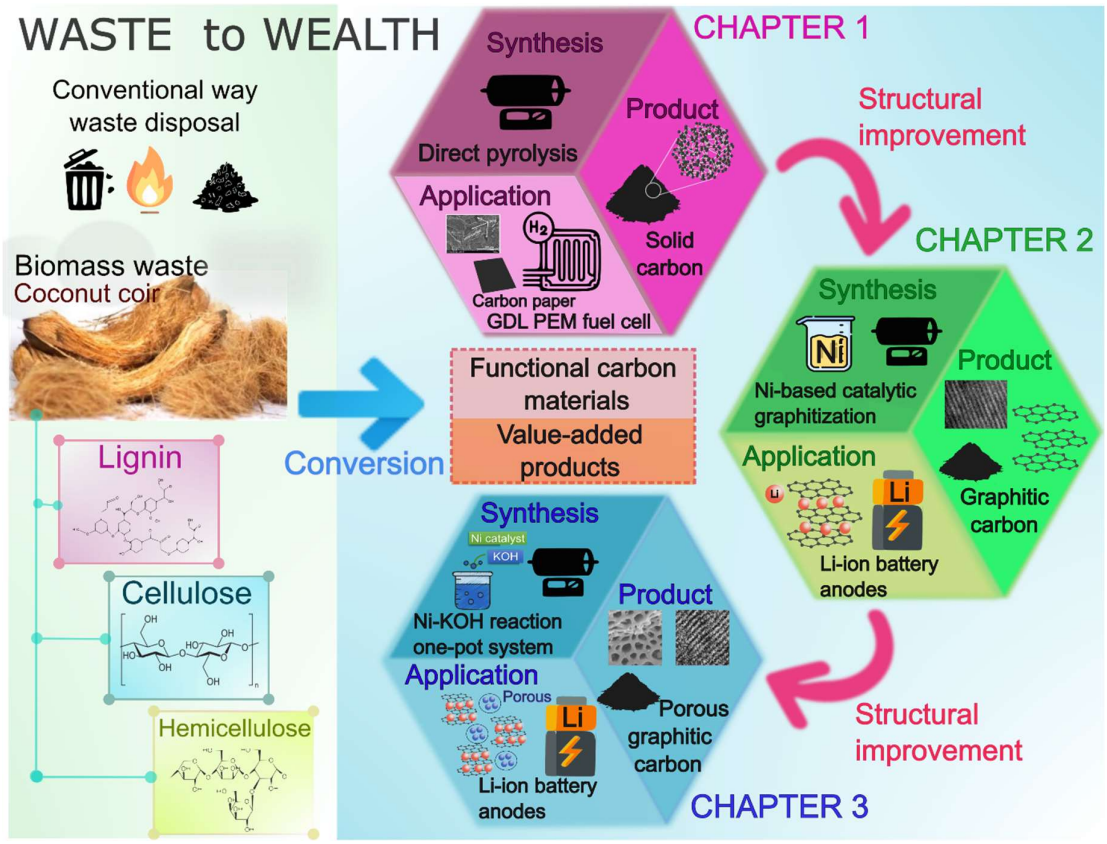

Figure 4. Graphical abstract of this doctoral dissertation

Chapter 1

In this chapter, amorphous carbon materials obtained by direct pyrolysis of coconut coir for producing conductive carbon composite paper (CCP) as PEMFC gas diffusion layer (GDL) are described. The CCPs were prepared by combining two different forms of carbon material from coconut coir: powder (particle size: ±74 m) and fiber (length: ±2 mm, diameter: 100–500 m), with the objective of achieving high electrical conductivity. A series of CCPs with different values of electrical conductivity were obtained by adjusting the weight ratio between these two forms of amorphous carbon materials obtained from coconut coir. The effect of carbon form on CCP properties, such as electrical conductivity, porosity, hydrophobicity, microstructure, and performance as a GDL in a stack of PEMFC systems, was comprehensively investigated and compared to commercial carbon paper. These findings highlight the promising potential of

CCPs developed from coconut coir as a sustainable and renewable GDL material for PEM fuel cells, exhibiting cell performance that is close to that of commercially available GDLs.

Chapter 2

In this chapter, the structural improvement of amorphous carbon from coconut coir obtained by the method in Chapter 1 was carried out through catalytic graphitization. This allows for the formation of graphitic carbon nanostructures at temperatures that are relatively lower in comparison to the temperatures required by conventional graphitization methods. By implementing a two-step process, consisting of carbonization at 500 °C to produce charcoal followed by nickel-based catalytic graphitization, highly crystalline graphitic nanostructures were successfully generated. The temperature during the graphitization process plays a crucial role in the structural transformation from amorphous to graphitic nanostructures. The results reveal that the carbon structure of coconut coir begins to transition from amorphous to ordered graphitic nanostructures at 1200 °C, a temperature lower than that required for conventional graphite production. The formation of graphitic nanostructures exhibiting a well-ordered arrangement around Ni particles is observed, with inter-planar spacing closely approximating the theoretical value of pure graphite (0.3354 nm). With the graphitization degree of the carbon structure (1200-ANi-GCM) about 82.16%, the graphitic structure present good electrochemical performance with a specific capacity of 192.6 mAh/g, a good cycling stability (the specific capacity remained 99.32 mAh/g after 30 cycles at 0.5C rate), and excellent rate performance (the specific capacity recovered when the rate was from 0.05C to 1C and then returned to 0.05C). The good electrochemical characteristics of this carbon graphite make it a promising alternative material for lithium-ion battery (LIB) anodes, providing a sustainable solution with a low-energy process and renewable raw materials. Moreover, this eco-friendly approach not only

contributes to mitigating the environmental impact associated with coconut waste but also offers potential solutions for sustainable energy storage systems.

Chapter 3

In Chapter 3, an advanced synthesis process is introduced to further enhance the structure and properties of the previously synthesized graphitic carbon material from Chapter 2. This refined approach aims to obtain functional carbon materials from coconut coir with a highly ordered graphitic structure as well as a high surface area through a simple and cost-effective synthesis method, thereby improving the performance as a lithium-ion battery anode and unlocking even greater potential for energy storage applications. The graphitization process by combining a Ni-based catalyst and potassium hydroxide (KOH) is carried out in a one-pot process to simultaneously generate graphitic and pore structures, resulting in porous graphitic carbon materials. The findings show that the pyrolysis temperature in the Ni catalyst and KOH treatment process had a positive effect on the structural transformation from an amorphous to highly ordered graphitic structure. The synergistic interaction between K and Ni metals initiates the formation of an early-stage graphitic structure at a lower temperature, around 800 °C, leading to the creation of larger graphitic clusters. However, as the pyrolysis temperature increases from 800 to 1200 °C, the specific surface area decreases due to disruptions in the microporous structure. As the LIB anode, 1000-ANi-KOH delivers the highest reversible capacity of 451.83 mAh/g at 0.05C, related to the optimal contribution between the graphitic structure and surface area. The unique porous graphitic carbon characteristics serve as a favorable and efficient channel for Li-ion/electron transport, thus increasing an active site for Li-ion storage. The Ni-KOH reaction in a one-pot graphitization process proves to be a promising method for converting waste coconut coir into a porous graphitic material suitable for LIB anodes. This process operates at a relatively low temperature and results in carbon

materials with enhanced structural properties and excellent electrochemical performance. Such advancements contribute to the sustainable utilization of coconut waste and provide a pathway for the development of efficient energy storage systems.

References

[1] S. Bhatt, B. Gupta, V. K. Sethi, M. Pandey, *Int. J. Curr. Eng. Technol.* **2012**, *2*, 219–226.

[2] Z. Li, Y. Wang, Y. Mu, B. Wu, Y. Jiang, L. Zeng, T. Zhao, *Renew. Sustain. Energy Rev.* **2023**, *176*, 113182.

[3] Y. Yang, X. Zhou, B. Li, C. Zhang, *Int. J. Hydrogen Energy* **2021**, *46*, 4259–4282.

[4] A. Ozden, S. Shahgaldi, X. Li, F. Hamdullahpur, *Prog. Energy Combust. Sci.* **2019**, *74*, 50–102.

[5] S. Yu, L. Wang, Q. Li, Y. Zhang, H. Zhou, *Mater. Today Sustain.* **2022**, *19*, 100209.

[6] G. Athanasaki, A. Jayakumar, A. M. Kannan, *Int. J. Hydrogen Energy* **2023**, *48*, 2294–2313.

[7] D. P. Leonard, S. Komini Babu, J. S. Baxter, H. M. Meyer, D. A. Cullen, R. L. Borup, *J. Power Sources* **2023**, *564*, 232619.

[8] R. Schweiss, C. Meiser, T. Damjanovic, I. Galbiati, N. Haak, *SGL Gr.* **2016**, 1–10.

[9] M. F. Mathias, J. Roth, J. Fleming, W. Lehnert, in *Handb. Fuel Cells*, **2010**.

[10] V. K. Mathur, J. Crawford, *Recent Trends Fuel Cell Sci. Technol.* **2007**, *400*, 116–128.

[11] Z. P. Cano, D. Banham, S. Ye, A. Hintennach, J. Lu, M. Fowler, Z. Chen, *Nat. Energy* **2018**, *3*, 279–289.

[12] P. U. Nzereogu, A. D. Omah, F. I. Ezema, E. I. Iwuoha, A. C. Nwanya, *Appl. Surf. Sci. Adv.* **2022**, *9*, 100233.

[13] H. Ali, H. A. Khan, M. G. Pecht, *J. Energy Storage* **2021**, *40*, 102690.

[14] C. M. Costa, J. C. Barbosa, R. Gonçalves, H. Castro, F. J. D. Campo, S. Lanceros-Méndez, *Energy Storage Mater.* **2021**, *37*, 433–465.

[15] M. Shi, C. Song, Z. Tai, K. Zou, Y. Duan, X. Dai, J. Sun, *Fuel* **2021**, *292*, 120250.

[16] L. Han, X. Zhu, F. Yang, Q. Liu, X. Jia, *Powder Technol.* **2021**, *382*, 40–47.

[17] R. Pell, P. Whattoff, J. Lindsay, *Minviro* **2021**.

[18] M. Inagaki, *Advanced Carbon Materials*, Elsevier Inc., **2013**.

[19] J. Deng, M. Li, Y. Wang, *Green Chem.* **2016**, *18*, 4824–4854.

[20] Badan Pusat Statistik-Statistics Indonesia, *Statistical Yearbook of Indonesia 2023*, **2023**.

[21] Directorate General of Estates, *Secr. Dir. Gen. Estates* **2022**, 1–572.

[22] L. Zhang, L. Y. Tu, Y. Liang, Q. Chen, Z. S. Li, C. H. Li, Z. H. Wang, W. Li, *RSC Adv.* **2018**, *8*, 42280–42291.

[23] N. I. F. Destyorini, A. Subhan, A. Suhandi, *Phys. J. Indones. Phys. Soc.* **2010**, *10*, 122–132.

[24] B. A. Mohamed, C. S. Kim, N. Ellis, X. Bi, *Bioresour. Technol.* **2016**, *201*, 121–132.

[25] N. A. S. Din, S. J. Lim, M. Y. Maskat, N. A. M. Zaini, *Biomass Convers. Biorefinery* **2021**, *11*, 815–826.

[26] T. Sesuk, P. Tammawat, P. Jivaganont, K. Somton, P. Limthongkul, W. Kobsiriphat, *J. Energy Storage* **2019**, *25*, 100910.

[27] E. I. Akpan, *Sustainable Lignin for Carbon Fibers: Principles, Techniques, and Applications*, **2019**.

[28] S. Li, W. L. Song, X. Han, Q. Cui, Y. li Zhu, S. Jiao, *Green Energy Environ.* **2023**, DOI 10.1016/j.gee.2023.04.006.

[29] J. Deng, T. Xiong, H. Wang, A. Zheng, Y. Wang, *ACS Sustain. Chem. Eng.* **2016**, *4*, 3750–3756.

[30] H. Zeng, B. Xing, Y. Cao, B. Xu, L. Hou, H. Guo, S. Cheng, G. Huang, C. Zhang, Q. Sun, *Int. J. Min. Sci. Technol.* **2022**, *32*, 1397–1406.

[31] Y. Guo, C. Su, H. Chen, B. Liu, L. Yu, J. Wang, J. Qiu, Z. Zeng, L. Li, Z. Zeng, L. Li, *J. Environ. Chem. Eng.* **2022**, *10*, 108985.

[32] C. Li, S. Yu, H. Dong, C. Liu, H. Wu, H. Che, G. Chen, *Appl. Catal. B Environ.* **2018**, *238*, 284–293.

[33] J. Wang, S. Wang, *J. Clean. Prod.* **2019**, *227*, 1002–1022.

[34] S. Yu, X. Yang, P. Zhao, Q. Li, H. Zhou, Y. Zhang, *J. Energy Inst.* **2022**, *101*, 194–200.

Chapter 1

Fabrication of conductive carbon composite paper from coconut coir through direct pyrolysis process for PEMFC gas diffusion layer

1.1 Introduction

As previously stated in the general introduction, the GDL, a porous component in PEMFC system, is mainly responsible for the distribution of reactive gases, water transport, and electrical pathways. GDLs require excellent electrical conductivity, appropriate porosity, and appropriate hydrophobicity to perform these functions [1–5]. They are typically porous component of mainly from carbon-based materials, which are commonly available in the form of carbon paper and carbon cloth [6–9]. Currently, GDLs are generally manufactured in a high-cost processes and uses carbon-based material from non-renewable fossil fuel resources such as coal, petroleum, polyacrylonitrile-based carbon fiber [10,11] and synthetic graphite [7]. This may raise concerns regarding sustainability. Therefore, to address this sustainability issue, the development of GDL utilizing carbon materials from abundant and renewable sources is required.

Plant biomass is a kind of low-cost, abundant, and renewable source of carbon material. Carbon material can be obtained through a carbonization process by degrading lignocellulosic compounds of biomass, such as cellulose, lignin, and hemicellulose under a N_2 atmosphere for a certain period [12,13]. The process produces porous charcoal residue with a high carbon content (50–80%) [14]. Coconut coir, a waste product of the coconut (*Cocos nucifera*) industry, is a type of plant biomass produced sustainably in significant amounts in Indonesia. Most of this waste is generally disposed of in conventional ways, such as landfills, incineration, or even open piles, all of which contribute to the pollution of the surrounding environment. For that reason, this chapter utilized coconut coir as a carbon source for preparing conductive carbon composite

paper (CCP) that was able to act as the GDL of PEMFC. This approach could help reduce dependencies on fossil fuels and alleviate environmental pollution.

In this chapter, carbon fiber and carbon powder obtained from a simple direct pyrolysis process of coconut coir at 1300 °C for three hours are utilized as raw materials for producing of CCPs. The composite formed by combining the two forms of carbon intends to obtain carbon composite paper with high electrical conductivity. The aim of this work is to create a renewable and sustainable carbon composite with good electrical conductivity and other comprehensive properties including porosity and hydrophobicity which are suitable for use as GDL in PEMFC. The CCP was then applied as a replacement for commercial carbon paper in a PEMFC stack, and its cell performance was evaluated (**Scheme 1-1**). The results demonstrate that the developed CCP from coconut coir shows promising potential as a GDL material for PEMFCs with comparable cell performance to commercial GDLs, while also providing a sustainable and renewable alternative.

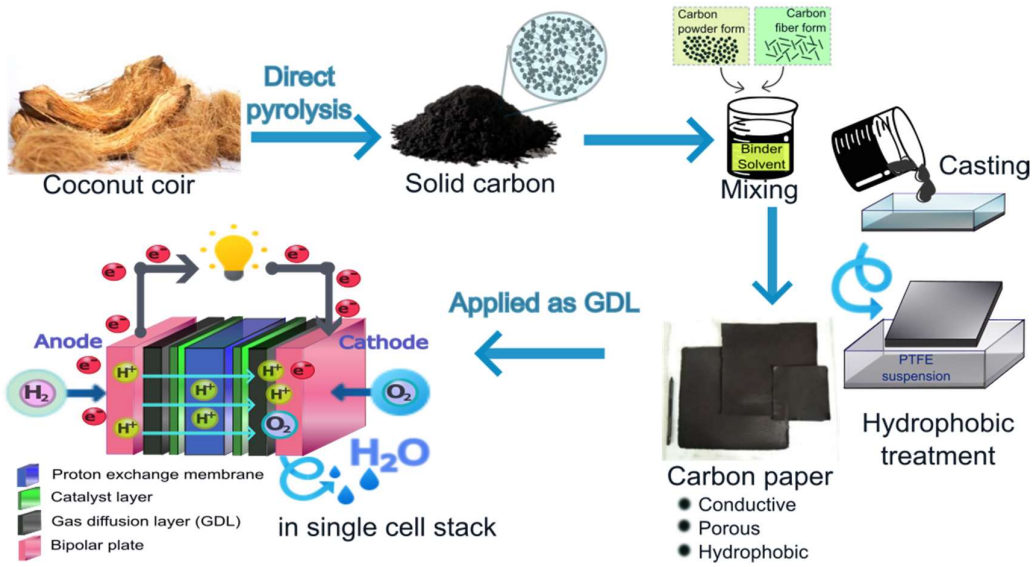

Scheme 1-1. Graphical abstract of Chapter 1

1.2 Experimental Section

1.2.1. Materials

Amorphous carbon materials were prepared from the pyrolysis products of coconut coir. Ethylene vinyl acetate (EVA) and polyethylene glycol (PEG) obtained from Aldrich Chemical Co., Inc. (St. Louis, MO, USA), were used as the binder and dispersant agent, respectively. Xylene (Brataco Chemika) was used as a solvent for making the CCP. Teflon emulsion polytetrafluoroethylene (PTFE) 30 obtained from Fuel Cell Earth LLC was used as a hydrophobic agent for CCP. Teflon emulsion PTFE 30 should be diluted to 10% concentration before being coated on the CCP surface. For comparison purposes, commercial carbon paper TGP-H-120 with 10% PTFE obtained from Toray Group was also investigated.

1.2.2. Production Process of Amorphous Carbon Materials

Carbon material with an amorphous structure was produced in two different forms: (i) carbon fiber and (ii) carbon powder. Both carbon materials were prepared from coconut coir by a two-stage process: carbonization and pyrolysis. In the carbonization process, coconut coir was heated at 500 °C for an hour under N_2 atmosphere and cooled down to room temperature to produce charcoal with a high carbon content. Subsequently, the obtained charcoal was pyrolyzed at 1300 °C for an hour under N_2 atmosphere to eliminate impurities and improve its electrical conductivity and other properties. For the final product, carbon powder was obtained by grinding and then mesh sieving to a size of about 74-µm. In the meantime, carbon fiber was produced by cutting the coconut coir to a length of approximately 2 mm prior to carbonization and pyrolysis.

1.2.3. CCPs Preparation

The CCPs were prepared by mixing the carbon materials (carbon fiber and carbon powder) obtained from the prior processes with EVA and PEG in xylene solvent at 100 ℃ for 2 hours to form a slurry. The mass ratio of carbon materials to EVA and PEG was 80:14:6 wt%. To make a paper, the slurry was cast onto glass mold, rolled, and then dried at room temperature for 24 hours to evaporate the solvent. Nine groups of samples were made with various carbon fiber and carbon powder compositions, as shown in **Table 1-1**. The CCPs with the highest and lowest electrical conductivities were treated with hydrophobic agents to improve their hydrophobic properties. The hydrophobic treatment was carried out by dipping the CCP in a 10% PTFE suspension for 30 minutes and drying at room temperature for 24 hours. They were then heated at 150 ℃ in an oven for 30 minutes to evaporate the surfactant and sintered at 350 ℃ for 30 minutes in air atmosphere.

Table 1-1. List of CCP sample codes in accordance with material composition variation.

Substrates	Composition (wt %)		EVA (wt %)	PEG (wt%)
	Carbon powder	Carbon fiber		
CCP-1	80	-	14	6
CCP-2	70	10	14	6
CCP-3	60	20	14	6
CCP-4	50	30	14	6
CCP-5	40	40	14	6
CCP-6	30	50	14	6
CCP-7	20	60	14	6
CCP-8	10	70	14	6
CCP-9	-	80	14	6

1.2.4. Physical Characterization

The CCPs and commercial carbon paper (TGP-H-120) were characterized using the same instruments and techniques for equitable comparison. The through-plane electrical conductivity was measured using a HIOKI 3522- 50 HITESTER LCR-meter. The porosity and density were determined by the kerosene density method using the Archimedes principle in accordance with BS 1902: Part 1A standard. The hydrophobic properties were determined from

the contact angle using a sessile drop test. For each measurement, a 50-μL water droplet was placed on the carbon paper surfaces by placing the tip of the syringe close to the sample surface, and images were captured every 20 min for an hour after the droplet was attached to the sample surface. Furthermore, the droplet shape was analyzed using Bashforth and Adams tables [15] to determine the contact angle of the samples. A HITACHI SU-3500 scanning electron microscope (SEM) was used to observe the surface and cross-section morphology of the samples. Energy-dispersive spectroscopy (EDS) mapping (X-maX, Horiba, Japan) was performed to analyze the PTFE distribution in the carbon paper.

1.2.5. Fuel Cell Assembly and Performance Test

The commercially available catalyst-coated membrane (CCM) was applied to the GDL samples in this work. The GDLs were assembled on both sides of the membrane. The performances of MEAs were evaluated using the polarization curve or J-V curve. A commercial PEMFC single cell test fixture (WonATech) with an active area of 25 cm^2 was used to test the cell performance using SMART2 test station (WonATech). Pure hydrogen and oxygen were fed into anode and cathode side, respectively, at a flow of 300 ml/min and operated at open-end conditions. The cell and reactant humidification temperature were set at 55 and 50 °C, respectively to maintain the proper hydration of membrane. All GDL samples were activated before measurement cell performance carried out by operating the cell at 0.6 volt for an hour. This activation process was performed under the same condition as the measurement cell performance process.

1.3 Results and Discussion

1.3.1. Effect of Variation in Carbon Fiber Content on CCP Electrical Conductivity

The through-plane electrical conductivities of CCPs with different carbon fiber contents (0-80 wt%) are shown in **Figure 1-1** prior to PTFE treatment. The electrical conductivity of CCP increases alongside number of carbon fiber content. The CCP-8 sample with 70 wt% carbon fiber has the highest electrical conductivity. The carbon fiber has higher aspect ratio (L/D) than the carbon powder. The aspect ratio plays an important role in enhancing the electrical conductivity of the composites. Carbon fiber with a high aspect ratio formed a more electrically conductive path than carbon powder. The conductivity of the composite increased with the number of electrically conductive paths formed on it. However, the CCP-9 sample with higher carbon fiber content (80 wt%) had lower electrical conductivity than the CCP-8 sample because the carbon powder (10 wt%) filled the gap between adjacent carbon fibers and formed a more electrically conductive path. Powders and fibers used in combination have greater influence on the electrical conductivity of composites compared to fibers alone [16].

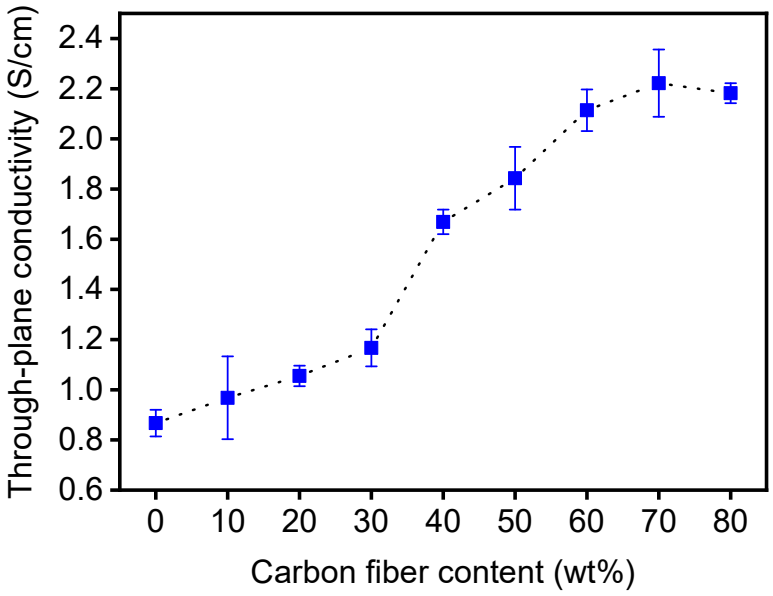

Figure 1-1. Electrical conductivity of CCP with various carbon fiber content.

1.3.2. Hydrophobic Treatment on CCP

The hydrophobic treatment in this study was performed by immersing the CCP, particularly the CCP-8 sample, which exhibited the highest electrical conductivity, in a 10% PTFE suspension for 30 minutes and drying it at room temperature. This treatment is aimed at improving the hydrophobic property of carbon paper used as a GDL by avoiding water-flooding in the GDL. **Table 1-2** shows the physical properties of CCP and commercial carbon paper. It is clearly seen that 10 wt% PTFE treatment of CCP improved the hydrophobic properties; the contact angle of CCP after PTFE treatment increased by 20.3° compared to that before the treatment. This value is comparable to that of commercial carbon paper.

Table 1-2. Physical properties of CCP and commercial carbon paper

Properties	Untreated CCP-8	PTFE-treated CCP-8	Commercial carbon paper
PTFE content (%)	0	10	10
Contact angle (°)	113.70±1.6	135.5±1.5	137.50±1.8
Bulk Density (gram/cm^3)	n.a	0.45±0.03	0.48±0.04
Porosity (%)	n.a	71.54±2.09	75.74±1.87
Through-plane conductivity (S/cm)	2.22±0.25	1.81±0.28	5.12±0.47

The contact angle value shown in **Table 1-2** was measured at the first observation after the droplet attached to the sample surface. **Figure 1-2** shows the results of the contact angle measurements performed every 20 min for a further an hour, and **Figure 1-3** shows photographs of the water drops on the sample surface after 20 min. The contact angle of untreated CCP after 20 min was below 90°, and it decreased to 0° after 40–60 min. Untreated CCP shows hydrophilic characteristics owing to the absence of a hydrophobic agent on its surface. The contact angle of PTFE-treated CCP-8 remained relatively constant from 0 to 60 min, as in the case of commercial carbon paper. This indicated that the hydrophobic properties of CCP obtained from coconut coir by PTFE treatment were comparable to those of commercial carbon paper. The porosity and bulk density of the PTFE-treated CCP-8 is also almost similar to those

of commercial carbon paper. Carbon paper used as a GDL allows the reactant gases to reach the reaction zones and the product water move out. To perform these functions effectively, carbon paper should have a high porosity of 50%–90% [17], the porosity of PTFE-treated CCP-8 satisfied this requirement. The effect of PTFE treatment on the electrical properties of carbon paper can be seen from the through-plane conductivity values listed in **Table 1-2**. PTFE treatment caused the electrical conductivity of CCP to decrease slightly from 2.22 to 2.09 S/cm. This was because the presence of non-conductive PTFE particles in the composite resulted in several conductive carbon materials failing to form electrically conductive paths. The electrical conductivity of PTFE-treated CCP was around 0.4 times that of commercial carbon paper.

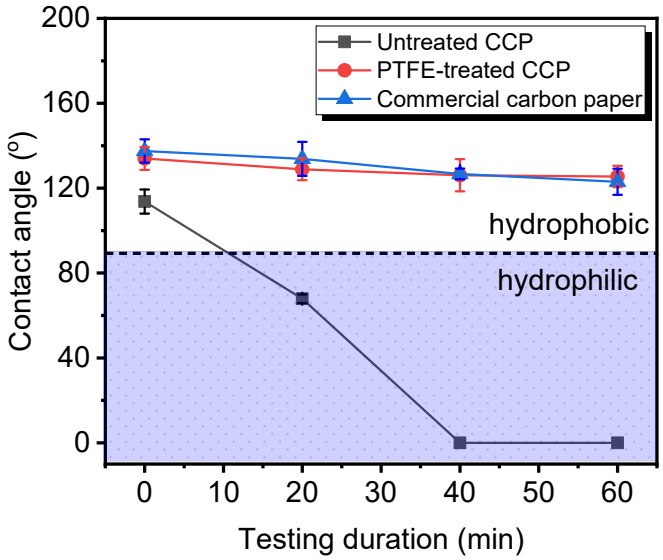

Figure 1-2. Contact angle of CCP-8 obtained from coconut coir and commercial carbon paper.

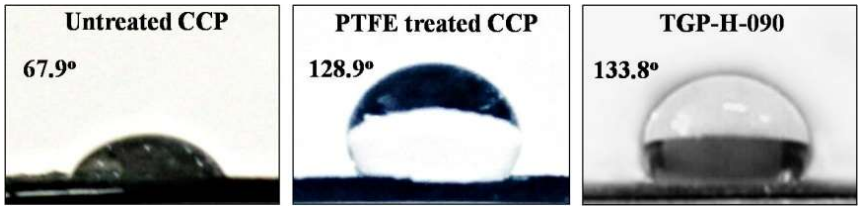

Figure 1-3. Photographs of water drops on untreated CCP-8, PTFE-treated CCP-8 obtained from coconut coir, and commercial carbon paper at 20 minutes.

1.3.3. PTFE Distribution of CCP

Figure 1-4 shows SEM images of the surfaces of untreated CCP-8, PTFE-treated CCP-8, and commercial carbon paper. As shown in **Figure 1-4(a-d)**, untreated CCP-8 and PTFE-treated CCP-8 show almost similar surface morphologies, namely, carbon fibers with length of 1–2 mm obtained from coconut coir. Observations with greater magnification, as shown in **Figure 1-4(b)** and **Figure 1-4(d)**, revealed that each carbon fiber comprises several hollow tubes. Furthermore, pores with ~1-μm diameter were spread across almost the entire wall of the hollow tube. The main pores of the CCP were in the range of 25–250 μm; they were formed by the internal spaces between carbon fibers. In contrast, commercial carbon paper comprises longer and smaller-diameter carbon fibers. This carbon paper has main pores only in the range of 10–100 μm; they were formed by the internal spaces between carbon fibers and were spread homogeneously across the surface of the carbon paper. **Figure 1-4(f)** shows that the carbon fibers were solid and nonporous.

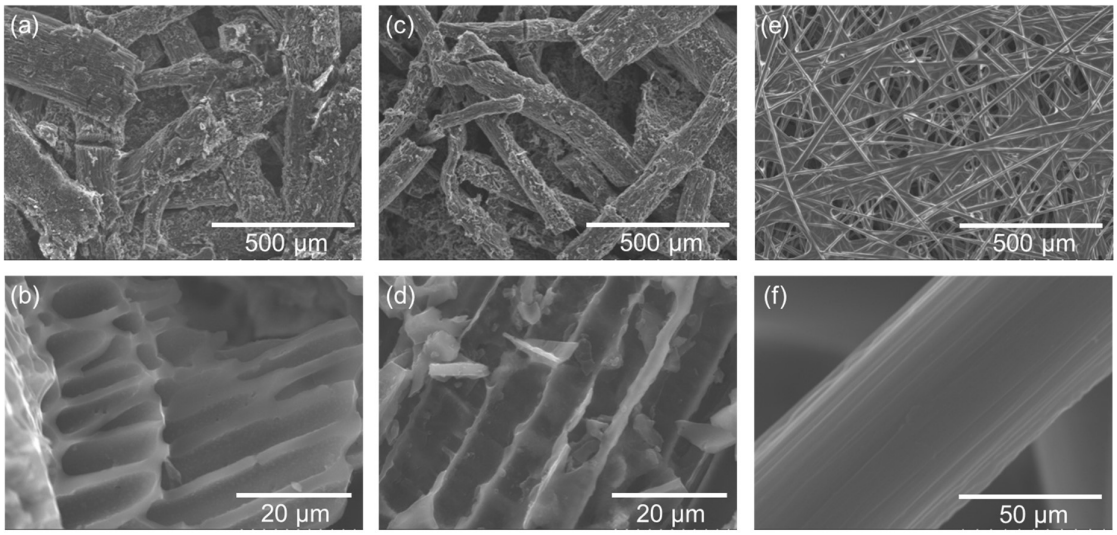

Figure 1-4. Surface morphologies of all samples under different magnifications: (a-b) untreated CCP-8, (c-d) PTFE-treated CCP-8, (e-f) commercial carbon paper.

The distribution of the hydrophobic agent could be seen using SEM with elemental mapping on the cross-section of the PTFE-treated CCP-8 and commercial carbon paper, as shown in **Figures 1-5** and **Figures 1-6**, respectively. Based on the results of carbon mapping shown in Figure **Figures 1-5(b)**, the CCP comprised carbon material (cyan-colored region) and pores (black-colored region). These pores were also seen on the surface, indicating that CCP has pores that are spread not only on the surface but also in the deeper part of the surface. The same was observed in commercial carbon paper (**Figures 1-6(b)**). **Figures 1-5(c)** and **Figures 1-6(c)** showed fluorine mapping of the CCP-8 and commercial carbon paper, respectively. These images indicate how far the PTFE (represented by elements of fluorine) dispersed in the carbon paper. As shown in **Figures 1-5(c)**, the PTFE particles (red-colored region) are spread on the surface and penetrate the CCP, as in the case of commercial carbon paper (**Figures 1-6(c)**). This indicates that hydrophobic material was deposited successfully in the CCP using the dipping technique, resulting in the improved hydrophobic properties of CCP, as shown in **Figures 1-2** and **Figures 1-3**.

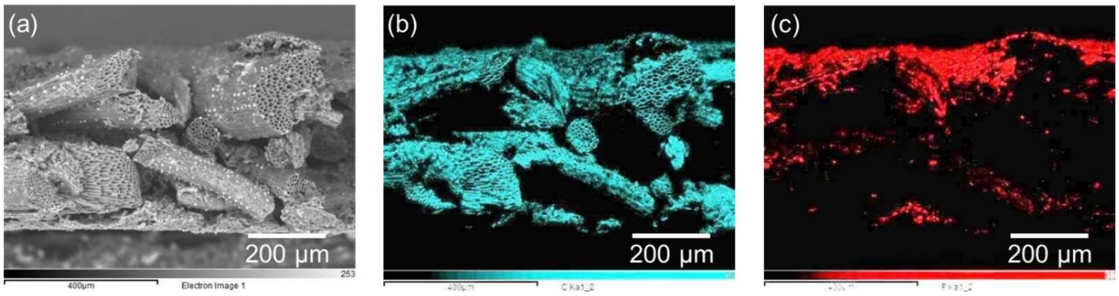

Figure 1-5. Cross-section morphologies and elemental mapping of PTFE-treated CCP: (a) SEM image, (b) carbon mapping, and (c) fluorine mapping.

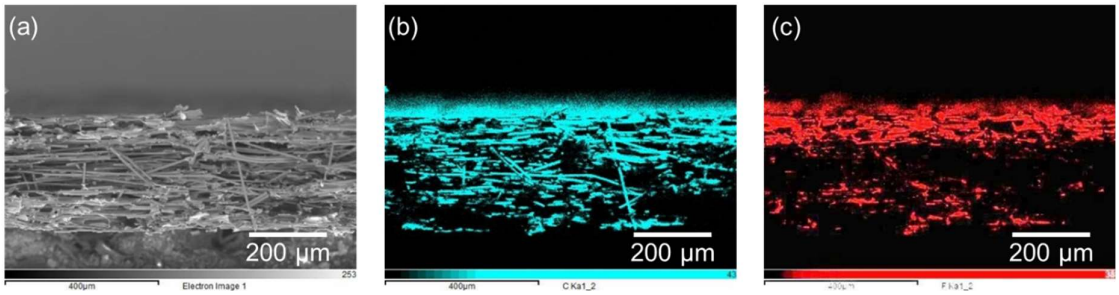

Figure 1-6. Cross-section morphologies and elemental mapping of commercial carbon paper: (a) SEM image, (b) carbon mapping, and (c) fluorine mapping.

1.3.4. Morphology of Carbon Papers

Figures 1-7 and **Figures 1-8** show the microscopic surface and cross-section morphologies of CCP-1, CCP-8, and the commercial carbon paper, respectively. The surface of CCP-1 with carbon material in powder shape appears smooth with a homogenous distribution of pores with sizes of about 1-50 µm, **Figures 1-7(a)**. The carbon powder seemed uniformly distributed in the matrix binder. This surface morphology is very similar to the micro-porous layer (MPL) on the carbon paper investigated by Shim, *et al.* [18]. The pore morphology can be seen more clearly in the cross-section view of CCP-1 (**Figures 1-8(a))**, which had a thickness of about 370 µm. The insert of **Figures 1-8(a)** clearly shows the original shape of the coconut fiber with some parallel hollow tube-like shapes close to each other with a diameter of 2-10 µm. **Figures 1-7(b)** reveals the surface morphology of CCP-8, a composite of carbon fiber and powder. From the top view of the surface, it can be seen that the morphology is completely different from that of CCP-1. It shows a discontinuous fiber-like shape with larger dimensions and a higher aspect ratio (L/D), spread randomly throughout the composite surface. Seen from the top, the pore size is about 25-250 µm, i.e., much lower than for CCP-1. The pores are formed by the internal spaces between the carbon fibers. These fibers can be seen more clearly at higher magnification in the cross-section view of CCP-8 in the insert of **Figures 1-8(b)**. It reveals that the fibers have a hollow tube-like morphology that is similar to that of CCP-1 (**Figures 1-8(a)**).

The fibers appear to be arranged irregularly and form pores with larger sizes than those of CCP-1. Meanwhile, **Figures 1-7(c)** and **Figures 1-8(c)** show the surface and cross-section morphology, respectively, of the commercial carbon paper (TGP-H-120). It can be seen that commercial carbon paper is composed of solid and non-porous carbon fiber with a finer diameter and higher aspect ratio compared with CCP-8. Seen from the top, the pore size is about 10-100 μm. The pores are formed by the internal spaces between the carbon fibers, as in CCP-8.

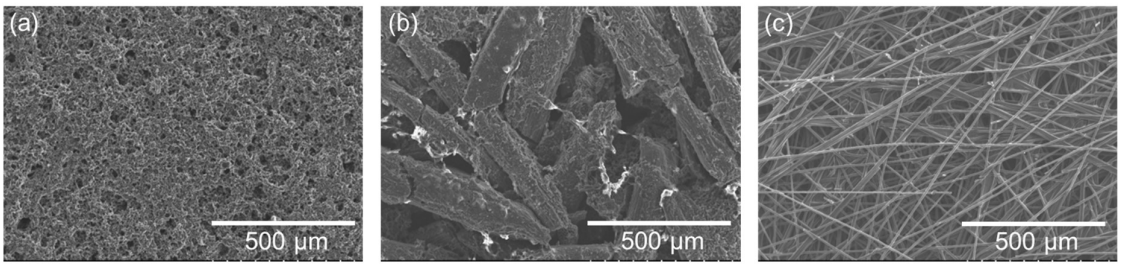

Figure 1-7. Surface morphologies of (a) CCP-1, (b) CCP-8, (c) commercial carbon paper.

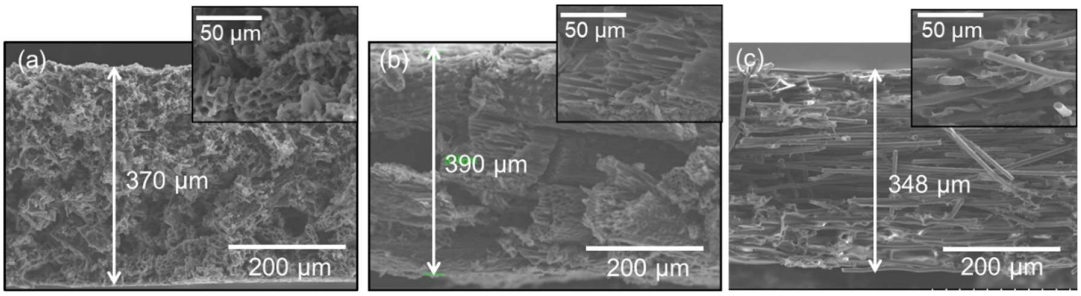

Figure 1-8. Cross-section morphologies of (a) CCP-1, (b) CCP-8, (c) commercial carbon paper.

1.3.5. Physical Properties of Carbon Papers

The physical properties of CCP-1, CCP-8 and the commercial carbon paper are summarized in **Table 1-3**. It shows that CCP-1 and CCP-8 have significantly different values of electrical conductivity and porosity. The combined use of carbon in fiber and powder shape in CCP-8 clearly enhanced the electrical conductivity compared with the CCP-1 (pure carbon

powder shape). This finding is consistent with the work of Wen, *et al.* [16] and Shen, *et al.* [19]. In CCP-8, carbon fibers with high aspect ratios were interconnected with each other (**Figure 1-7(b)**), thus establishing a continuous electrically conductive path. Hence, the electrons can be transported over a longer continuous path with fewer barrier than in CCP-1. This can also be explained by the carbon powder filling the gaps between adjacent carbon fibers, which creates more interconnected fibers. Thus, the increasing number of conductive paths leads to higher electrical conductivity of the composite CCP-8 than that of CCP-1. However, the conductivity of the commercial carbon paper was still much higher than that of our developed samples. As described above, CCP-1 had pores with smaller sizes and in greater numbers compared with CCP-8 (**Figure 1-7(a-b)** and **Figure 1-8(a-b)**), spread homogenously throughout the composite. This probably causes a higher porosity of CCP-1 than that of CCP-8, and a lower bulk density. Furthermore, all the tested materials exhibited relatively similar hydrophobic properties, while their contact angle value was not significantly different. The ideal hydrophobicity for GDL has a contact angle between 90° and 180° based on water as a wetting agent [20].

Table 1-3. Electrical and physical properties of CCPs and commercial product.

Parameter	CCP-1	CCP-8	Commercial carbon paper
Electrical conductivity (S/cm)	0.50±0.03	1.81±0.28	4.50±0.26
Porosity (%)	74.24±2.04	71.54±2.09	74.02±1.98
Bulk density (gram/cm^3)	0.43±0.02	0.45±0.03	0.50±0.04
Contact angle (˚)	139±1.5	135.5±1.5	131±1.7
BET Surface area (m^2/gram)	15.72	14.86	213.80
Average pore diameter (nm)	4.02	6.49	5.56

1.3.6. Cell Performance from PEMFC Test

Figure 3 shows the performance test of the GDLs based on CCP-1, CCP-8, and the commercial product. The curve indicating the MEA performance based on CCP-1 and CCP-8 is almost the same for both, especially for low current density (with voltage higher than 0.7 V). The slight difference between these two types of as-developed GDLs is noticeable only in the

medium and high current density region (about 100-500 mA/cm^2). As is already known, the polarization curve of the J-V curve is the most important characteristic and is a convenient tool for the design and optimization of PEMFC systems [21]. There are three main parameters that can be obtained directly from the J-V curve to evaluate cell performance, namely: (i) open circuit voltage (OCV), (ii) current density at operation voltage of 0.6 V (J0.6), and (iii) maximum power density (Pmax), as can be seen in **Table 1-4**. From the J-V curve, voltage losses or overpotential of the cell can be estimated.

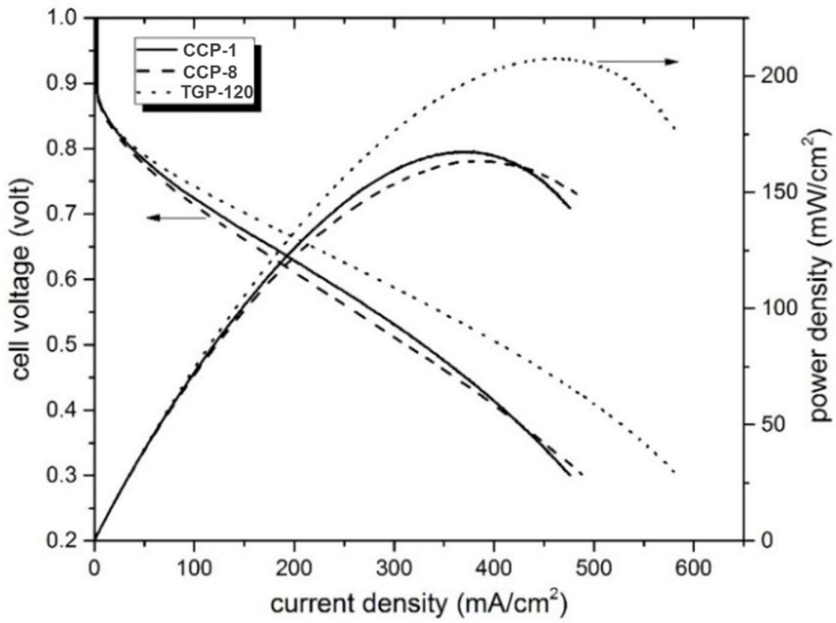

Figure 1-9. Cell MEA performance based on GDL CCP-1, CCP-8, and commercial carbon paper (TGP-120).

Table 1-4. Parameters of the cell performance for the three kinds of MEAs.

Substrates	OCV (V)	$J_{0.6}$ (mA/cm^2)	P_{max} (mW/cm^2)
CCP-1	0.997	232	168
CCP-8	0.979	212	164
Commercial carbon paper	1.000	284	208

During the operational test, the cell potential is decreased from its ideal performance due to three main overpotentials, namely: (i) activation, (ii) ohmic, and (iii) diffusion overpotential [22,23]. Activation overpotential dominates at low current density and is related to the slowness of the reaction that is taking place on the electrode surface. This overpotential highly depends on the activity of the catalyst sites. In **Figure 1-9** it can be seen that the J-V curves of the cell based on the three different GDLs (CCP-1, CCP-8, and commercial carbon paper) are almost identical at low current density. This shows that the catalytic activity of the catalyst layer of the GDLs was nearly the same, because the three GDLs used the same CCM catalyst.

Starting from a current density of 50 mA/cm^2 and clearly noticeable in the middle current density region (about 100-400 mA/cm^2), the three GDLs revealed different performances. At the middle current density known as the ohmic overpotential region, the performance losses are dominated by the electrical resistance of the electrode and the resistance of the ion (proton) flow in the electrolyte. Because the three GDLs used the same CCM catalyst and test apparatus, the ohmic overpotential can be attributed to the electrical conductivity of the GDLs, as shown in **Table 1-3**, where the conductivity of commercial carbon paper is much higher than that of CCP-1 and CCP-8. On the other hand, the J-V curves of CCP-1 are slightly higher than those of CCP-8 in this current density region, whereas the conductivity of CCP-8 is higher than that of CCP-1. This indicates that high electrical conductivity only cannot directly lead to high performance of the cell. This can also be contributed to the surface morphology and pore size of the GDL itself. CCP-1 has a smoother surface and smaller pore sizes than CCP-8 (**Figure 1-7(a)** and **Figure 1-7 (b)**). These two factors probably prevent the catalyst ink from penetrating into the pores of the carbon paper (during the preparation process) [24] and this will affect the reduction of the contact resistance of the catalyst layer/GDL [7], as illustrated in **Figure 1-10**.

The third contribution of the overpotential is diffusion or mass transport. This overpotential is clearly shown at high current density and it appears since there is a concentration gradient of reactant due to the limited supply of reactants. At cell voltage of 0.3 V, the cell based on commercial carbon paper had a current density of 580 mA/cm^2, whereas for CCP-1 and CCP-8 it was 476 and 488 mA/cm^2, respectively. From previous results, diffusion overpotential is closely related to porous electrodes, since the pore size distribution and hydrophobicity of the GDL influences the possibility of water flooding inside the cell [25]. However, in this study, apart from the three GDLs having a similar porosity and contact angle (**Table 1-3**), differences in mass transport overpotential were still strongly detected. This phenomenon could be related to the different structure of the GDLs, especially for CCP-1 and CCP-8.

At high current density, GDL has two main functions. Firstly, it can effectively transport sufficient reactants to the electrodes, and secondly, it provides a good water management system that facilitates water vapor to flow out from active sites to flow field plates in order to avoid flooding inside the cell. It has been reported that roughness features presented on the surface of the GDL contribute highly to water pinning and evaporation. A lower surface roughness or smoother surface of the GDL indicates higher pinning and lower water evaporation [26]. This means that CCP-1, which has a smoother surface, as shown by the SEM image in **Figure 1-7**, would need more time to remove water droplets into flow channels compared to CCP-8. This could increase the possibility of water clogging and hinder the reactant distribution, as indicated by the lower J-V curve in the high-current region.

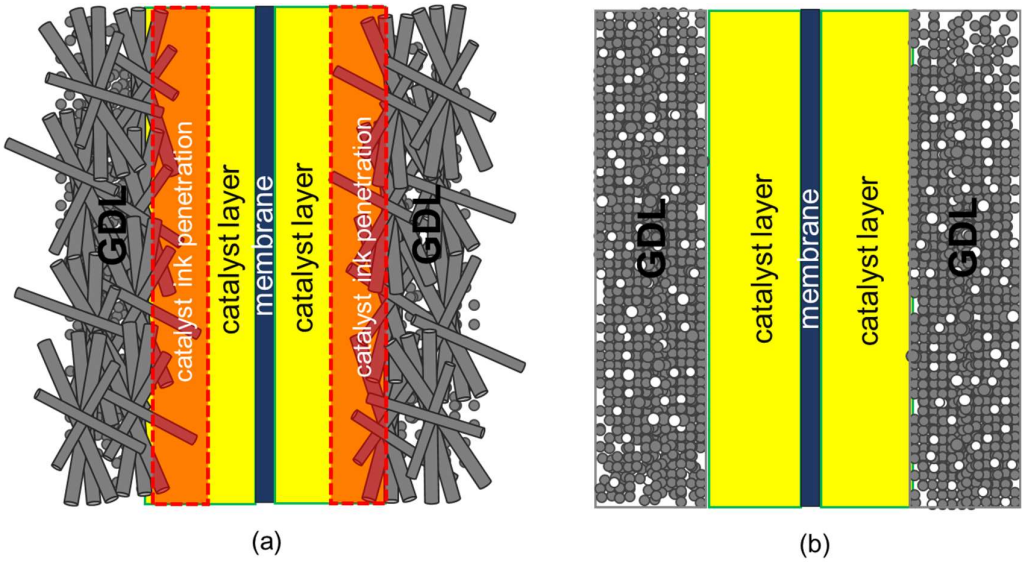

Figure 1-10. Schematic representation of MEA with (a) CCP-1 and (b) CCP-8 as GDL.

1.4 Conclusions

In this study, carbon composite paper, which can serve as GDL in PEMFC, was successfully prepared using carbon materials derived from biomass waste, specifically coconut coir, by varying the powder and fiber forms of carbon materials. Sample CCP-8 with a composition of 70 wt% carbon fiber, 10 wt% carbon powder, and 20 wt% polymer showed the highest electrical conductivity (2.22 S/cm). The combined use of carbon fiber and carbon powder may enhance the electrical connectivity of the composite, resulting in improved electrical conductivity. However, when applied as GDL in PEMFC stack, CCP-8 exhibits slightly lower cell performance than CCP-1 at the middle current density, due to its unfavorable surface morphology and pore size. Apart from being beneficial for its electrical conductivity, the smooth GDL surface and suitable pore size also play a role in resulting high cell performance. The smoother surface and smaller pores of CCP-1 prevent catalyst ink from spreading into the pores of the carbon paper and reduce the contact resistance between the catalyst layer/GDL, resulting in higher current density and power.

1.5 References

[1] N. Parikh, J. S. Allen, R. S. Yassar, *Fuel Cells* **2012**, *00*, 1–9.

[2] S. Park, J. W. Lee, B. N. Popov, *J. Power Sources* **2006**, *163*, 357–363.

[3] J. Lobato, P. Cañizares, M. A. Rodrigo, C. Ruiz-López, J. J. Linares, *J. Appl. Electrochem.* **2008**, *38*, 793–802.

[4] J. Ge, A. Higier, H. Liu, *J. Power Sources* **2006**, *159*, 922–927.

[5] E. Sengul, S. Erkan, I. Eroglu, N. Bac, *Chem. Eng. Commun.* **2008**, *196*, 161–170.

[6] S. Bhatt, B. Gupta, V. K. Sethi, M. Pandey, *Int. J. Curr. Eng. Technol.* **2012**, *2*, 219–226.

[7] C. Han, I.-T. Kim, H.-J. Sun, G. Park, J.-J. Lee, H.-K. Lee, J. Shim, *Int. J. Electrochem. Sci.* **2012**, *7*, 8627–8636.

[8] S. Park, B. N. Popov, *Fuel* **2011**, *90*, 436–440.

[9] L. Cindrella, A. M. Kannan, J. F. Lin, K. Saminathan, Y. Ho, C. W. Lin, J. Wertz, *J. Power Sources* **2009**, *194*, 146–160.

[10] A. G. Chiroptical, C. One, **2013**, 1–5.

[11] Z. Y. Xie, G. Y. Jin, M. Zhang, Z. A. Su, M. Y. Zhang, J. X. Chen, Q. Z. Huang, *Trans. Nonferrous Met. Soc. China* **2010**, *20*, 1412–1417.

[12] T. Kinumoto, T. Matsumura, K. Yamaguchi, M. Matsuoka, T. Tsumura, M. Toyoda, *ACS Sustain. Chem. Eng.* **2015**, *3*, 1374–1380.

[13] A. Dobashi, J. Maruyama, Y. Shen, M. Nandi, H. Uyama, *Carbohydr. Polym.* **2018**, *200*, 381–390.

[14] N. Indayaningsih, D. Priadi, A. Zulfia, Suprapedi, *Key Eng. Mater.* **2011**, *462–463*, 937–942.

[15] F. Bashforth, J. C. Adams, *An Attempt to Test the Theories of Capillary Action by Comparing the Theoretical and Measured Forms of Drops of Fluid. With an Explanation of the Method of Integration Employed in Constucting the Tables Which Give the Theoretical Forms of Such Drops*, Cambridge [Eng.] University Press, Cambridge, **1883**.

[16] S. Wen, D. D. L. Chung, *Carbon N. Y.* **2007**, *45*, 505–513.

[17] G. H. Yoon, Y. il Park, *Int. J. Precis. Eng. Manuf.* **2012**, *13*, 1153–1159.

[18] J. Shim, C. Han, H. Sun, G. Park, J. Lee, H. Lee, *Trans . Korean Hydrog. New Energy Soc.* **2012**, *23*, 34–42.

[19] L. Shen, F. Q. Wang, H. Yang, Q. R. Meng, *Polym. Test.* **2011**, *30*, 442–448.

[20] S. Park, B. N. Popov, *Fuel* **2009**, *88*, 2068–2073.

[21] S. Haji, *Renew. Energy* **2011**, *36*, 451–458.

[22] J. Larminie, A. Dicks, *2nd Ed. John Wiley Sons Ltd* **2003**, *93*, 14–16, 67–72.

[23] I. Khazaee, M. Ghazikhani, *Heat Mass Transf.* **2012**, *48*, 799–807.

[24] C.-J. Tseng, S.-K. Lo, *Energy Convers. Manag.* **2010**, *51*, 677–684.

[25] M. Han, J. H. Xu, S. H. Chan, S. P. Jiang, *Electrochim. Acta* **2008**, *53*, 5361–5367.

[26] J. Gostick, *Chem. Eng.* **2008**, *Ph.D.*

Chapter 2

Graphitic carbon nanostructured from nickel-based catalytic graphitization of coconut waste and its potential application for lithium-ion battery anodes

2.1 Introduction

As the field of energy conversion technology continues to grow, the demand for reliable and efficient energy storage systems is steadily increasing, particularly for use in electronic and transportation devices[1]. In recent years, rechargeable batteries, with their high-energy capacity and cycle endurance, have emerged as the next generation of mobile electrical energy storage devices. Lithium-ion batteries (LIBs) are among the most commercially used electrical energy storage technologies, and their demand has led to an increased need for electrode materials, including anode materials[2,3]. Graphite has long been a popular choice for LIB anodes, due to its excellent conductivity, reversibility for lithium-ion intercalation/deintercalation, low operation potential, and high specific capacity[4,5]. However, graphite is typically produced from fossil fuel-derived sources, such as petroleum coke, coal-tar, or pitch[6–10], which raises concerns about sustainability, availability, and CO_2 emissions. In addition, high energy and production cost are required to obtain graphite from its precursor owing to high temperature of structural converting process (>2000 °C)[8–10]. In response to this challenge, the utilization of sustainable and low-cost carbon sources with a simple fabrication method has become a focus of the energy research field.

In this context, coconut coir as a biomass waste has been identified as a promising sustainable precursor to produce graphitic carbon materials due to its abundance, renewability, and low cost. Low temperature catalytic graphitization is a preferred strategy for converting biomass to graphitic carbon structure compared to conventional graphitization process[11].

Transition metals such as iron (Fe)[12,13], cobalt (Co)[14], nickel (Ni)[15–17], chromium (Cr), or manganese (Mn)[18,19] have been proven as catalysts for reducing the graphitization temperature due to the catalytic activity of metal particles formed during the process.

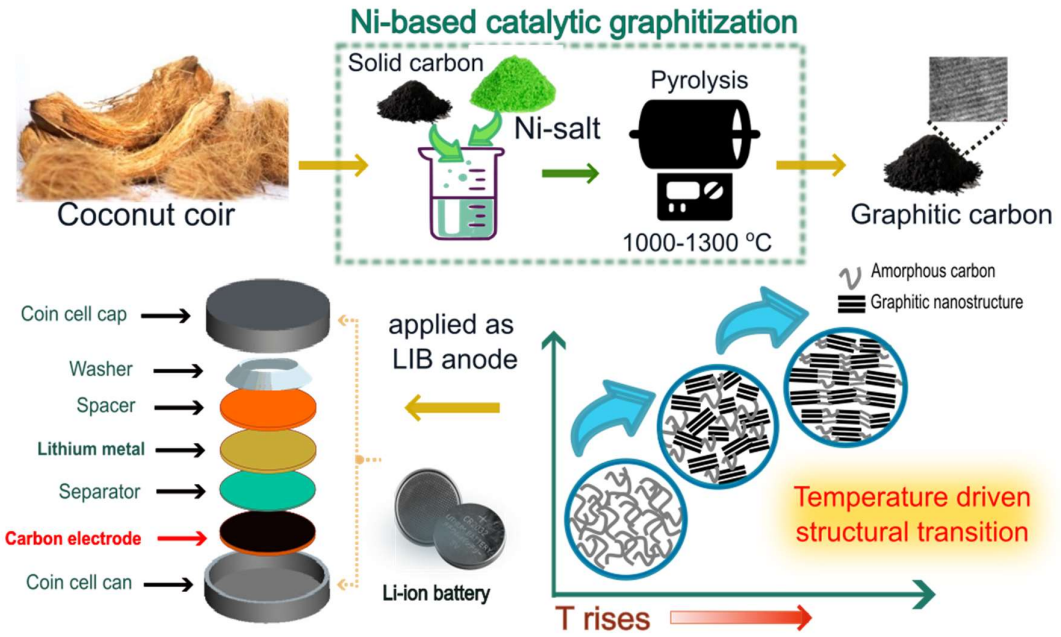

Scheme 2-1. CtNF fibers wrapping around PSL.

This chapter demonstrates the conversion of coconut coir into nanostructured graphitic carbon materials via Ni-based catalytic graphitization and investigates their prospective application as anodes in lithium-ion batteries (LIB), as shown in **Scheme 2-1**. Ni-based catalysts are preferred for graphitization owing to their effectiveness in producing graphitic structures with relatively high crystallinity[20] and their corrosion resistance in basic or acidic environments. Structural transformations in response to pyrolysis temperature are elucidated based on the findings of X-ray diffraction (XRD), Raman spectroscopy, X-ray photoelectron spectroscopy (XPS), and transmission electron microscopy (TEM) analysis. The proposed approach offers a sustainable and cost-effective alternative to the conventional production of graphite for LIB anodes. The resulting graphitic carbon materials exhibited high degree of graphitization, good electrochemical performance, and low environmental impact. The

potential of this approach could lead to a significant reduction in the carbon footprint of LIBs, contributing to the development of more sustainable energy storage systems.

2.2 Experimental Section

2.2.1. Materials

Coconut coir used in this work was obtained from local market in Indonesia as by-products. Nickel (II) chloride hexahydrate ($NiCl_2.6H_2O$) and hydrochloric acid (HCl, 37%) were purchased from Merck. The water used throughout the experiment was purified using Evoqua LaboStar PRO TWF UV ultra-pure water system.

2.2.2. Preparation of amorphous carbon from coconut coir waste

Twenty gram of raw coconut coir was carbonized at 500 °C for an hour under N_2 gas atmosphere. The process produced charcoal in amorphous phase with a yield of about 30.73 wt.%. The ultimate and proximate analysis of amorphous carbon was tested using EDTA method (LECO CHN628) and Gravimetric method, respectively, with the results provided in Table **2-1**. The amorphous carbon was then ground into a carbon powder with a particle diameter of approximately 74 μm.

Table 2-1. Ultimate analysis and proximate analysis result of raw coconut coir and its charcoal

	Coconut coir charcoal (carbonized at 500 °C)
Ultimate analysis:	
Carbon (%)	71.06
Hydrogen (%)	3.76
Nitrogen (%)	0.65
Proximate analysis:	
Volatile matter (%)	25.99
Ash (%)	6.72
Fix carbon (%)	67.28

2.2.3. Preparation of graphitic carbon from coconut coir waste

The amorphous carbon material (6.15 g) obtained in the previous steps was then immersed in a solution of $NiCl_2 \cdot 6H_2O$, with a mass ratio of carbon to $NiCl_2 \cdot 6H_2O$ is 1:1.2. The mixture was stirred at 60 °C until all the solvent evaporated. Ni-impregnated carbon was obtained after drying the solid overnight at 80 °C. The Ni-impregnated carbon was graphitized in a tube furnace (6-cm inner diameter) under nitrogen gas (N_2) with a flow rate of 200 mL/min at 1,300 °C for 3 h. The product was designated as 1300-Ni-GCM with a yield of 31.67 wt%. A portion of the 1300-Ni-GCM product (6.33 g) was stirred in a 2 M HCl solution overnight to remove the metal. The solid was then washed repeatedly with deionized water and dried at 80 °C. The acid-treated sample was designated 1300-ANi-GCM with a yield of 24.22 wt%. The control sample was prepared at the same temperature without Ni impregnation and designated 1300-CC. Commercially available graphite powder (ThermoFisher Scientific, USA) was also characterized for comparison.

To investigate the effect of temperature on the structural transition of coconut coir-derived carbon from amorphous into graphitic carbon nanostructure through nickel catalytic graphitization, the Ni-impregnated carbon samples were also heat treated at various temperatures of 1000, 1100, 1200, 1300 °C. The synthesis procedure was identical to 1300-ANi-GCM. The obtained samples were denoted as "t-ANi-GCM", where the letter "t" represents heat treatment temperature.

2.2.4. Structural and morphological characterization of the GCM samples

A Rigaku SmartLab X-ray Diffractometer with Cu-Kα radiation (λ = 1.54059 Å) over the scanning angle (2θ) range of 10–80° at 40 kV and 30 mA was used to record the XRD patterns of all samples. The carbon interlayer spacing (d_{002}) was calculated by the equation of $d_{002} = \lambda/2\sin\theta_{002}$, where λ is the wavelength of the Xray radiation and θ_{002} is the (002) reflection angle [21]. Raman spectra were recorded using Horiba Modular Raman iHR320 at a laser

wavelength of 532 nm and scanned between 1000 to 2850 cm^{-1} with data acquisition time of 10 s. Three different spots for each sample were scanned to ensure the accuracy of measurement. Analysis of Raman spectra were carried out by peak deconvolution using the curve-fitting procedure for carbon-based materials developed by Smith et al. [22]. XPS spectra were recorded using JEOL JPS-9010MC. The XPS parameters included the power of analysis (wide: 75 W, narrow: 150 W) and monochromatic Al Kα. The peaks were fitted by using CasaXPS version 2.315 computer program (Casa Software Ltd). Graphitic nanostructure morphology was also investigated by transmission electron microscopy using JEM 2100 operated at 200 kV accelerating voltage. All samples for TEM analysis were dispersed in ethanol and dropped on carbon-coated grids followed by drying process at room temperature.

2.2.5. Electrochemical Measurement

All the electrochemical tests were conducted in coin cells (CR2032). Electrode slurries were prepared by mixing 80 wt. % of the carbon samples as active material with 10 wt. % of polyvinylidene fluoride binder and 10 wt. % of conductive agent (Super P). Then, the powder mixture was dispersed in dimethylacetamide and cast on a copper foil using a standard doctor blade technique. The mass loading of the active material was 2−7 mg/cm2. Coin cells were assembled in half-cell configuration using a lithium metal electrode as the reference and counter electrode and a standard electrolyte lithium hexafluorophosphate (LiFP6) 1 Min ethylene carbonate and dimethyl carbonate with a molar ratio of 1:1 at room temperature. Cell assembly was conducted in an Ar-filled glovebox. Galvanostatic charge/discharge (CD) and cyclic voltammetry (CV) measurements of the samples were performed by using a WBCS3000 Automatic Battery Cycler. The CD tests were carried out with C-rate variation of 0.05, 0.1, 0.2, 0.5, and 1 C at potentials ranging from 1.0 to 3.0 V (vs Li+/Li). The CV test was conducted between 0 and 2.5 V at a scan rate of 0.1 mV/s.

2.3 Results and Discussion

2.3.1. Formation of nanostructured graphitic carbon from coconut waste via low-temperature catalytic graphitization

Morphological characterization

The morphology of carbon material derived from coconut coir was observed by SEM, as shown in **Figure 2-1**. At low magnification, all samples exhibited the original coconut coir structure (i.e., fibers with several parallel hollow tube close to each other), as in our previous work [23–25]. The catalytic graphitization process and HCl treatment of carbon can produce more pores in the wall of the hollow tube of carbon, as seen in **Figure 2-1**(f) and **Figure 2-1**(i) for 1300-Ni-GCM and 1300-ANi-GCM, respectively. The effect of both processes on porous structure was also confirmed by the BET method. The N_2 adsorption–desorption isotherms are shown in **Figure 2-2**, and porous parameters are summarized in **Table 2-2**. Without the catalytic graphitization process and HCl treatment, the 1300-CC sample exhibited a low surface area of 5.71 m^2/g and the total pore volume of 0.02 cm^3/g. Furthermore, the catalytic graphitization process, which was conducted on the 1300-Ni-GCM sample, increased surface area to 51.61 m^2/g and its total pore volume to 0.1 cm^3/g owing to the etching reaction between the Ni salt catalyst and carbon. Further treatment of 1300-ANi-GCM using HCl increased surface area to 59.02 m^2/g owing to the removal of Ni particles, which created a more porous carbon.

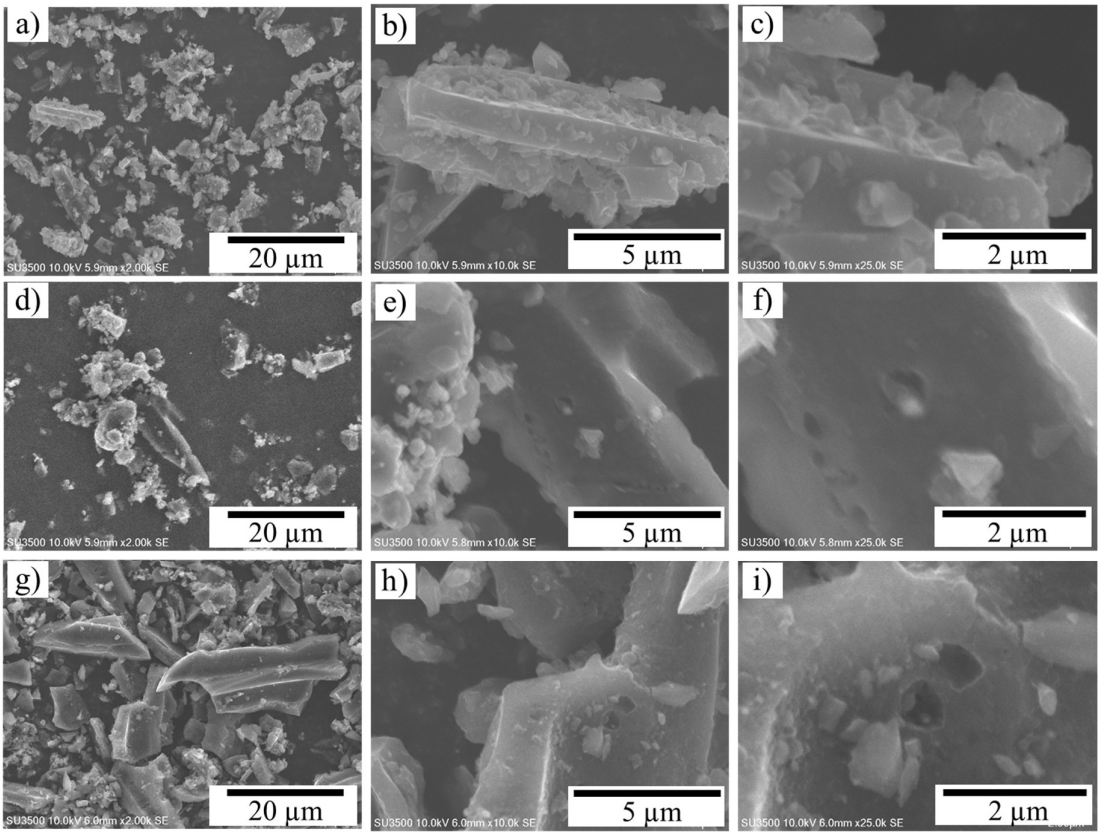

Figure 2-1. SEM images at various magnifications for (a–c) 1300-CC, (d–f) 1300-Ni-GCM, and (g–i) 1300-ANi-GCM.

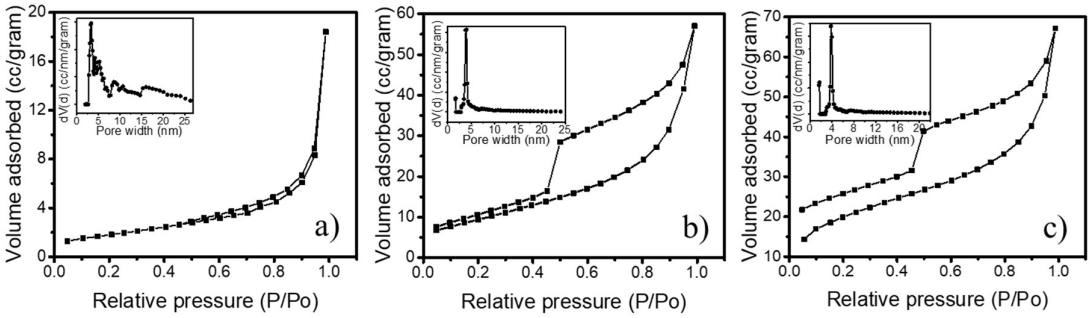

Figure 2-2. N_2 adsorption-desorption isotherms (inset: pore distribution) of (a) 1300-CC, (b) 1300-Ni-GCM, and (c) 1300-ANi-GCM.

Table 2-2. Porous structure parameters of all carbon sample derived from coconut coir.

Parameters	1300-CC	1300-Ni-GCM	1300-ANi-GCM
BET surface area (m^2/g)	5.71	51.61	59.02
Total pore volume (m^3/g)	0.02	0.10	0.10
Micropore volume (m^3/g)	0.01	0.08	0.08
Mesopore volume (m^3/g)	0.01	0.02	0.02
Average pore diameter (nm)	3.07	3.91	3.86

Structural characterization

XRD was performed to investigate structural changes in the carbon throughout the graphitization process. Diffraction patterns were collected from (2θ) 10° to 90° to characterize the graphitic structures. The patterns of the 1300-Ni-GCM and 1300-ANi-GCM samples treated with Ni each contained a strong peak centered an approximately 26.5° (**Figure 2-3**). This diffraction peak corresponded to the 002 plane of graphite, and it was also observed in the XRD pattern of commercial graphite. In contrast, the pattern of the carbon sample that underwent heat treatment at the same temperature without the nickel catalyst (1300-CC) contained a broad (002) peak that was shifted in the negative direction. This indicated that the sample contained large amounts of disordered carbon or an amorphous phase. These results showed that the nickel particles could catalyze the graphitization of coconut coir at a pyrolysis temperature as low as 1,300 ℃. XRD analysis was also helpful in determining that the HCl treatment was effective for removing the nickel particles from the 1300-ANi-GCM sample. Strong peaks in the pattern of the 1300-Ni-GCM sample at 44.5°, 51.8° and 76.4° were indexed to the 111, 002 and 022 planes of nickel, respectively (ICSD 98–005-3808). There are no clear NiO or Ni_3C peaks detected, which would typically be observed at approximately 2θ = 37° and 41°, respectively. Furthermore, Ni peaks were significantly less intense in the pattern of the 1300-ANi-GCM sample, which indicated the reduction of nickel particles in the samples. The removal of nickel particles by the HCl treatment was also observed using the EDS data (**Figure 2-4**). The amount of nickel decreased from 2.72 at. % to 0.76 at. % after the HCl treatment.

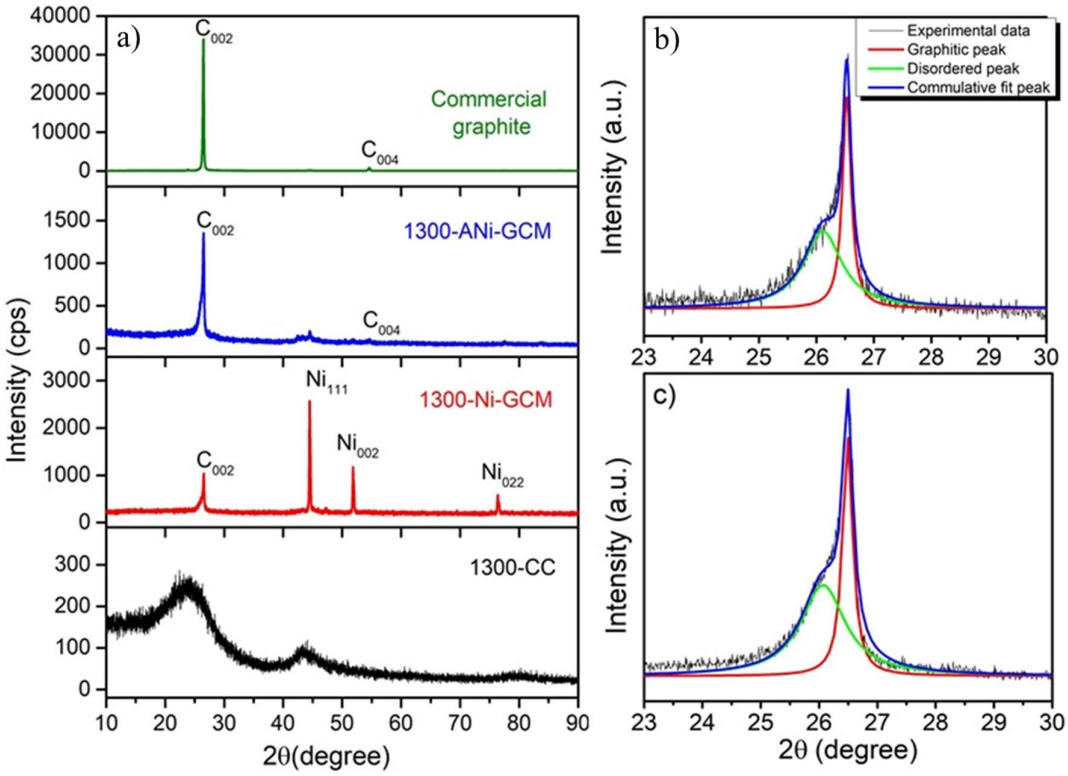

Figure 2-3. (a) XRD patterns of graphitic carbon materials obtained from coconut coir and commercial graphite. Fits of (b) 1300-Ni-GCM and (c) 1300-ANi-GCM (002) peaks.

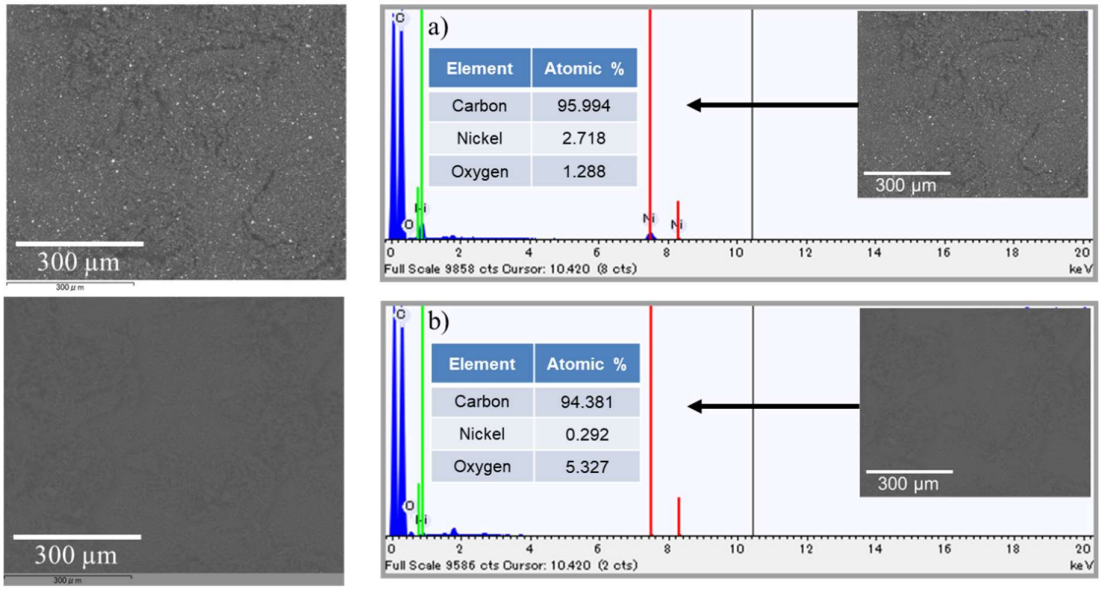

Figure 2-4. Energy Dispersive Spectrometer (EDS) data of (a) 1300-Ni-GCM and (b) 1300-ANi-GCM

In this study, the graphitization process of coconut coir charcoal using Ni catalyst started with the dehydration and decomposition of $NiCl_2 \cdot 6H_2O$ at certain temperature, which produced nickel oxide (NiO) [26]. Then, NiO was reduced to Ni nanoparticles by coconut coir charcoal. Kang et al. [27] have shown that nickel ions can be reduced to Ni metal nanoparticles by amorphous carbon as a reductant in an N_2 atmosphere at 500 °C. Another study has shown that nickel oxide particles can be reduced by natural graphite at high pyrolysis temperature [28,29]. Then, Ni nanoparticles dispersed and moved on the amorphous carbon matrix owing to the random diffusion effect and/or C–Ni interaction [30]. The process was followed by the reaction of Ni metal nanoparticles with amorphous carbon to form nickel carbide (Ni_3C). With an increase in the temperature, Ni_3C decomposed to Ni metal and formed a graphitic carbon structure through the dissolution–precipitation mechanism.

The (002) peaks were analyzed to obtain quantitative information about the crystal structures of the samples. The (002) peaks in the patterns of the 1300-Ni-GCM and 1300-ANi-GCM samples shown in **Figure 2-3**(b) and **Figure 2-3**(c), respectively, were obtained by profile fitting. The (002) peaks of both samples were clearly asymmetric. Careful fitting using the Origin software package showed that each peak consisted of two Lorentzian peaks, a broad disordered carbon band and a sharp graphitic band. These results were consistent with those obtained by Sevilla et al. [16], which indicated that the formation of graphitic carbon during catalytic graphitization occurred through dissolution and precipitation. Graphitic carbon precipitated around the catalyst particles after dissolution of the amorphous carbon in Ni. Amorphous carbon located far from any catalyst particles remained amorphous.

The (002) peaks in the XRD patterns were used to calculate the degree of graphitization (g), crystallite size (Lc), and the number of stacked C planes (n) in the samples after the fitting process. The degree of graphitization, g (%), was calculated using Eq. (2-1) [21,31].

$$g = (3.440 - d_{002}) / (3.440 - 3.354) \qquad (2\text{-}1)$$

where 3.440 is the interlayer spacing in non-graphitized carbon (Å); 3.354 is the interlayer spacing in an ideal graphite crystallite (Å); and d_{002} is the interlayer spacing in the sample determined from its XRD pattern (Å). The crystallite size (*Lc*) was calculated using Eq. (2-2) [21,32].

$$Lc = (K\lambda) / (\beta cos\theta) \quad (2\text{-}2)$$

where β is the full width at half maximum (FWHM) peak intensity at 2θ (rad), and *K* is a dimensionless constant that depends on the plane of reflection. In this case, *K* for the (002) peak is 0.89. The number of stacked carbon layer planes (*n*) was calculated using Eq. (2-3) [21].

$$n = Lc / d_{002} \quad (2\text{-}3)$$

The quantitative analysis results are shown in **Table 2-3**. The degree of graphitization is used to quantify the similarity between a carbon material and a perfect single graphite crystal [33]. We calculated g from the interlayer spacing (d) determined using the (002) peak. Sample 1300-Ni-GCM had a high degree of graphitization (84.88%) that was slightly lower than that of commercial graphite (90.23%). The acid treatment using 2-M HCl performed overnight to remove Ni from the graphitic carbon powder in the 1300-ANi-GCM sample caused a slight reduction in g. This meant that 1300-Ni-GCM had higher graphite content than that of the 1300-ANi-GCM sample. In addition, the acid treatment reduced the stacking height (*Lc*) and the number of stacked C planes (**Table 2-3**). Bouleghlimat et al. [34] have reported that the HCl treatment of graphite degraded carbon lattice by weakening and breaking interplanar bonds. Hydronium ion of HCl attacked the surface of graphene sheets and the interplanar structure, which formed defects [34,35]. The acid penetrated further into defective sites, which decreases the van der Waals forces between interlayer bonds of graphite and broke the structures. Thus, it is necessary to optimize the process conditions (temperature and duration) and the concentration of acid used to remove the metal catalyst particles to obtain graphite with few or no structural defects.

Table 2-3. Quantitative parameters of the samples obtained from analysis of the (002) XRD peaks.

Parameters	1300-CC	1300-Ni-GCM	1300-ANi-GCM	Commercial graphite
2θ (°)	24.69	26.45	26.40	26.44
Phase	Amorphous	C (002)	C (002)	C (002)
Interlayer spacing *d* (nm)	0.3602	0.3367	0.3373	0.3362
Degree of graphitisation, *g* (%)	-	84.88	77.91	90.23
Stacking height, *Lc* (nm)	-	51.96	46.36	56.26
Number of stacked C planes (*n*)	-	154.32	137.44	167.31

The formation of graphitic structures from carbon in coconut coir was also confirmed through Raman spectroscopic analysis. The spectra in **Figure 2-5** were analyzed from 1,000 cm^{-1} to 2,850 cm^{-1} to monitor the formation of graphitic structures during catalytic graphitization. The spectrum of sample 1300-CC contained two broad and overlapping peaks that were characteristic of amorphous carbon materials. The peaks at approximately 1,340 cm^{-1} and 1,580 cm^{-1} were assigned to D and G bands, respectively. The D band is indicative of defects or disorder in the structure owing to the presence of sp^3-hybridised carbon [36–38]. The G-band arises from the vibrations of sp^2-hybridised bonds in the hexagonal lattice of graphitic carbon [36–38]. The spectral profile of carbon was considerably different subsequent to catalytic graphitization using the nickel particles. The spectra of samples treated with nickel, 1300-Ni-GCM and 1300-ANiGCM, contained three peaks. Their spectral profiles were similar to that of commercial graphite, and each spectrum contained D and G bands. The peak near 2,690 cm^{-1} in each of these spectra was assigned to the 2D band. The appearance of a 2D band indicates the presence of graphene layers. The spectrum of the 1300-CC sample did not contain a 2D band. The intensity ratio of G and D bands (IG/ID) is indicative of the degree of graphitization

[39] and is commonly used to characterize different types of carbon-based materials [40]. A high IG/ID ratio, which is calculated from the area under the curve of G and D peaks after the fitting process using the Origin software, indicates a high degree of graphitization or a graphitic region within a sample. The G and D bands in each spectrum were deconvoluted into two Lorentzian peaks by carefully fitting using Origin. The fitted peaks are shown in **Figure 2-5**(b–e). The IG/ID ratios and peak parameters used for calculations are shown in **Figure 2-5**(f) and **Figure 2-5**(g), respectively. The IG/ID ratio of the 1300-CC sample was 0.46 ± 0.01. The IG/ID ratio of the 1300- Ni-GCM sample was significantly higher at 1.01 ± 0.04 followed by the slightly change IG/ID ratio of 1300-ANi-GCM. These results indicated that the degree of graphitization in 1300-Ni-GCM and 1300-ANi-GCM samples was higher than it was in the 1300-CC sample. Moreover, the G and D bands in the spectra of the samples treated with nickel were shaped somewhat differently than the corresponding bands in the 1300-CC spectrum. The G and D bands of 1300-Ni-GCM and 1300-ANi-GCM were narrower and more fully resolved than those of 1300-CC. The FWHMs of the G and D bands are compared in **Figure 2-5**(g). Raman analysis provided additional evidence that catalytic graphitization using nickel particles afforded carbon materials with more ordered structures at the same temperature of 1,300 °C and that highly graphitic carbon materials could be obtained from coconut coir. Treatment with acid to remove the nickel particles reduced the degree of graphitization, because the acid degraded the carbon lattice [34].

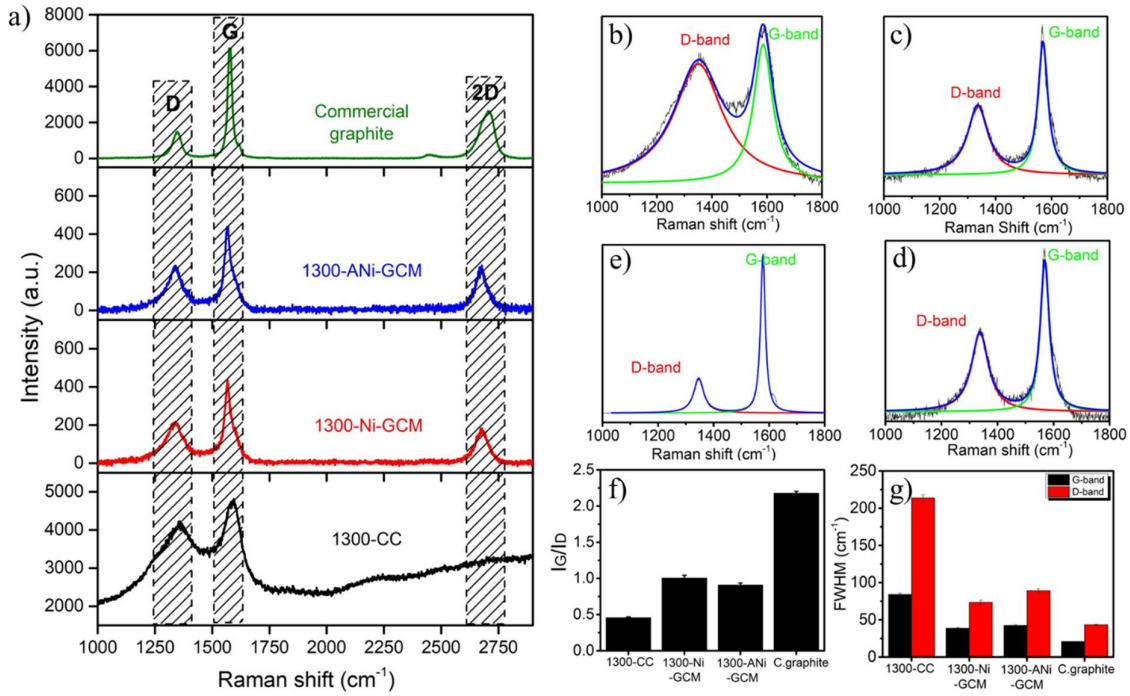

Figure 2-5. (a) Raman spectra of commercial graphite and graphitic carbon obtained from coconut coir. Fitted D- and G-bands of (b) 1300-CC, (c) 1300-Ni-GCM, (d) 1300-ANi-GCM and (e) commercial graphite. (f) IG/ID intensity ratios. (g) G- and D-band FWHMs.

The chemical compositions of 1300-CC, 1300-Ni-GCM and 1300-ANi-GCM were analyzed using XPS. As shown in **Figure 2-6**(a), in the full range XPS wide scan spectra with a binding energy ranging from 0 eV to 900 eV, there are signals only from C and O elements for the surface region of all samples. The Ni signal, which is located at the binding energy of approximately 852.6 eV, does not appear in the XPS spectra of nickel-treated samples. This result may be caused by the low detection depth of XPS. XPS is typically used for a sensitive surface elemental analysis and has the detection depth of ~10 nm [41,42]. However, in our samples, Ni particles are located inside graphene layers with the thickness of graphene layers of approximately 15–20 nm, as shown in **Figure 2-7**(e). **Table 2-4** shows the quantitative analysis of the catalytic graphitization process of carbon materials. Catalytic graphitization process

causes the increasing of surface carbon content from 88.22% to 93.95% and reducing the oxygen content of 11.78% to 6.05%, indicates an increase in the amount of graphitic carbon from 1300-CC to 1300-Ni-GCM. Furthermore, HCl treatment carried out in 1300-Ni-GCM in order to remove the Ni particles causes a reducing the carbon content from 90.5% of 1300-ANi-GCM and an increasing of oxygen content to 9.5%. For the instance, HCl solution plays two important roles for the removal of metal particles and surface modification which may occurred during process. Surface modification by HCl occurs in the form the single bonded oxygen functional group on the carbon surface such as phenol, lactone, and ether by HCl treatment [35,43]. The effects of HCl treatment on carbon materials generally increase the surface oxygen content [34,44]. Furthermore, the C 1s XPS spectra of all samples (**Figure 2-6**(b–d)) were fitted using Gaussian-Lorentzian line shape and Shirley background type. In the fitting process, the FWHM value were set to 1.1–2 eV for C–C peaks, 1.8–2.2 eV for C-O peaks, and 2–3 eV for π-π* transition peaks [45]. The deconvoluted C 1s peaks consist of 3C–C peaks, 3 or 4 oxygenated peaks, and π-π* transition peak [45,46]. The C–C peaks were ascribed to cyclopentane ring atoms within cluster (C–C low), sp^2-hybridised carbon in aromatic C=C bonds, and carbon in C–C sp^3 bonds in the amorphous phase [45]. While the oxygenated peaks were ascribed to phenol or hydroxyl (C–O) groups, C in carbonyl (C=O) groups, C in carboxyl and ester (COO) groups, and C in lactone (O–C=O) groups [15,31,47,48]. The detailed results of C 1s peak fitting are listed in **Table 2-4**.

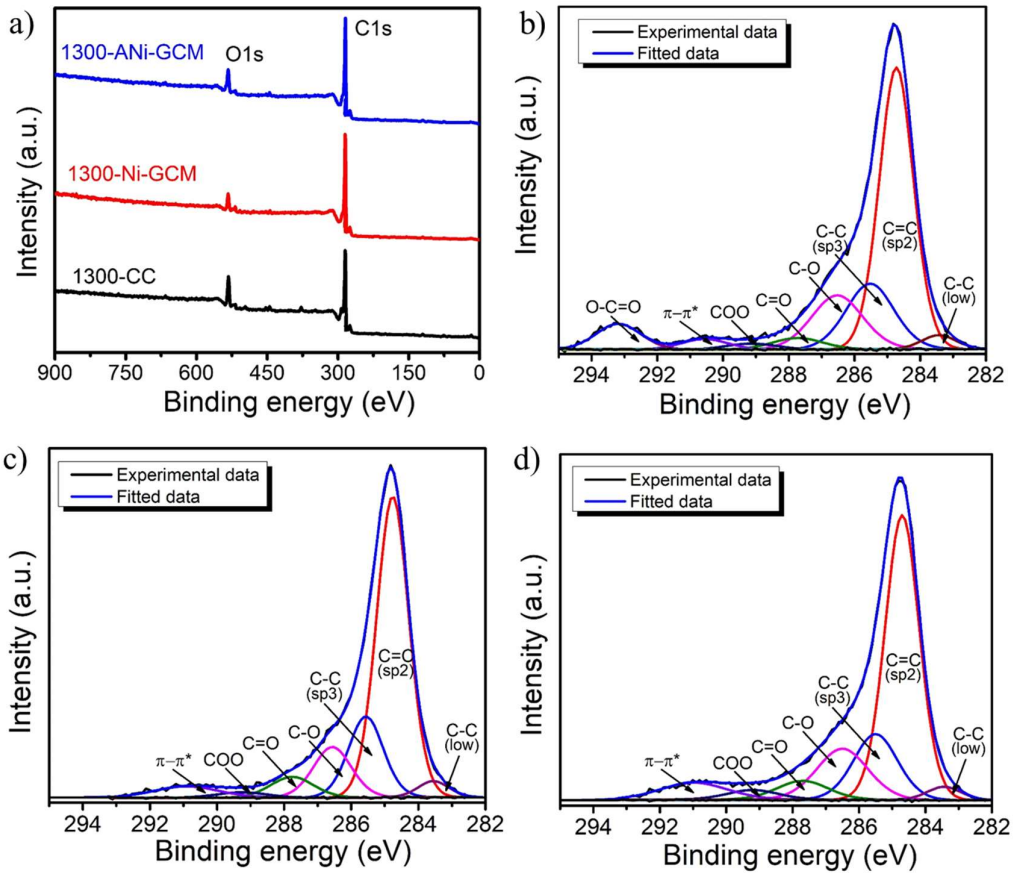

Figure 2-6. (a) XPS wide scan spectra of 1300-CC, 1300-Ni-GCM, 1300-ANi-GCM; C 1s XPS spectra of (b) 1300-CC; (c) 1300-Ni-GCM; and (d) 1300-ANi-GCM.

Table 2-4. XPS quantitative analysis of all samples.

Parameters	1300-CC	1300-Ni-GCM	1300-ANi-GCM
Elemental content (at. %):			
Carbon	88.22	93.95	90.5
Oxygen	11.78	6.05	9.5
Relative areas of C 1s peaks (%):			
C-C low	2.58	2.94	2.51
C-C primary (C=C sp^2)	51.67	57.32	53.22
C–C high (C-C sp^3)	16.93	16.74	15.75
C–O	14.94	11.45	14.29
C=O	3.22	5.35	5.29
COO	1.7	1.71	2.72
π- π*	2.71	4.5	6.23
O-C=O	6.26	-	-

The 1300-Ni-GCM and 1300-ANi-GCM samples contained a higher proportion of sp^2-hybridised C=C bonds than 1300-CC, which indicated that the Ni-treated samples had higher graphite contents. The relative areas of the 1300-Ni-GCM, 1300-ANi-GCM and 1300-CC C=C (sp^2) C1s peaks were 61.66%, 58.08% and 53.15%, respectively. The C=C (sp^2) content of 1300-ANi-GCM was slightly lower than that of 1300-Ni-GCM. The catalytic graphitization process also effected on the presence of π-π* component in both Ni-treated samples as well as the electronic properties. The π-π*component is generated from electrons in C=C sp^2 systems within the graphite plane, the p orbitals can overlap to form a cloud of delocalized electrons above and below the plane [49]. The XPS results were in accordance with the XRD and Raman data, indicating the formation of ordered graphitic structures during catalytic graphitization at 1300 °C, and the 2-M HCl treatment affected on the surface modification.

TEM was used to further investigate the formation of graphitic structures in the carbon materials obtained from coconut coir waste. TEM images of the 1300-CC and 1300-Ni-GCM samples are shown in **Figure 2-7**. The TEM data confirmed that there were structural differences between the samples treated with nickel and the 1300-CC sample pyrolyzed at 1300 °C in the absence of Ni particles. TEM and SAED images of the 1300-CC sample are shown in **Figure 2-7**(a–c). The TEM image of a highly disordered or randomly oriented structure in the 1300-CC sample was typical of an amorphous carbonaceous material. The diffuse halo in the SAED pattern in the inset of **Figure 2-7**(c) confirmed that the carbon in the 1300-CC sample was an amorphous phase. The TEM images in **Figure 2-7**(d–f) indicate the presence of a graphitic structure in the 1300-Ni-GCM sample obtained at the same temperature. The low-magnification TEM image of the 1300-Ni-GCM sample in **Figure 2-7**(d) shows spherical projections with Ni nanoparticles in their cores. The high-resolution TEM (HR-TEM) image shows shells around the Ni nanoparticles with well-defined lattice fringes. The graphitic layers were separated by an interplanar distance of ±0.3367 nm (from the XRD result), which

matched the interlayer spacing between the (002) planes in graphite (ICSD 98-007-6767). This value is closer to the lattice spacing of the (002) crystal plane of commercial graphite powder (0.3362 nm), compare to the graphene-like carbon nanosheets produced from a mixture of melamine and natural soybean oil of 0.35 nm by Shen et al. [47], and graphite-like crystallites from biomass-based activated carbon of 0.354–0.383 nm by Miou et al. [50]. After acid treatment, most of Ni particles were dissolved and removed from the sample, leaving the ordered carbon nanostructure, which can be clearly seen in **Figure 2-7**(g-i). The HR-TEM of 1300-ANi-GCM (**Figure 2-7**(i)) also showed well-defined lattice fringes and small change in the interplanar distance of graphitic material after acid treatment to 0.337 nm (from the XRD result).

The combined results of SAED, XRD, Raman spectroscopy and XPS analysis confirmed that graphitic carbon was produced from catalytic graphitization of amorphous carbon using Ni. The nickel salt ($NiCl_2 \cdot 6H_2O$) used as a catalyst was first decomposed into nickel oxide. It was then reduced to metallic Ni as it reacted with the surrounding amorphous carbon at a certain temperature. Metallic Ni also reacted with amorphous carbon following the dissolution and precipitation process. Dissolved amorphous carbon in metallic Ni precipitated as graphitic carbon around the Ni nanoparticles [16]. Thus, amorphous carbon, derived from coconut coir waste, was successfully converted into graphitic materials via catalytic graphitization at a lower temperature than that of conventional graphite production.

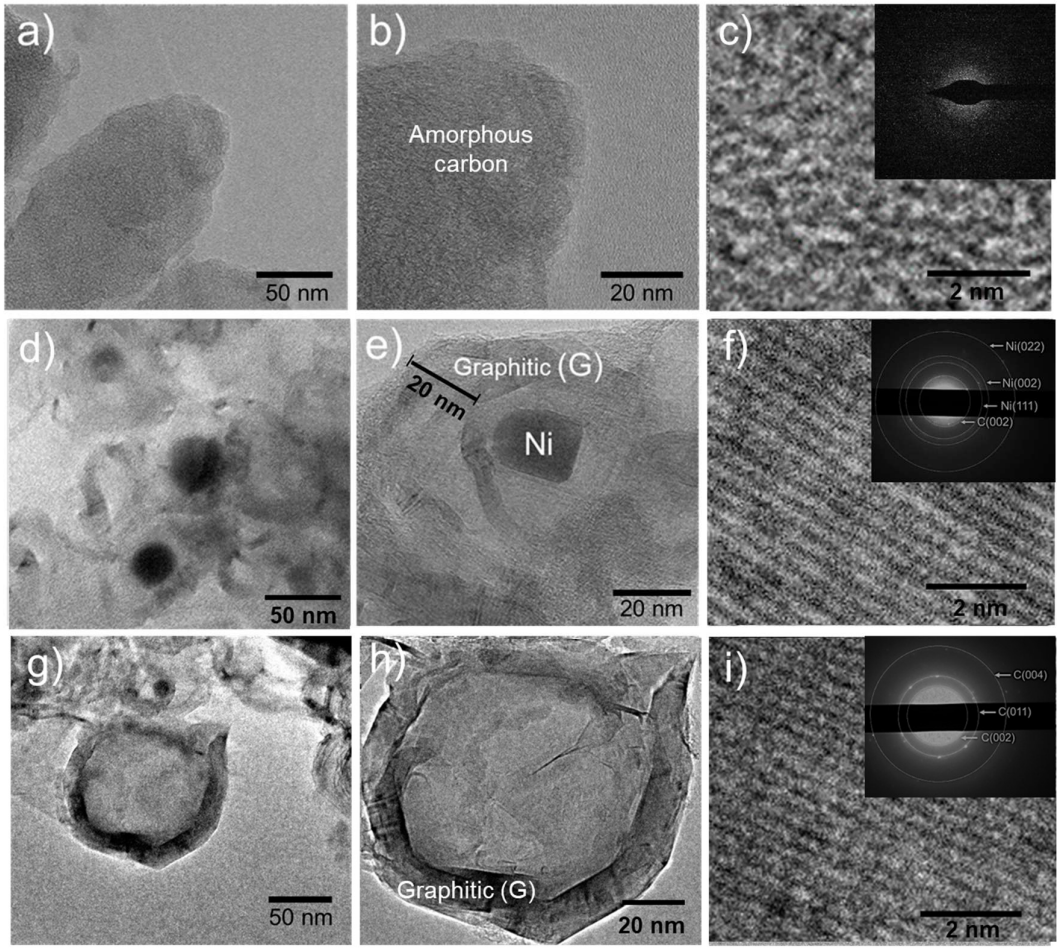

Figure 2-7. Low-magnification TEM micrographs of (a, b) 1300-CC; (d, e) 1300-Ni-GCM; (f, g) 1300-ANi-GCM. HR-TEM images of (c) 1300-CC; (f) 1300-Ni-GCM; (i) 1300-ANi-GCM with SAED patterns shown in the insets.

Electrical conductivity of carbon powder is an important parameter when it applies as electrode material. We also investigated the effect of carbon structure from coconut coir on its electrical conductivity. On the basis of the powder electrical conductivity measurement of all samples at the pressure of 741 kPa, the conductivities of 1300-CC, 1300-Ni-GCM and 1300-ANi-GCM were determined to be 14.97 S/cm, 25.75 S/cm, and 24.75 S/cm, respectively. This directly confirms the formation of graphitic carbon from amorphous structure in coconut coir carbon, which improved its electrical conductivity (by almost 11 S/cm or 1.65–1.72 times).

This also proves that the behavior of electron transport measured as electron conductivity is proportional to the degree of graphitization in carbon material [51]. Furthermore, the acid treatment caused a slight decrease in conductivity of 1300-ANi-GCM by 1 S/cm due to the degradation of its structure, as described in detail in the previous section. However, the highest conductivity value obtained in current research is still lower than that of commercial graphite powder (measured as 100.19 S/cm at 741 kPa). The authors are currently conducting further research on enhancing the structure of coconut coir carbon in order to improve the electrical conductivity as well as the porosity.

2.3.2. Temperature driven structural transition in the nickel-based catalytic graphitization of coconut coir

Morphological characterization

Morphological structure of all samples was observed using SEM, as shown in **Figure 2-8**. Different heating treatment subjected to all samples do not show a significant effect on morphological surface. Morphological structure of coconut coir composed of multi-cellular with polygonal shape arranged lengthwise along the fiber. The greater magnification was also observed pores with diameters of ~1 μm spread in the fiber cell wall. The porous morphological structure provides the advantages for the better mechanical interlocking with matrix when fabricating a porous composite.

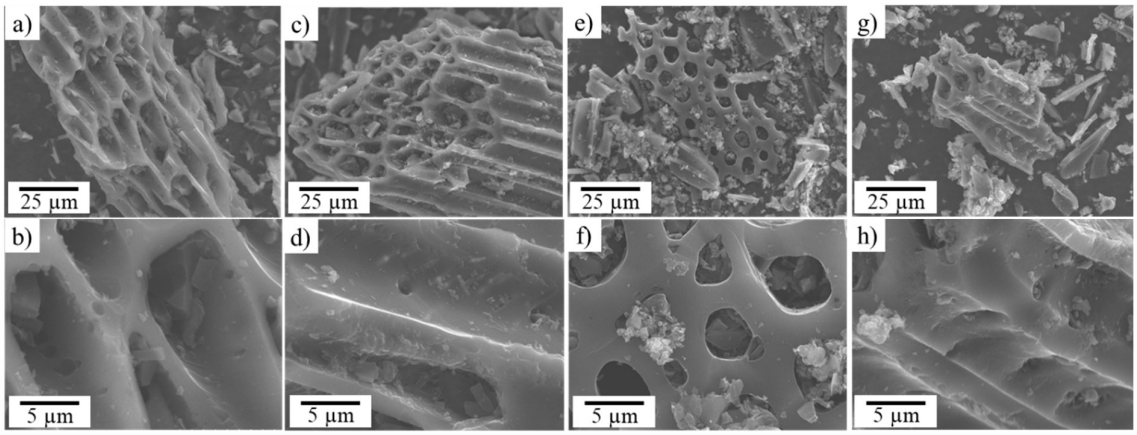

Figure 2-8. SEM image of (a-b) 1000-ANi-GCM, (c-d) 1100-ANi-GCM, (e-f) 1200-ANi-GCM and (g-h) 1300-ANi-GCM.

Structural characterization

The structural changes of samples were characterized using XRD. After acid solution treatment to remove the residual nickel nanoparticles, the XRD pattern of all samples are shown in **Figure 2-9**(a). Two samples (1000-ANi-GCM and 1100-ANi-GCM) contain two broad peaks at 2θ = 23° and 44°, indicating a largely amorphous phase. The 002 peak is becoming higher intensity and sharper, when the temperature increase to 1200 ℃ and 1300 ℃. The 002 peak of 1200-ANi-GCM is initially observed to be getting higher intensity, which indicates the graphitic nanostructure is starting to form at 1200 ℃. Heating treatment from 1000 to 1300 ℃ gradually shifts the peak of 002 to the larger 2θ (26.5) as typical graphite position (ICSD 98–007-6767). This temperature range also give an important effect on the gradual changing in the interlayer spacing of the samples to the ideal graphene layer distance of graphite, 0.3354 nm (**Figure 2-9**(b)). On the contrary, the sharp peak of 002 does not appear in the XRD pattern (**Figure 2-9**(c)) of sample that heat-treated at the same temperature of 1200 ℃ without the nickel catalyst (1200-CC). As shown in **Figure 2-9**(c), 1200-CC exhibit an essentially amorphous pattern with two broad peaks. These results proved that graphitic structure have not

formed on coconut coir carbon at 1200 °C without the presence of nickel catalyst, even at a higher temperature of 1300 °C as reported in detail in our previous work [52].

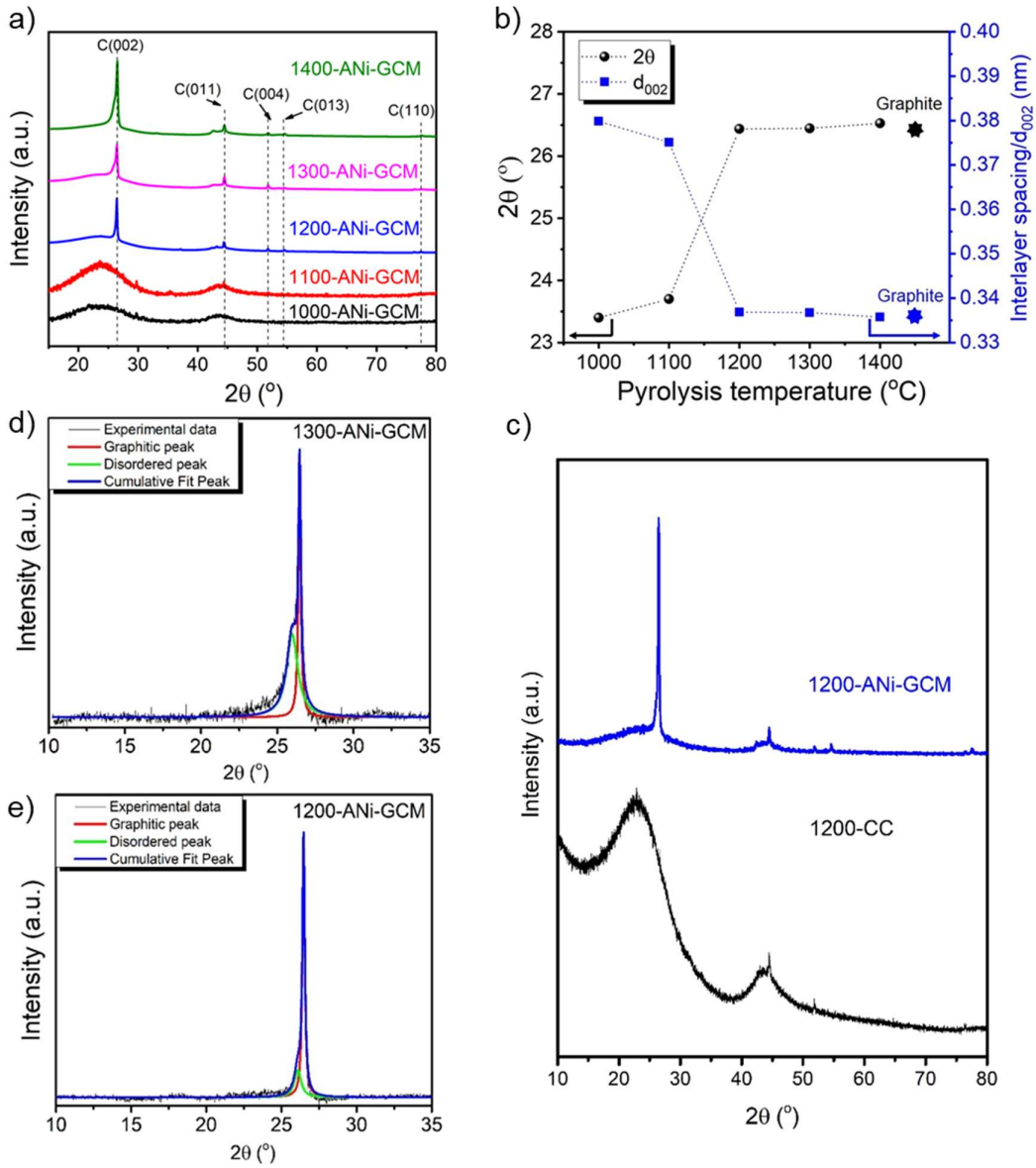

Figure 2-9. (a) XRD patterns, (b) 2θ and d-spacing value of Ni-treated carbon materials (1000-ANi-GCM, 1100-ANi-GCM, 1200-ANi-GCM, 1300-ANi-GCM, 1400-ANi-GCM), (c) XRD patterns of untreated (1200-CC) and Ni-treated (1200-ANi-GCM) samples that were heat-treated at 1200 °C. Fitting d_{002} peaks of (d) 1200-ANi-GCM and (e) 1300-ANi-GCM.

There are two possible catalytic graphitization mechanisms are well known: (i) the dissolution-precipitation mechanism; (ii) metal carbide formation-decomposition mechanism [11]. In dissolution-precipitation mechanism, amorphous carbon is first dissolved into metal catalyst followed by precipitation as graphitic carbon. While in the carbide formation-decomposition mechanism, the graphitization process begins with the formation of metal carbide from amorphous carbon and metal catalyst, and then decomposes at a certain temperature leaving graphitic structure. In our current research, there is no nickel carbide phase indication in all samples system before acid solution treatment, as shown in **Figure 2-10**. In addition, Ni is also known not carbide formers, unlike iron (Fe) and molybdenum (Mo) which can form stable metal carbides [18,53]. Accordingly, the catalytic graphitization mechanism using Ni-based catalyst in our current research might be approaching to the dissolution-precipitation mechanism, ruling out the carbide formation–decomposition mechanism as reported in several works [15,52–54].

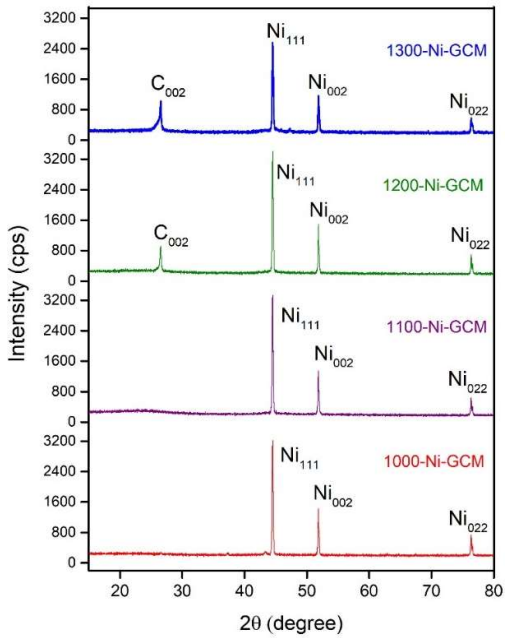

Figure 2-10. XRD patterns of all samples before hydrochloric acid washing to remove the nickel metal in the wide-angle region (10°–80°)

The conversion process of amorphous carbon from coconut coir into graphitic carbon via catalytic graphitization of can be illustrated as in **Figure 2-11**. The process was preceded by dehydration and decomposition of metal precursor ($NiCl_2 \cdot 6H_2O$) at a certain temperature, which produced nickel oxide (NiO), as described in our previous work [52]. With the increase of temperatures, the NiO was reduced to Ni nanoparticles by the amorphous carbon of coconut coir. Due to the random diffusion effect and/or C–Ni interaction [30], the Ni nanoparticles dispersed and moved within a matrix of amorphous carbon. A certain amount of amorphous carbon then dissolves and diffuse in nickel at certain temperature owing to its good solubility in nickel [55]. When the Ni–C system reaches a super saturation condition, graphitic carbon precipitation is formed at the C–Ni interface [30] due to the free energy difference between the amorphous and graphitic carbon [18,53]. The C–Ni interaction is mainly diffusion and dissolution of amorphous carbon onto the bulk of nickel nanoparticles, followed by precipitation of dissolved carbon as form of graphitic carbon around the Ni nanoparticles [52,55].

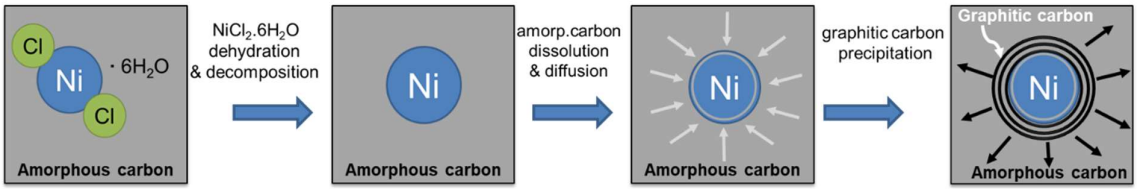

Figure 2-11. Schematic illustration of the catalytic graphitization process. Catalytic graphitization occurs via the Ni dissolution followed by graphitic carbon precipitation around Ni nanoparticles.

Detail analysis of graphitic nanostructure of 1200-ANi-GCM and 1300-ANi-GCM was carried out by the deconvolution of (002) peak into two components as shown in **Figure 2-9**(d) and **Figure 2-9**(e), respectively. Deconvolution of these asymmetric (002) peaks indicate that the graphitic carbon composes of disordered carbon at ~26° and ordered graphitic nanostructure at ~26.5° overlapped for each other. The lower intensity and smaller area at the disordered peak

of 1200-ANi-GCM indicates that this sample is slightly more graphitic than that of 1300-ANi-GCM. The graphitization degree of 1200-ANi-GCM and 1300-ANi-GCM estimated from the equation of $g = (0.3440-d_{002})/(0.3440–0.3354)$ [21,52,56], are 82.16% and 77.91%, respectively, that are slightly lower than that of commercial graphite (90.23%) [52]. This phenomenon also was reported by Sevilla et al. that the graphitization degree of carbons prepared at low heat treatment temperatures is greater than at high temperatures using Fe and Ni catalyst of graphitization [20]. In their opinion, this was due to the presence of higher amount of surface oxygen functional group in the carbons prepared at lower temperatures, which contribute in the reduction of metallic salts and metal nanoparticles formation as catalyst at relatively low temperatures [20]. In addition, the presence of hydrogen which is released during the catalytic graphitization process on biomass charcoal, can lead to higher Ni catalytic activity as reported by Tomita et al. [57]. Furthermore, when heat treatment is carried out at a higher temperature, namely 1400 °C, the degree of graphitization (1400-ANi-GCM=78.41%) increases slightly but not significantly, as shown in **Figure 2-9**(a-b). This is probably due to the solubility of carbon in Ni has reached its maximum at that temperature (maximum solubility of carbon in Ni is about 2.7 at. % at 1326.5 °C [55]). Therefore, higher amount of carbon could interact with Ni, and form higher area of graphitic phase. However, this factor is not too significant effect on the degree of graphitization. Thus, it can be concluded that the optimal temperature for graphitization in current work is 1200 °C.

Analysis using Raman spectroscopy was also carried out to further evaluate the ordered degree of structure for all carbon samples from coconut coir that catalytic graphitized at various temperatures. The spectra shown in **Figure 2-12**(a), were analyzed between 1000 cm^{-1} to 2850 cm^{-1} and provided information on structural transformation of the samples during catalytic graphitization process from temperature 1000 to 1300 °C. It can be seen that the spectrum of sample 1000-ANi-GCM and 1100-ANi-GCM consisted of two broad overlapping peaks at

approximately 1340 cm^{-1} (D-band) and 1580 cm^{-1} (G-band), indicating the existence of amorphous carbon structure. The D-band is related to defects or disorder in the structure due to the presence of sp^3-hybridised carbon [30,55]. While, the G-band arises from the stretching vibrations of sp^2-hybridised bonds in the hexagonal lattice of graphitic carbon or graphite [36,37,58]. The 1200-ANi-GCM and 1300-ANi-GCM spectral profile were observed a significant change. They contained three peaks namely D-band, G-band, and one additional peak located near 2690 cm^{-1} assigned to the 2D band. The presence of a 2D band in the Raman spectrum indicates the improved structure of carbons through the formation of the several layers of graphene [59]. This proves that the graphene layer in this work started to form at temperatures 1200 °C, agreeing with the XRD analysis.

Furthermore, these structural transformations were also observed through quantitative analysis based on the integral area ratio of the D-band and the G-band as well as the full widths at half maximum (FWHM) of G-band. Firstly, the deconvolutions of spectra at around 1100 cm^{-1} to 1800 cm^{-1} of all samples were performed with Gaussian-Lorentzian curve-fitting procedure as shown in **Figure 2-12**(b–e), and then the analytical results of peak fitting were plotted as a function of the heat treatment temperature in **Figure 2-12**(f–h). It can be seen that the Raman spectrum of carbon materials were decomposed into five components namely TPA-band near 1240 cm^{-1} which related to transpolyacetylene-like structures [60], D-band, A-band near 1490 cm^{-1} which is assigned to amorphous structure [22], G-band, and D-band which is a defect-induced feature by intra-valley double resonance scattering process [60].

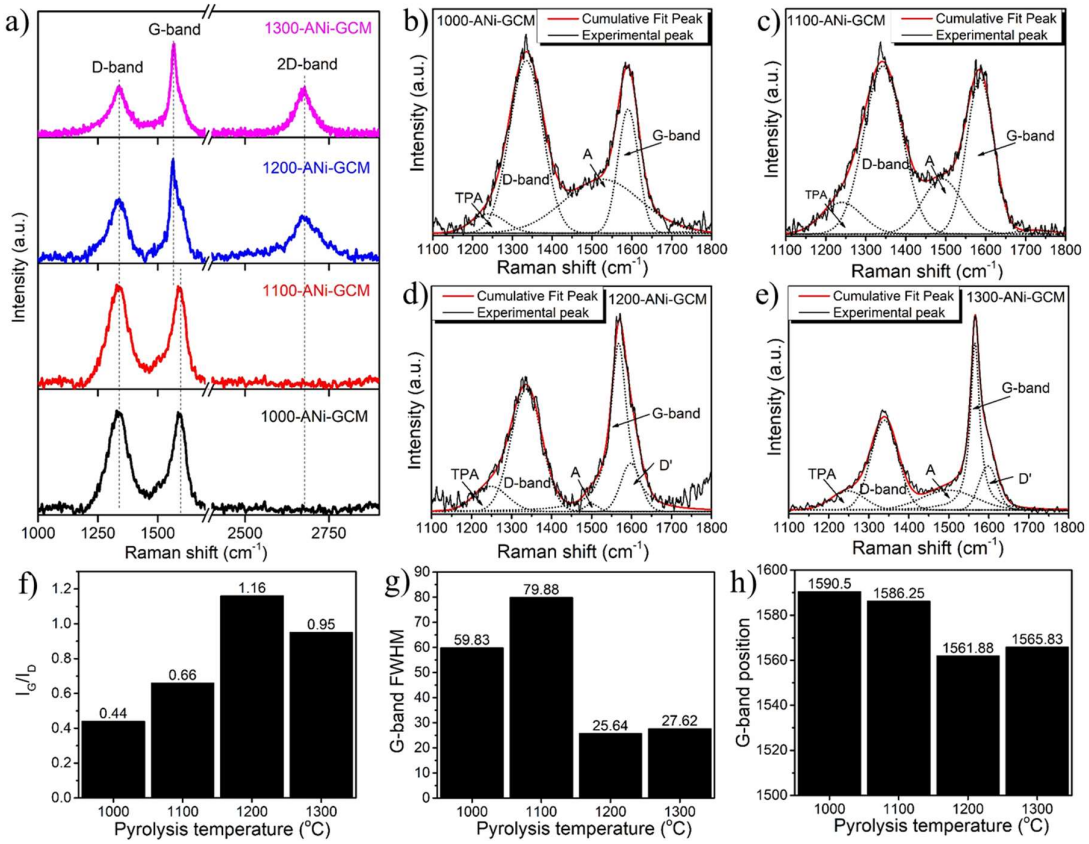

Figure 2-12. (a) Raman spectra of graphitic carbon materials. Deconvolution of Raman spectra for (b) 1000-ANi-GCM, (c) 1100-ANi-GCM, (d) 1200-ANi-GCM, and (e) 1300-ANi-GCM. Raman structural parameters in the function of pyrolysis temperature according to the Raman fitting analysis: (f) IG/ID ratios (area-based), (g) FWHM of G-band, and (h) G-band position.

The intensity of G-band was observed to be dominant at temperature 1200 and 1300 °C, while the intensity of A-band and D-band decreased in the temperature, indicating the removal of amorphous carbon and disordered structure followed by initiation of crystal growth during the graphitization process. **Figure 2-12**(f) shows the integral area ratio between the G-band and D-bands (IG/ID) obtained from the fitted data of Raman spectra as a function of heat treatment temperature. A significant increase of IG/ID are observed from temperature 1000 °C to 1200 °C, followed by a slight decreasing to 1300 °C. It indicates that 1200-ANi-GCM and 1300-ANi-GCM have higher of crystalline structure than that of 1000-ANi-GCM and 1100-ANi-GCM.

Then, the FWHM and position of G-band are also used to monitor the structural change in this work. Previous research has reported that the FWHM of G-band represented of the in-plane defects and lateral dimension, while the G-band position was dominantly affected by the number of graphite layers [60,61]. As shown in **Figure 2-12**(g) and **Figure 2-12**(h), the decreasing trend in the FWHM of G-band, as well as the G-band position from temperature 1100 °C to 1200 °C, represent an improved the crystalline structure with the disappearance of the defects, suggesting the in-plane homogenization process for producing ordered graphite. In addition, the FWHM of G band and IG/ID ratio were proved to specify semi-graphite and graphite [62], the range of IG/ID area ratio > 1.176 and G-band FWHM < 23.8 cm^{-1} correspond to the range of d_{002}-spacing < 0.336 nm, which classify the highly ordered graphite. In this work, sample 1200-ANi-GCM has the highest IG/ID (1.16), smallest G-band FWHM (25.64 cm^{-1}), and d_{002} (0.3369) which closed to being classified into highly ordered graphite. In other word, the sample is a graphitic carbon, which contain of the ordered graphite and smaller amount of disordered carbon structures. This graphitic structure formation is also evidenced by G-band position as shown in **Figure 2-12**(h). It can be seen that the G-band position decreases from 1590.5 cm^{-1} to 1561.88 cm^{-1} along the heat treatment temperature 1000 to 1200 °C. Moreover, sample 1200-ANi-GCM and 1300-ANi-GCM, which proved to have been formed a graphitic structure from XRD data, show a lower Raman shift than that of 1000-ANi-GCM and 1100-ANi-GCM. This suggests the decreasing trend seen here corresponds to the increased amount of the graphitic structure as well as the degree of graphitization on the sample [60,61], in line with the XRD results presented in the previous section.

The surface chemical composition analysis using XPS spectroscopy was carried out for the quantitative analysis of the carbon atoms compositions including the sp^2/sp^3 ratio of samples during the catalytic graphitization from 1000 to 1300 °C, as proved in previous studies [15,16,52,59]. The XPS survey spectra of all samples with the binding energy from 0 to 900 eV as shown in

Figure 2-13 show mainly the presence of C1s and O1s photoemission peak, indicating the carbon material only consists of carbon and oxygen components. The deconvoluted high-resolution C 1s region spectra of all samples (1000-ANi-GCM, 1100-ANi-GCM, 1200-ANi-GCM, and 1300-ANi-GCM) are shown in **Figure 2-13**(d–g). It can be seen that the C 1s spectrum of all samples were fitted to 7 components using Gaussian-Lorentzian line shape and Shirley background type as proposed by Smith et al. [41]. The 7 components are 3C–C peaks, 3 oxygenated peaks, and π-π* transition peak, as identified by the previous study [45,46]. In the fitting process, the FWHM value were set to 1.1–2 eV for C–C peaks, 1.8–2.2 eV for C–O peaks, and 2–3 eV for π- π* transition peaks [45]. The C–C peaks were assigned to cyclopentane ring atoms within cluster (C–C low), sp^2-hybridised carbon in aromatic (C=C bonds), and carbon in C–C sp^3 bonds in the disordered phase. Whereas, the oxygenated peaks were ascribed to phenol or hydroxyl (C–O) groups, carbonyl (C=O) groups, C in carboxyl and ester (COO) groups. The results of area-fraction calculation under each peak deconvolution of C 1s are summarized in **Figure 2-13**(b–c). The sp^2/sp^3 ratio amount of the samples during catalytic graphitization can be corresponded to the C=C/C-C ratio. The sp^3 is a hybridization in the diamond structure, while sp^2 is a hybridization of two-dimensional layered graphite structure [63,64]. As shown in **Figure 2-13**(b), the C=C/CC ratio tend to increase as increasing temperature from 1000 to 1200 °C, then decreased slightly at 1300 °C. It indicates that the heating treatment up to 1200 °C causes highly increasing amount of graphitic carbon. These results are good agreement with the XRD and Raman analysis that transformation of carbon structure from amorphous to the graphitic nanostructures are formed at 1200 °C. Surely, the presence of Ni-metal catalyst assigned good contribution on the transformation of carbon structure at relatively low temperature.

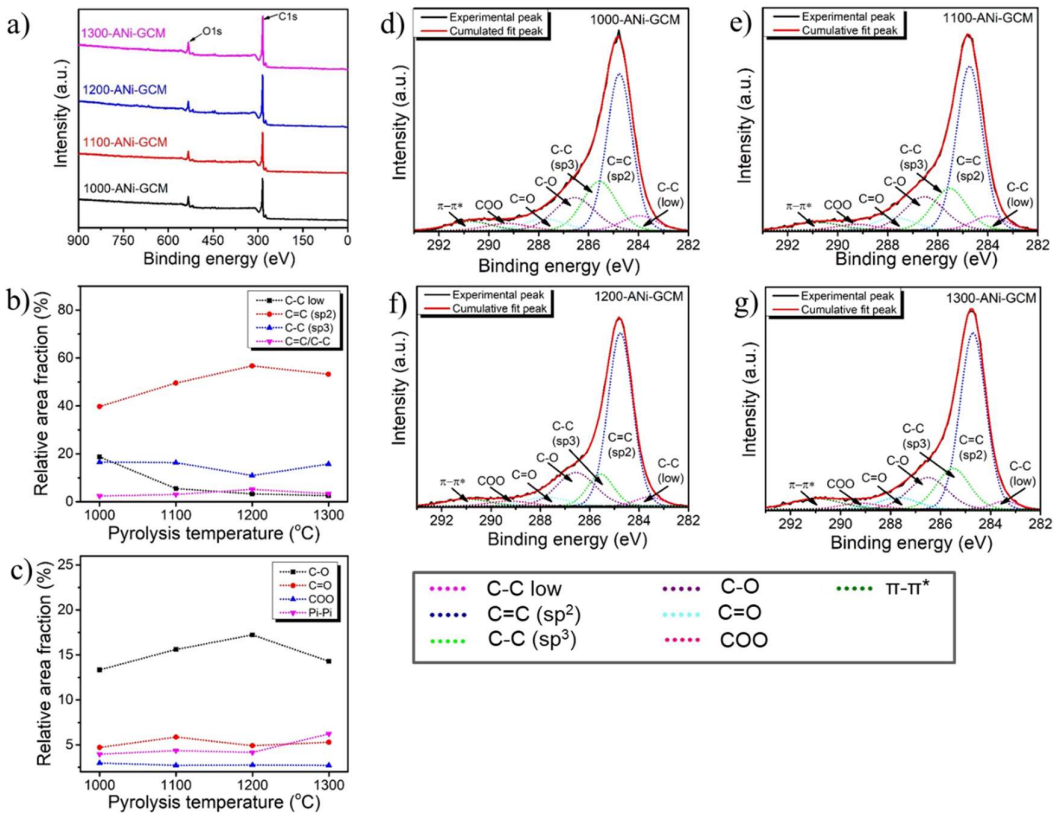

Figure 2-13. (a) XPS wide scan spectra, (b-c) relative area fractions of deconvoluted C1s peak and C=C/C-C ratios of graphitic carbon materials obtained from coconut fiber in the pyrolysis temperature range of 1000-1300 °C. Deconvoluted XPS C1s peak for (d) 1000-ANi-GCM, (e) 1100-ANi-GCM, (f) 1200-ANi-GCM, and (g) 1300-ANi-GCM.

Intensive investigation on the microstructural change and the formation of graphitic nanostructures in the carbon materials were characterized by TEM coupled with selected area electron diffraction pattern (SAED) (**Figure 2-14**(a–l)). As agreeable results of XRD, Raman, and XPS analysis, the TEM images of 1000-ANi-GCM and 1100-ANi-GCM samples (**Figure 2-14**(a–f)) which heat treated below 1200 °C exhibited the disordered microstructures or randomly oriented structure typical of amorphous carbonaceous material. The diffuse ring in the SAED pattern as shown in **Figure 2-14**(c) and (f) confirmed that 1000-ANi-GCM and 1100-ANi-GCM samples are still in an amorphous phase. This indicates that the graphitic

nanostructure of the coconut coir carbon has not been able to form in the presence of Ni-nanoparticles below 1200 °C. On the other hand, completely different TEM and SAED images were observed from the 1200-ANi-GCM and 1300-ANi-GCM samples, as shown in **Figure 2-14**(g–l). The low-magnification TEM images of both samples in **Figure 2-14**(g) and **Figure 2-14**(j) show the formation of ribbon-like graphitic nanostructures. Detailed observations focused on these ribbon-like graphitic nanostructures using HRTEM shows the well-defined lattice fringes throughout the entire sample. The microstructure of both samples was observed to be composed of multilayer graphene sheets which separated by an interplanar distance of ±0.3369 and ± 0.3376 nm (from the XRD result) for 1200-ANi-GCM and 1300-ANi-GCM, respectively. Thus, the spot patterns that appeared in the SAED images (**Figure 2-14**(i–l)) for both samples confirmed that crystalline ordering or graphitic nanostructures are formed in these samples. The multilayer graphene sheets are dominantly formed around the Ni-nanoparticles in amorphous carbon at certain temperatures as an effect of catalytic graphitization including the reaction of Ni-nanoparticles with amorphous carbon according to the mechanism described above. These combined results analysis of XRD, Raman spectroscopy, XPS analysis, and TEM observation proved that amorphous carbon from coconut coir were successfully converted into graphitic carbon nanostructure through a catalytic graphitization using Ni-metal catalyst at temperatures starting from 1200 °C. The initial temperature of the graphitic structure formation in the current work is slightly different compared to the results reported in previous works. Sevilla et al. reported that the graphite-like structure started to form at the 700–730 °C range from glucose-based hydro-char using Ni-catalyst [65]. The use of hydro-char supports a good dispersion of the catalyst nanoparticles, probably due to the abundance of surface oxygen functional groups and give effect to the catalytic graphitization process [65]. While, Johnson et al. proved that 1000 °C was the starting temperature of graphitization, by employing a Ni-catalyst solution on raw wood samples of red oak and beech [66]. Hydrogen gas produced during the heat treatment process of

Ni-impregnated raw wood samples [18] leads to the possibility of increasing the catalytic activity and promotes graphitization reaction efficiently [53]. From these studies, we thus hypothesize that the catalytic effectiveness of graphitization is highly dependent on the choice of precursor carbon and the impregnation method.

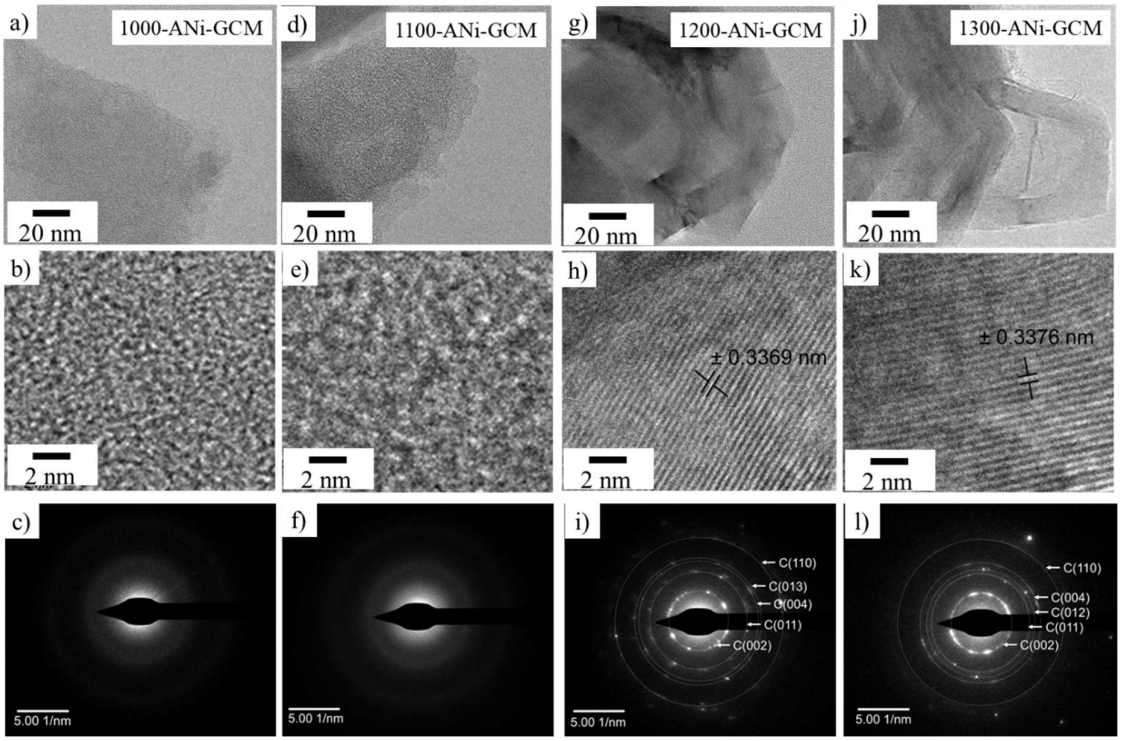

Figure 2-14. Low magnification TEM, HRTEM, and SAED images of (a-c) 1000-ANi-GCM, (d-f) 1100-ANi-GCM, (g-i) 1200-ANi-GCM, and (j-l) 1300-ANi-GCM samples.

2.3.3. Electrochemical Characteristic Analysis as Anode of LIBs.

In order to assess the potential use of the graphitic carbon derived from coconut coir as anode material in LIBs, galvanostatic CD and CV tests were carried out in a half-cell configuration on untreated (1200-CC) and Ni-treated samples, which were heat treated at 1200 °C (1200-ANi-GCM). The tests assisted in evaluating its electrochemical performance and lithium-ion storage mechanism. The first three cycles of galvanostatic discharge (lithiation)−charge (delithiation) profiles of all samples tested at a current density of 0.05 C are

depicted in **Figure 2-15**(a-c). It can be noticed that there are differences in the shape of the CD curve in both carbon sample derived from coconut coir, indicating differences in the lithium-ion storage mechanism. The 1200-CC sample displays a sloping profile with specific capacity up to 75.25 mA h/g (**Figure 2-15**(a)). This sloping profile indicates that Li^+ ions are dominantly stored at the surface of micropores and defect and edge sites, with a minor contribution to the graphitic layers [6,67]. Due to its amorphous structure and very low surface area, the 1200-CC electrode showed the low specific. Meanwhile, 1200-ANi-GCM (**Figure 2-15**(b)) exhibit a CD curve with a low-voltage plateau profile (<0.25 V vs Li/Li^+) and high-voltage sloping profile substantially identical to commercial graphite (**Figure 2-15**(c)). This profile shows that the ion storage mechanism of 1200-ANi-GCM sample is dominated by ion diffusion in the graphitic interlayer, which is comparable to the storage mechanism of commercial graphite, as a result of the existence of graphitic structures in the samples. This sample shows higher specific capacity (192.56 mA h/g) compared to 1200-CC sample, which can be attributed to the higher degree of graphitic structure and surface area. The differential capacity curves (dQ/dV) of charge/delithiation process shown in **Figure 2-15**(d-f) are used to provide further insight about the ion storage mechanism of each sample. It can be seen in the dQ/dV curve that the 1200-CC **Figure 2-15**(d) electrode shows several anodic peaks located mostly in the high-voltage range and weak peaks in the low-voltage region. The peaks detected at the low-voltage region (<0.25 V vs Li/Li^+) are generally thought to be Li extraction from the graphitic interlayer because the lithiation and delithiation of this site occur at a very low potential [68–71]. Other big peaks located in the high-voltage region (>0.25 vs Li/Li^+) were associated with the delithiation of the adsorbed Li+ ion at the micropore surface, defect sites, and edges [70–72]. This validates the structural analysis findings that 1200-CC is an amorphous carbon with numerous defects, edges, functional groups, randomly orientated structure, and micro voids that provide a number of distinct storage sites [72]. On the contrary, the Ni-catalytic graphitized sample, 1200-ANi-GCM

shows different lithium-ion storage characteristics. As shown in **Figure 2-15**(e), the well-defined anodic peaks in the low-voltage region look stronger and identical to those of commercial graphite (**Figure 2-15**(e)), revealing that this sample has a better graphitic structure, allowing for greater lithium extraction from this site. In the high-voltage region, peaks suggesting the delithiation of Li^+ ions adsorbed on the micropore surface, defect sites, and edges were also detected. This is consistent with the BET data, which indicate that 1200-ANi-GCM has a pore structure with a surface area of 337.45 m^2/g as a result of the Ni-carbon etching reaction.

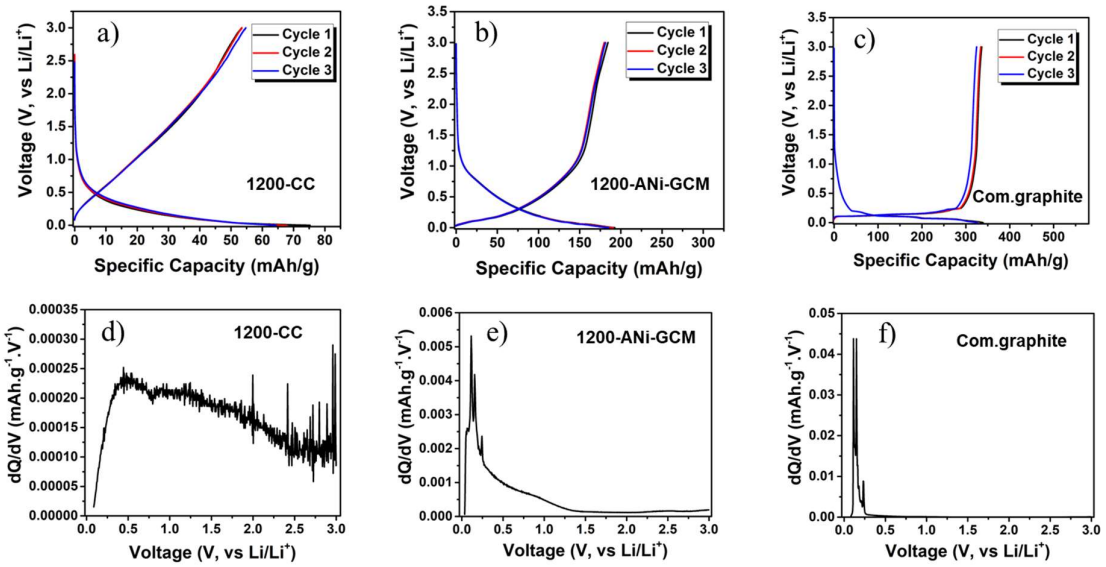

Figure 2-15. Charge−discharge plots for the first 3 cycles and dQ/dV plot of the third cycle charge/delithiation process for (a-b) 1200-CC, (c-d) 1200-ANi-GCM, and (e-f) commercial graphite sample electrodes at 0.05 C (0.0001−3.00 V, vs Li/Li+).

In order to evaluate further the electrochemical properties of all carbon electrodes, the rate performance at increasing rates (0.05−1 C) and cycling stability at a constant rate (0.5 C) over a voltage range of 0.0001−3.00 V vs Li/Li^+ were also performed. As illustrated in **Figure 2-16**(a), the specific capacity of all samples declines as the current density increases because the ions in the electrolyte are limited by diffusion and do not have enough time to reach all

storage sites of the carbon electrodes [73]. Then, when the current density is restored to 0.05C, the specific capacity of each sample almost recovers to its initial specific capacity at 0.05 C, demonstrating that the materials exhibit good rate performance. The 1200-CC electrode exhibits the lowest specific capacity at all current densities than the others due to its unfavorable structure as a lithium-ion storage as described previously. While, the 1200-ANi-GCM electrode shows higher specific capacity than 1200-CC at each stage owing to its high graphitic and porous structure as described above. The micro-/mesoporous structure possessed by 1200-ANi-GCM, which is indicated by its higher surface area values compared to 1200-CC, according to the BET analysis. Micropores provide an extra storage site to accommodate large amounts of Li^+ ions, allowing the capacity to be increased. On the other hand, mesopores contribute to the acceleration of the ion diffusion process as well as the increase in power density by offering free Li^+ ion transmission pathways [73,74]. Moreover, the specific capacity of commercial graphite electrode decreased significantly as current rates were increased. Indeed, its capacity is lower than that of the 1200-ANi-GCM at rates of 0.5 and 1 C. The poor performance of graphite at high current rates is well known to be related to the slow solid-state diffusion of Li^+ ion in graphite and the lack of a porous structure [71,74–76].

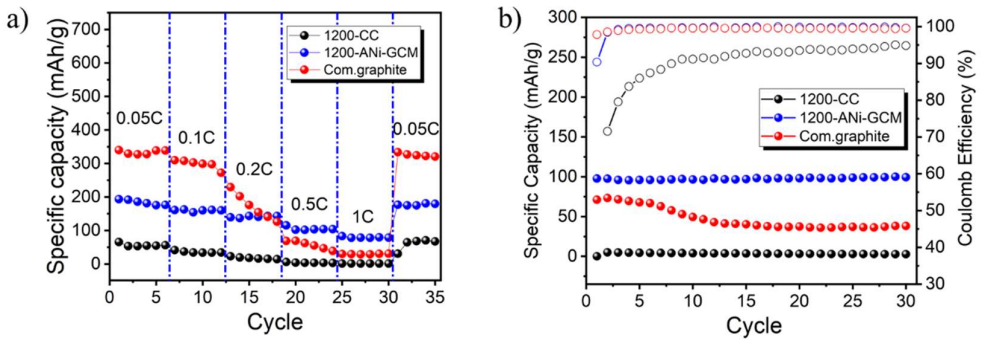

Figure 2-16. (a) C-rate performance of 1200-CC, 1200-ANi-GCM, and commercial graphite at increasing current densities from 0.05 to 1 C and then back to 0.05 C to demonstrate rate

capability, (b) cycling performance and Coulombic efficiency at 0.5 C current density for 30 cycles (1 C = 372 mA/g).

Furthermore, the cycling performances completed with Coulombic efficiency of all prepared carbon electrodes at a constant rate of 0.5 C are depicted in **Figure 2-16**(b). It can be seen that carbon electrodes prepared from coconut coir (1200-ANi-GCM) demonstrated better cycling performance after 30 cycles compared to commercial graphite. Among the samples tested, the 1200-ANi-GCM sample showed the highest specific capacity, with an initial capacity of 97.721 mA h/g and a capacity retention ratio of 101.63%. While, commercial graphite powder appears to have a lower cycling performance (53.54%) and a lower capacity (71.107 mA h/g) than 1200-ANi-GCM. This may be due to the highly ordered structure of commercial graphite with the highest graphitization degree and the narrowest interlayer spacing among the carbon samples investigated, which poses an unfavorable effect for the lithium-ion intercalation and deintercalation processes at a relatively high current rate [71,75–78]. Meanwhile, the 1200-CC showed the smallest initial capacity of 5.01 mA h/g, related to its poor structure and surface area. The good lithium-ion cell performance reported above demonstrates that coconut coir has potential as an alternative anode material for energy storage systems that are sustainable, reasonably priced, and environmentally friendly.

2.4 Conclusions

This chapter demonstrates an approach for producing high graphitic carbon materials from renewable resources of coconut coir waste using a simpler and lower-energy process than that used for conventional graphite production. Through nickel-based catalytic graphitization, the amorphous charcoal obtained by the carbonisation of coconut coir was converted into a graphitic nanostructure at an initial heat treatment temperature of 1200 °C for three hours. A

well-ordered graphitic nanostructure with inter-planar distance in the range between 0.3369 nm - 0.3376 nm, which is close to the theoretical value of pure graphite (0.3354 nm), was clearly observed formed near Ni particles. The formation of graphitic layers was also proven by the XRD, Raman spectroscopy and TEM/SAED results. With the graphitization degree of the carbon structure (1200-ANi-GCM) about 82.16%, the graphitic structure present good electrochemical performance with a specific capacity of 192.6 mAh/g, a good cycling stability (the specific capacity remained 99.32 mAh/g after 30 cycles at 0.5C rate), and excellent rate performance (the specific capacity recovered when the rate was from 0.05C to 1C and then returned to 0.05C). The relatively good electrochemical performance of this graphitic carbon can be strongly utilized as an alternative material for LIB anodes with a low-energy process and renewable raw materials. This simple and efficient method for converting waste biomass into graphitic carbon material for energy storage applications is a promising technology to address the global challenge without environmental deterioration.

2.5 References

[1] S. P. S. Badwal, S. S. Giddey, C. Munnings, A. I. Bhatt, A. F. Hollenkamp, *Front. Chem.* **2014**, *2*, 1–28.

[2] Z. P. Cano, D. Banham, S. Ye, A. Hintennach, J. Lu, M. Fowler, Z. Chen, *Nat. Energy* **2018**, *3*, 279–289.

[3] O. Velázquez-Martínez, J. Valio, A. Santasalo-Aarnio, M. Reuter, R. Serna-Guerrero, *Batteries* **2019**, *5*, 1–33.

[4] Y. Mekonnen, A. Sundararajan, A. I. Sarwat, in *SoutheastCon 2016*, **2016**, pp. 1–6.

[5] J. Xu, Y. Dou, Z. Wei, J. Ma, Y. Deng, Y. Li, H. Liu, S. Dou, *Adv. Sci.* **2017**, *4*, 1700146 (1–14).

[6] L. Han, X. Zhu, F. Yang, Q. Liu, X. Jia, *Powder Technol.* **2021**, *382*, 40–47.

[7] S. Huang, H. Guo, X. Li, Z. Wang, L. Gan, J. Wang, W. Xiao, *J. Solid State Electrochem.* **2013**, *17*, 1401–1408.

[8] M. Shi, C. Song, Z. Tai, K. Zou, Y. Duan, X. Dai, J. Sun, *Fuel* **2021**, *292*, 120250.

[9] I. Cameán, A. B. Garcia, *J. Power Sources* **2011**, *196*, 4816–4820.

[10] S. M. Lee, D. S. Kang, J. S. Roh, *Carbon Lett.* **2015**, *16*, 135–146.

[11] H. Li, H. Zhang, K. Li, J. Zhang, M. Sun, B. Su, *Fuel* **2020**, *279*, 118531.

[12] E. Thompson, A. E. Danks, L. Bourgeois, Z. Schnepp, *Green Chem.* **2015**, *17*, 551–556.

[13] A. Gomez-Martin, J. Martinez-Fernandez, M. Ruttert, A. Heckmann, M. Winter, T. Placke, J. Ramirez-Rico, *ChemSusChem* **2018**, *11*, 2776–2787.

[14] S. S. Li, J. K. Wang, Q. Zhu, X. W. Zhao, H. J. Zhang, *Solid State Phenom.* **2018**, *281 SSP*, 807–812.

[15] C. Chen, K. Sun, A. Wang, S. Wang, J. Jiang, *BioResources* **2018**, *13*, 3165–3176.

[16] M. Sevilla, A. B. Fuertes, *Chem. Phys. Lett.* **2010**, *490*, 63–68.

[17] K. Wang, Y. Cao, X. Wang, P. R. Kharel, W. Gibbons, B. Luo, Z. Gu, Q. Fan, L. Metzger, *Energy* **2016**, *101*, 9–15.

[18] Q. Yan, J. Li, X. Zhang, E. B. Hassan, C. Wang, J. Zhang, Z. Cai, *J. Nanoparticle Res.* **2018**, *20*, 1–20.

[19] I. Mochida, R. Ohtsubo, K. Takeshita, H. Marsh, *Carbon N. Y.* **1980**, *18*, 117–123.

[20] M. Sevilla, A. B. Fuertes, *Carbon N. Y.* **2006**, *44*, 468–474.

[21] C. N. Barnakov, G. P. Khokhlova, A. N. Popova, S. A. Sozinov, Z. R. Ismagilov, *Eurasian Chem. J.* **2015**, *17*, 87–93.

[22] M. W. Smith, I. Dallmeyer, T. J. Johnson, C. S. Brauer, J. S. McEwen, J. F. Espinal, M. Garcia-Perez, *Carbon N. Y.* **2016**, *100*, 678–692.

[23] and F. D. Nanik Indayaningsih, Yuyun Irmawati, *ARPN J. Eng. Appl. Sci.* **2016**, *11*, 4040–4044.

[24] F. Destyorini, A. Subhan, N. Indayaningsih, B. Prihandoko, A. Z. Syahrial, *Int. J. Technol.* **2016**, *7*, 1283–1290.

[25] F. Destyorini, Y. Irmawati, H. Widodo, D. S. Khaerudini, N. Indayaningsih, *J. Eng. Technol. Sci.* **2018**, *50*, 409–419.

[26] S. K. Mishra, S. B. Kanungo, *J. Therm. Anal.* **1992**, *38*, 2417–2436.

[27] J. Kang, X. Duan, C. Wang, H. Sun, X. Tan, M. O. Tade, S. Wang, *Chem. Eng. J.* **2018**, *332*, 398–408.

[28] J. Yuan, Y. Zhu, L. Li, *Chem. Commun.* **2014**, *50*, 6641–6644.

[29] Y. Koltypin, A. Fernandez, T. C. Rojas, J. Campora, P. Palma, R. Prozorov, A. Gedanken, *Chem. Mater.* **1999**, *11*, 1331–1335.

[30] R. Anton, *Carbon N. Y.* **2008**, *46*, 656–662.

[31] L. Zou, B. Huang, Y. Huang, Q. Huang, C. Wang, *Mater. Chem. Phys.* **2003**, *82*, 654–662.

[32] M. Käärik, M. Arulepp, M. Karelson, J. Leis, *Carbon N. Y.* **2008**, *46*, 1579–1587.

[33] S. Tao, Y. Wang, D. Shi, Y. An, J. Qiu, Y. Zhao, Y. Cao, X. Zhang, *J. Mater. Chem. A* **2014**, *2*, 12785–12791.

[34] E. Bouleghlimat, P. R. Davies, R. J. Davies, R. Howarth, J. Kulhavy, D. J. Morgan, *Carbon N. Y.* **2013**, *61*, 124–133.

[35] V. A. Coleman, R. Knut, O. Karis, H. Grennberg, U. Jansson, R. Quinlan, B. C. Holloway, B. Sanyal, O. Eriksson, *J. Phys. D. Appl. Phys.* **2008**, *41*, 062001.

[36] P. K. Chu, L. Li, *Mater. Chem. Phys.* **2006**, *96*, 253–277.

[37] A. C. F. and J. Robertson, *Phys. Rev. B* **2000**, *61*, 632–645.

[38] J. R. Dennison, M. Holtz, *Spectroscopy* **1996**, *11*, 38–46.

[39] X. Zhang, H. Li, K. Zhang, Q. Wang, B. Qin, Q. Cao, L. Jin, *J. Electrochem. Soc.* **2018**, *165*, A2084–A2092.

[40] L. Bokobza, J.-L. Bruneel, M. Couzi, *C* **2015**, *1*, 77–94.

[41] T. Nunney, R. White, *Micros. Today* **2011**, 22–29.

[42] Jean-Numa Gillet and Michel Meunier, *J. Phys. Chem. B* **2005**, *109*, 8733–8737.

[43] Fazel G. Jahromi and Ahmad Ghahreman, *Colloids Interfaces* **2019**, *3*, 1–16.

[44] S. Wang, G. Q. Lu, *Carbon N. Y.* **1998**, *36*, 283–292.

[45] M. Smith, L. Scudiero, J. Espinal, J. S. McEwen, M. Garcia-Perez, *Carbon N. Y.* **2016**, *110*, 155–171.

[46] R. Blume, D. Rosenthal, J. P. Tessonnier, H. Li, A. Knop-Gericke, R. Schlögl, *ChemCatChem* **2015**, *7*, 2871–2881.

[47] Z. Shen, C. Liu, C. Yin, S. Kang, Y. Liu, Z. Ge, Q. Xia, Y. Wang, X. Li, *Carbon N. Y.* **2019**, *145*, 751–756.

[48] D. Fitria, L. A. Al Baroroh, F. Destyorini, W. B. Widayatno, M. I. Amal, A. S. Wismogroho, in *J. Phys. Conf. Ser.*, **2018**.

[49] A. Theodosiou, B. F. Spencer, J. Counsell, A. N. Jones, *Appl. Surf. Sci.* **2020**, *508*, 144764.

[50] M. Miao, S. Zuo, Y. Zhao, Y. Wang, H. Xia, C. Tan, H. Gao, *Carbon N. Y.* **2018**, *140*, 504–507.

[51] S. Shi, X. Zhou, W. Chen, M. Chen, T. Nguyen, X. Wang, W. Zhang, *RSC Adv.* **2017**, *7*, 44632–44638.

[52] F. Destyorini, Y. Irmawati, A. Hardiansyah, H. Widodo, I. N. D. Yahya, N. Indayaningsih, R. Yudianti, Y. I. Hsu, H. Uyama, *Eng. Sci. Technol. an Int. J.* **2020**, *24*, 514–523.

[53] Y. Kodama, K. Sato, K. Suzuki, Y. Saito, T. Suzuki, T. J. Konno, *Carbon N. Y.* **2012**, *50*, 3486–3496.

[54] A. A. Galuska, H. H. Madden, R. E. Allred, *Appl. Surf. Sci.* **1988**, *32*, 253–272.

[55] T. Kim, J. Lee, K. H. Lee, *RSC Adv.* **2016**, *6*, 24667–24674.

[56] I. Major, J. M. Pin, E. Behazin, A. Rodriguez-Uribe, M. Misra, A. Mohanty, *Green Chem.* **2018**, *20*, 2269–2278.

[57] A. Tomita, K. Yoshida, Y. Nishiyama, Y. Tamai, *Carbon N. Y.* **1972**, *10*, 601–611.

[58] D. B. Schuepfer, F. Badaczewski, J. M. Guerra-Castro, D. M. Hofmann, C. Heiliger, B. Smarsly, P. J. Klar, *Carbon N. Y.* **2020**, *161*, 359–372.

[59] X. Zhang, K. Zhang, H. Li, Q. Wang, L. Jin, Q. Cao, *J. Appl. Electrochem.* **2018**, *48*, 415–426.

[60] C. Hu, S. Sedghi, A. Silvestre-albero, G. G. Andersson, A. Sharma, P. Pendleton, F. Rodrı, M. J. Biggs, *Carbon N. Y.* **2015**, *85*, 147–158.

[61] Y. Eom, S. M. Son, Y. E. Kim, J. E. Lee, S. H. Hwang, H. G. Chae, *Carbon N. Y.* **2019**, *150*, 142–152.

[62] S. Zhang, Q. Liu, H. Zhang, R. Ma, K. Li, Y. Wu, B. J. Teppen, *Carbon N. Y.* **2020**, *157*, 714–723.

[63] J. C. Lascovich, R. Giorgi, S. Scaglione, *Appl. Surf. Sci.* **1991**, *47*, 17–21.

[64] A. Fujimoto, Y. Yamada, M. Koinuma, S. Sato, *Anal. Chem.* **2016**, *88*, 6110–6114.

[65] M. Sevilla, A. B. Fuertes, *Mater. Chem. Phys.* **2009**, *113*, 208–214.

[66] M. T. Johnson, K. T. Faber, *J. Mater. Res.* **2011**, *26*, 18–25.

[67] X. Zhu, J. Ye, Y. Lu, X. Jia, *ACS Sustain. Chem. Eng.* **2019**, *7*, 11241–11249.

[68] H. S. Oktaviano, K. Waki, *J. Electrochem. Soc.* **2016**, *163*, A442–A446.

[69] Y. Li, Y.-F. Du, G.-H. Sun, J.-Y. Cheng, G. Song, M.-X. Song, F.-Y. Su, F. Yang, L.-J. Xie, C.-M. Chen, **2021**, DOI 10.1002/eom2.12091.

[70] S. Alvin, H. S. Cahyadi, J. Hwang, W. Chang, S. K. Kwak, J. Kim, *Adv. Energy Mater.* **2020**, *10*, 1–16.

[71] L. Xie, C. Tang, Z. Bi, M. Song, Y. Fan, C. Yan, X. Li, F. Su, Q. Zhang, C. Chen, *Adv. Energy Mater.* **2021**, *11*, 1–22.

[72] Y. Huang, Y. Wang, P. Bai, Y. Xu, *ACS Appl. Mater. Interfaces* **2021**, *13*, 38441–38449.

[73] K. Yu, Z. Zhang, J. Liang, C. Liang, *Diam. Relat. Mater.* **2021**, *119*, 108553: 1–11.

[74] Y. Dou, X. Liu, K. Yu, X. Wang, W. Liu, J. Liang, C. Liang, *Diam. Relat. Mater.* **2019**, *98*, 107514: 1–9.

[75] V. Etacheri, C. Wang, M. J. O'Connell, C. K. Chan, V. G. Pol, *J. Mater. Chem. A* **2015**, *3*, 9861–9868.

[76] M. Weiss, R. Ruess, J. Kasnatscheew, Y. Levartovsky, N. R. Levy, P. Minnmann, L. Stolz, T. Waldmann, M. Wohlfahrt-Mehrens, D. Aurbach, M. Winter, Y. Ein-Eli, J. Janek, *Adv. Energy Mater.* **2021**, *11*, 2101126: 1–37.

[77] T. H. Park, J. S. Yeo, M. H. Seo, J. Miyawaki, I. Mochida, S. H. Yoon, *Electrochim. Acta* **2013**, *93*, 236–240.

[78] X. Rao, Y. Lou, J. Chen, H. Lu, B. Cheng, W. Wang, H. Fang, H. Li, S. Zhong, *Front. Energy Res.* **2020**, *8*, 1–9.

Chapter 3

Highly graphitized porous carbon from coconut waste developed by Ni-KOH reaction for lithium-ion battery anodes

3.1. Introduction

As discussed in Chapter 2, coconut coir, a waste product of the coconut industry in Indonesia, is an abundant and underutilized carbon source that has the potential to be used as an anode material. However, it is still necessary to improve the properties of the resulting carbon material to enhance battery performance. In this chapter, we aim to address this need by focusing on developing porous graphitic carbon (PGC) materials derived from renewable coconut coir. To generate a carbon material with the combined features of high graphitic structure and large surface area in order to boost LIB capacity, a simple and low-energy-consumption process is required. But it remains challenging because both features have a contradicting relationship.

Hence, in this chapter, coconut coir waste was further explored by converting it into porous graphitic carbon (PGC) through the combination of Ni-based catalysts and KOH in a one-pot system. This innovative synthesis approach allows for a synergistic effect resulting from the reaction of the two agents with carbon, resulting in several advantages compared to the Ni-catalyst-only method employed in the Chapter 2. Firstly, the one-pot method generates carbon products with a higher degree of graphitization, indicating a more ordered and crystalline carbon structure. Additionally, the one-pot synthesis reduces the initial formation temperature required for the development of graphitic structures, indicating improved efficiency and faster kinetics. By investigating the effects of pyrolysis temperatures up to 1200 °C, we gained insights into the competitive relationship between pore structure and graphitic structure development. Through careful optimization, we identified the optimal

pyrolysis temperature for producing PGC materials with enhanced graphitization and a large surface area, leading to a significant increase in battery capacity. In summary, by utilizing this renewable carbon source and employing the effective one-pot synthesis process, we not only address environmental challenges associated with fossil-based graphite but also pave the way for the development of more sustainable lithium-ion batteries.

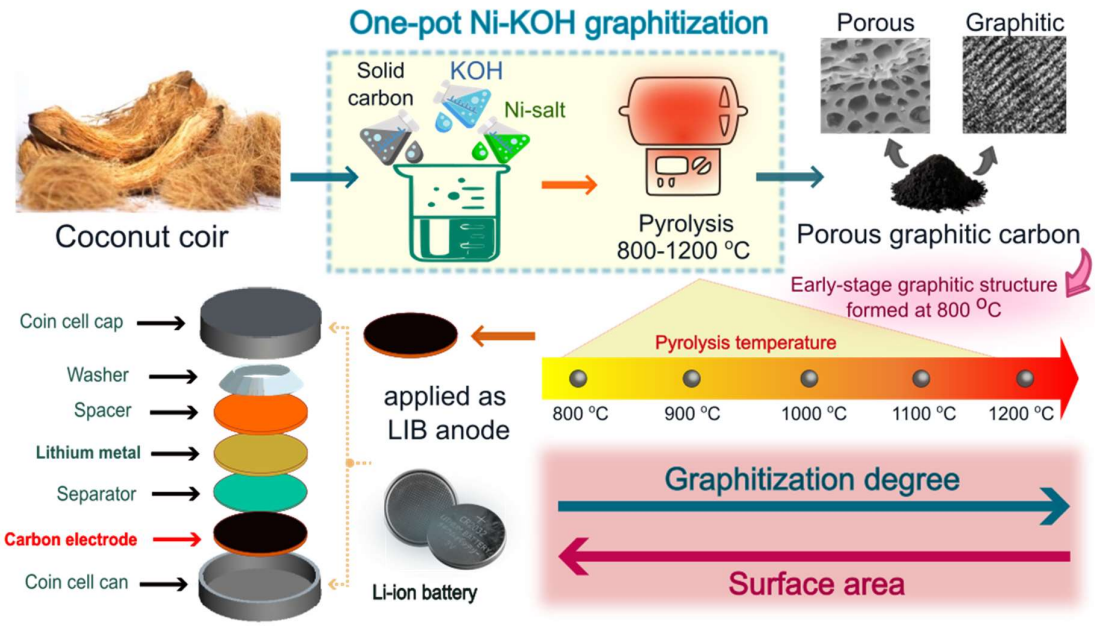

Scheme 3-1. Graphical abstract of Chapter 3

3.2. Experimental Section

3.2.1. Materials

All reagents were used as received. Coconut coir obtained from local market in Indonesia was used in this work as carbon source. Nickel (II) chloride hexahydrate ($NiCl_2 \cdot 6H_2O$), potassium hydroxide (KOH), and hydrochloric acid (HCl, 37%) were purchased from Merck. The water used throughout the experiment was purified using an Evoqua LaboStar PRO TWF UV ultra-pure water system.

3.2.2. Synthesis of porous graphitic carbon from coconut coir

Raw coconut coir (20 g) was initially carbonized in an N_2 gas atmosphere at 500 °C for an hour. The carbonized sample (with a yield of 30.73 wt.%) was subsequently ground into a fine powder with a particle size of roughly 74 μm. Then 6.15 g of carbon powder was immersed into a mixture solution of $NiCl_2.6H_2O$ and KOH, with a 1:1.2:1 wt% ratio of the mixture. The mixture was evaporated at 60 °C, followed by drying overnight at 80 °C. The dried mixture was then pyrolyzed at various temperatures from 600 to 1200 °C in a tubular furnace under an N_2 gas atmosphere (flow rate of 200 mL/min) at a heating rate of 5 °C/min for 3 hours and then cooled to room temperature automatically. The obtained carbon sample (a yield of 44.88 wt.%) was soaked overnight in 2 M HCl solution to remove the Ni and K species, then repeatedly washed with deionized water and dried at 80 °C. The porous graphitic carbon products are denoted as t-ANi-KOH (t represents the pyrolysis temperature, ranging from 600 to 1200 °C). The synthesis routes for obtaining PGC are depicted schematically in **Scheme 3-2**.

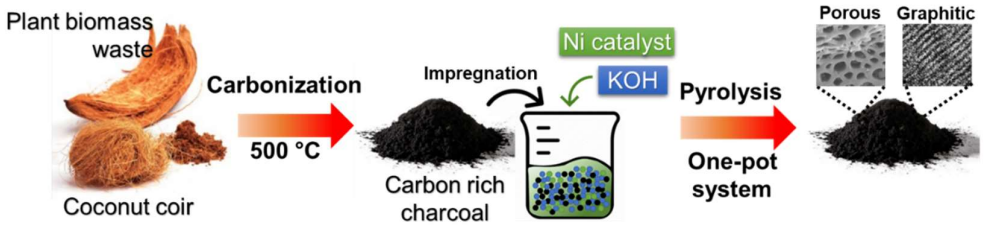

Scheme 3-2. Schematic illustration of porous graphitic carbon synthesis.

3.2.3. Preparation of analogous samples for comparison

For comparison, three types of samples were prepared through different methods as follows:

(i) The 1200-CC sample was prepared using a pyrolysis method: the synthesis procedure was identical to 1200-ANi-KOH, except that no Ni-based catalyst and KOH were added to the system. The obtained carbon sample (yield of ±65.35 wt %) was denoted as 1200-CC.

(ii) The 1200-KOH sample was prepared using a KOH chemical activation method: the synthesis and washing procedure were identical to 1200-ANi-KOH, except that no Ni-based catalyst was added to the system. The obtained carbon sample (yield of ±26.35 wt %) was denoted as 1200-KOH.

(iii) The 1200-ANi sample was prepared using a Ni-based catalytic graphitization method: the synthesis and washing procedure were identical to 1200-ANi-KOH, except that no KOH was added to the system. The obtained carbon sample (yield of ±52.55wt %) was denoted as 1200-ANi.

3.2.4. Material characterization method

Rigaku SmartLab X-ray Diffractometer with Cu-Kα radiation (λ = 1.54059 Å) over the scanning angle (2θ) range of 10–90° at 40 kV and 30 mA was used to generate X-ray diffraction (XRD) patterns for all samples. The carbon interlayer spacing (d_{002}) was determined by the Bragg equation of $d_{002} = \lambda/2\sin\theta_{002}$, where λ is the wavelength of the X-ray radiation and θ_{002} is the (002) reflection angle [1]. Horiba Modular Raman iHR320 was used to record Raman spectra with a laser wavelength of 532 nm and a scanning range of 1,000 to 2,850 cm^{-1} in 10 s. The Raman spectra were analyzed by peak deconvolution using the curve-fitting method for char published by Smith et al. [2]. The morphologies of the samples were investigated using scanning electron microscope (SEM, HITACHI SU3500) and transmission electron microscopy (TEM, JEM 2100, operated at 200 kV accelerating voltage). A JEOL JPS-9010MC X-ray photo-electron spectroscopy (XPS) instrument with monochromatic Al Kα-radiation was used to record XPS spectra. The peaks were fitted using the CasaXPS version 2.3.25 software package (Casa Software, Ltd.). The porous structure for all samples were analyzed using N_2 adsorption-desorption measurements obtained using a TriStar II 3020 2.00 (Micromeritics, USA) instrument operated at 77 K. The Brunauer–Emmett–Teller (BET) and Density Functional

Theory (DFT) methods were used to determine the surface area and pore size distribution, respectively.

3.2.5. Electrochemical measurement

All the electrochemical measurements were carried out using CR2032 coin cells. The working electrode was prepared by mixing 80 wt.% of the carbon samples (t-ANi-KOH) as active material, 10 wt.% of polyvinylidene fluoride (PVDF) binder, and 10 wt.% of conductive agent (Super P) in dimethylacetamide (DMAc), then casting the mixture on a copper foil using a standard doctor blade technique at a thickness of 150 μm. The mass loading of the active material was 2-7 mg/cm^2. Coin cells were assembled in half-cell configuration using a lithium metal electrode as a reference and counter electrode, polyethylene separator, and a standard electrolyte lithium hexafluorophosphate (LiFP6) 1 M in ethylene carbonate and dimethyl carbonate with the molar ratio of 1:1 at room temperature. The cell was assembled in an argon-filled glove box. Galvanostatic charge/discharge (CD) and cyclic voltammetry (CV) measurements of the samples were performed by using Battery Testing System (Neware, BTS-5V10mA) and Automatic Battery Cycler (Wonatech, WBCS3000). The CD tests was carried out with C-rate variation of 0.05C, 0.1C, 0.2C, 0.5C, and 1C at potentials range from 0.01 to 3.0 V (vs. Li/Li+). The CV test was conducted between 0.01 and 2.5 V at a scan rate of 0.1 mV/s.

3.3. Results and Discussion

3.3.1. High graphitic carbon derived from coconut coir waste by promoting potassium hydroxide in the catalytic graphitization process

Structural characteristic analysis

The structural information of all carbon samples obtained and commercial graphite for comparison was analyzed using XRD, Raman, and TEM. As shown in **Figure 3-1**(a−c), the

XRD pattern of the 1200-CC sample displays two broad peaks at 2θ values of 23 and 43°, respectively, indicating a predominantly amorphous phase. This result demonstrates that the pyrolysis process at 1200 °C cannot convert the structure of coconut coir carbon into graphitic carbon. Then, the KOH-activated sample revealed a slight change of (002) peak. The (002) peak of 1200-KOH sample appears sharper and moves to a larger 2θ value of 25.75° (**Figure 3-1**b), indicating a more ordered structure compared to 1200-CC. The interlayer spacing (d_{002}) also decreases from 0.38 to 0.3457 nm, as shown in **Figure 3-1**c, further indicating that the structure of 1200-KOH becomes better than 1200-CC. In the meantime, the Ni-based catalytic graphitized sample (1200-ANi) exhibits a much sharper and stronger (002) peak. The (002) peak also shifts to an even larger 2θ position (26.44°), followed by a decrease in the (d_{002}) interlayer spacing to 0.3369 nm compared to 1200-KOH and closer to the (002) peak value of the commercial graphite. This result reveals that Ni-based catalytic graphitization has converted the amorphous structure of coconut coir carbon into graphitic as reported in our previous work[3]. Furthermore, a combination of KOH chemical activation and Ni-based catalytic graphitization processes carried out on the carbon led to the further structural change. 1200-ANi-KOH displays a higher intensity of the (002) peak at the 2θ position of 26.42° and a slight increase in the interlayer spacing (d_{002}= 0.3367 nm) compared to 1200-ANi. These findings suggest that the combination process of KOH chemical activation and Ni-based catalytic graphitization conducted in a one-pot system exerted a positive effect on improving the graphitic structure of carbon material when compared to the Ni-based catalytic graphitization process solely.

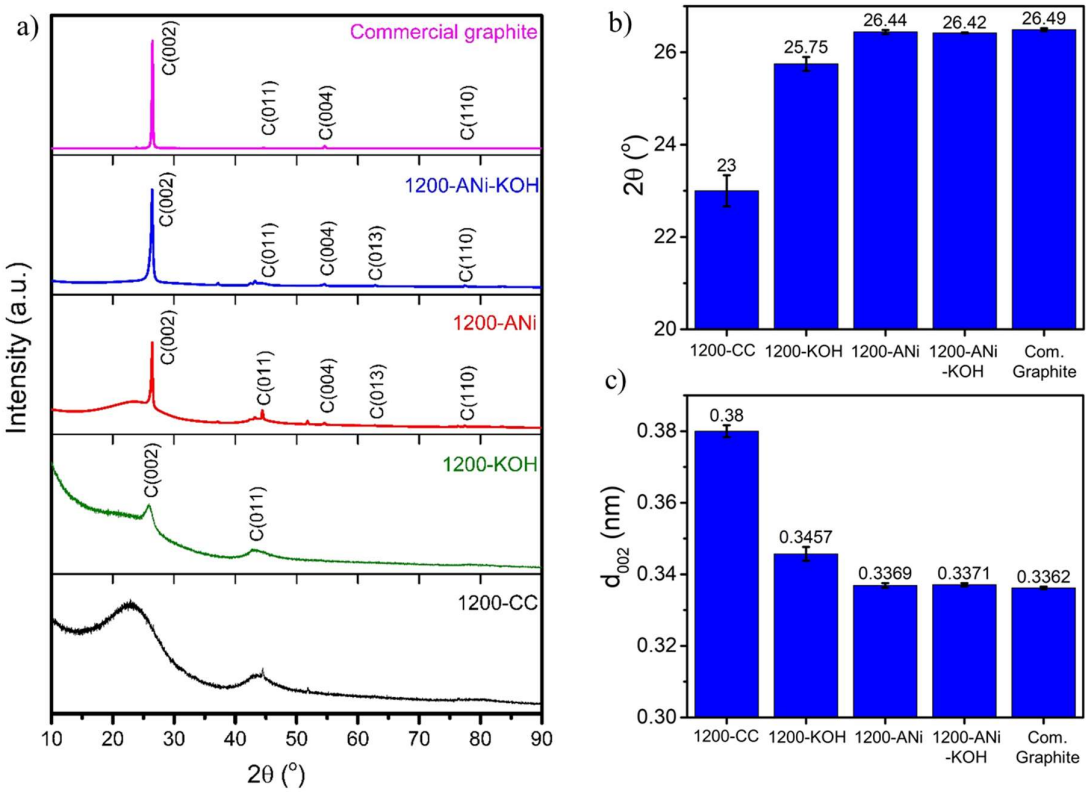

Error! Reference source not found.. (a) XRD patterns, (b) (002) peak position, and (c) interlayer spacing (d_{002}) of all carbon materials obtained from each fabrication method (1200-CC, 1200-KOH, 1200-ANi, and 1200-ANi-KOH).

The structural ordering of all carbon samples was further verified through Raman spectroscopy, and the spectra are shown in **Figure 3-2**a. The spectrum of sample 1200-CC can be seen to consist of two broad overlapping peaks at around 1340 cm^{-1} (D-band) and 1584 cm^{-1} (G-band), showing the presence of the amorphous carbon structure. The D-band is associated with defects or disorder in the structure due to the existence of sp^3-hybridized carbon, while the G-band is assigned to the stretching vibrations of sp^2-hybridized bonds in the hexagonal lattice of graphitic carbon[4,5]. On the other hand, the spectral profile of 1200-KOH, 1200-ANi, and 1200-ANi-KOH appears to be slightly different. They exhibited three peaks: D-band, G-band, and one additional peak at around 2694 cm^{-1} that was assigned to the 2D-band, which is similar to commercial graphite. The appearance of a 2D-band is characteristic of graphite[4], related to

the existence of the graphene sheet stacking order along the c-axis[6,7]. It reveals that the graphitic structure is present in these three samples, agreeing with the XRD analysis. Furthermore, the structural order of all samples was further evaluated through quantitative analysis based on the integral area ratio of the G-band and D band (IG/ID) and the full width at half maximum (FWHM) of G-band. The spectra of all samples from 1100 to 1800 cm^{-1} were first deconvoluted using the Gaussian−Lorentzian curve fitting procedure, as shown in **Figure 3-2**(b−f), and the analytical results are shown in **Figure 3-2**g and **Figure 3-2**h. As can be seen, the Raman spectrum of carbon materials was decomposed into five components: the TPA-band near 1240 cm^{-1} associated with transpolyacetylene-like structures[8], the D-band, the A-band near 1490 cm^{-1} associated with amorphous structures[2], the G-band, and the D'-band, which is a defect-induced feature caused by intravalley double resonance scattering[8]. The calculated IG/ID (**Figure 3-2**g) of the 1200-KOH appears to be slightly higher than that of the 1200-CC, followed by a significant increase in those of the 1200-ANi and 1200-ANi-KOH samples. **Figure 3-2**h shows that 1200-ANi and 1200-ANi-KOH exhibit small G-band FWHM values of 25.64 and 25.17 cm^{-1}, respectively, which are in the range of values for materials with a well-ordered graphitic structure (23.8−30.3 cm^{-1})[9]. Additionally, the sample obtained through a combination of KOH chemical activation and Ni-based catalytic graphitization (1200-ANi-KOH) exhibits the highest IG/ID ratio and smallest D-band FWHM value, indicating the highest degree of graphitization in comparison to all other samples, consistent with the XRD results.

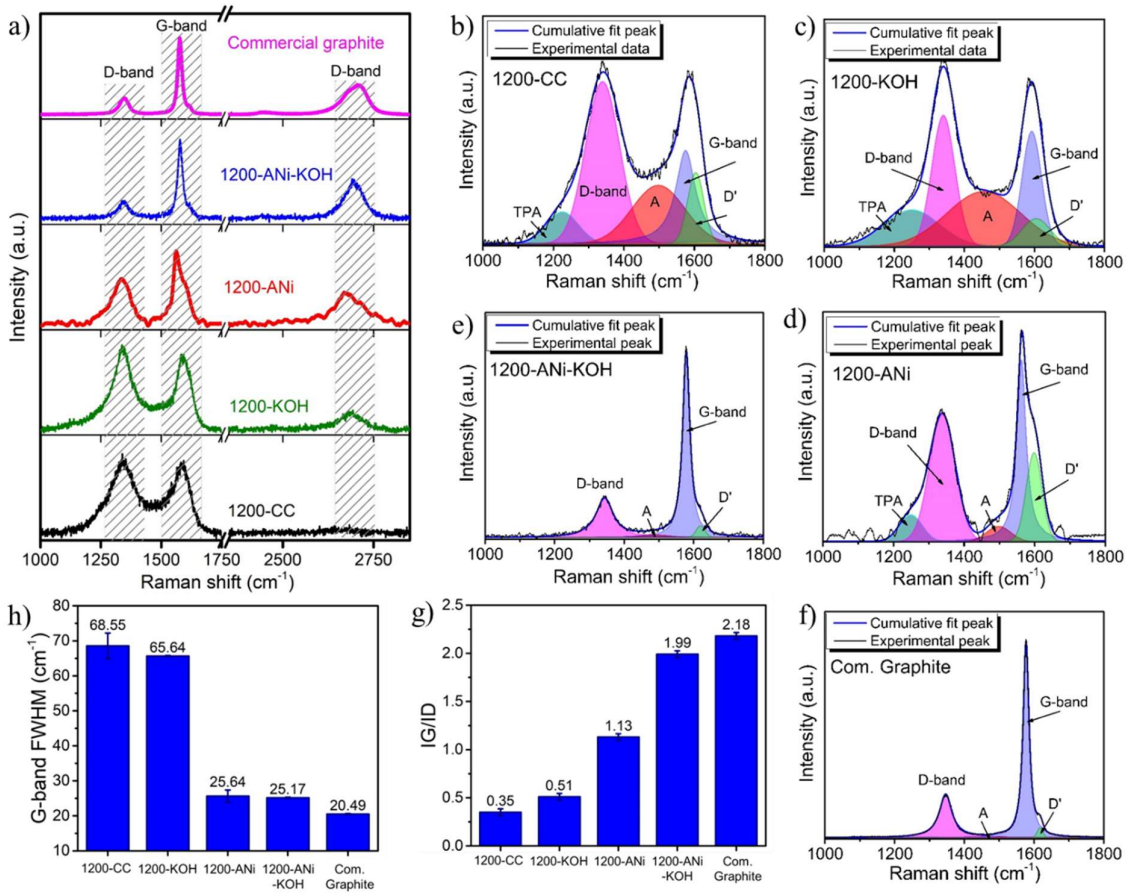

Figure 3-2. (a) Raman spectra of all samples. Deconvolution of Raman spectra for (b) 1200-CC, (c) 1200-KOH, (d) 1200-ANi, (e) 1200-ANiKOH), and (f) commercial graphite. Raman structural parameters according to the Raman fitting analysis: (g) IG/ID ratios (area-based) and (h) FWHM of G-band.

The structure produced by each fabrication process was also confirmed using X-ray photoelectron spectroscopy (XPS) by calculating the C=C(sp^2)/C−C(sp^3) ratio. The C=C(sp^2) represents sp^2-hybridized carbon atoms that make up the graphene and graphite structure, whereas C−C(sp^3) is a sp^3-hybridized carbon atom present in the diamond and diamondlike carbon[10]. The obtained survey spectra as shown in **Figure 3-3**a show mainly the presence of C 1s and O 1s photoemission peaks. The C=C/C−C ratio all samples can be calculated through the XPS fitting analysis of C 1s peak. Using the Gaussian−Lorentzian line shape and Shirley background type as provided by Smith et al.[11], the C 1s spectrum of all samples was fitted to

seven components: 3C−C peaks, three oxygenated peaks, and π−π* transition peak[11,12], as indicated in **Figure 3-3**(b−e). The C−C peaks corresponded to cyclopentane ring atoms within the cluster (C−C low), sp^2-hybridized carbon (C=C bonds), and sp^3-hybridized carbon (C−C) in the disordered phase. The oxygenated peaks were attributed to phenol or hydroxyl (C−O) groups, carbonyl (C=O) groups, and C in carboxyl and ester (COO) groups. Then, the area fractions for each peak calculated by deconvolution of C 1s peak are summarized in **Figure 3-3**f. It was confirmed that the combined process of KOH chemical activation and Ni-based catalytic graphitization produced carbon material with the highest C=C/C−C ratio, suggesting the highest amount of graphitic carbon, when compared to the KOH chemical activation process only as well as the Ni-based catalytic graphitization process solely.

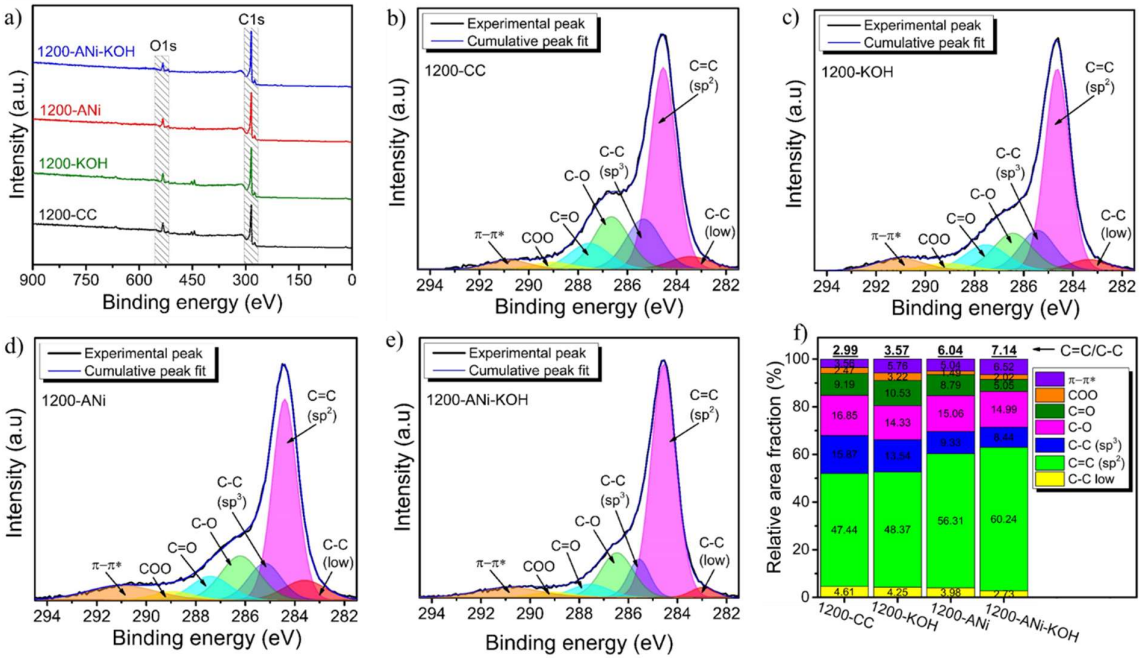

Figure 3-3. (a) XPS wide scan spectra. Deconvoluted XPS C 1s peak for (b) 1200-CC, (c) 1200-KOH, (d) 1200-ANi, and (e) 1200-ANi-KOH. (f) Relative area fractions of deconvoluted C 1s peak and C=C/C−C ratios of all samples.

TEM in conjunction with selected area electron diffraction pattern (SAED) was used to conduct in-depth observations on the structural ordering of all carbon samples (**Figure 3-4**(a−l)). In conformity with the findings of XRD, Raman, and XPS examination, the TEM image of 1200-CC (**Figure 3-4**(a-b)) revealed disordered microstructures or randomly orientated structure, which is characteristic of amorphous carbonaceous material. The appearance of a diffuse ring in the SAED pattern, as shown in **Figure 3-4**c, also confirmed the amorphous phase in the 1200-CC sample. On the other hand, the presence of graphitic structures in the 1200-KOH, 1200-ANi, and 1200-ANi-KOH samples as described on XRD and Raman analysis is clearly visible on the TEM images (**Figure 3-4**(d−l)). Graphitic regions are seen as ribbon-like structures in the low magnification TEM images of these three samples (**Figure 3-4**d, **Figure 3-4**g, **Figure 3-4**j). The HRTEM observations focused on these ribbonlike structures revealed well-defined lattice fringes in all three samples (**Figure 3-4**e, **Figure 3-4**h, **Figure 3-4**k). It can be seen that the graphitic regions in these three samples are composed of multilayer graphene sheets separated by interlayer distances of ±0.3457, ±0.3369, and ±0.3371 nm (from XRD results) for the 1200-KOH, 1200-ANi, and 1200-ANi-KOH, respectively. However, compared to the other two samples, the number of graphene layers in the 1200-KOH sample appeared to be less and uneven, indicating a lower degree of graphitization. Hence, the spot patterns observed in the SAED images (**Figure 3-4**f, **Figure 3-4**i, **Figure 3-4**l) for these three samples confirmed the existence of crystalline ordering or graphitic structures.

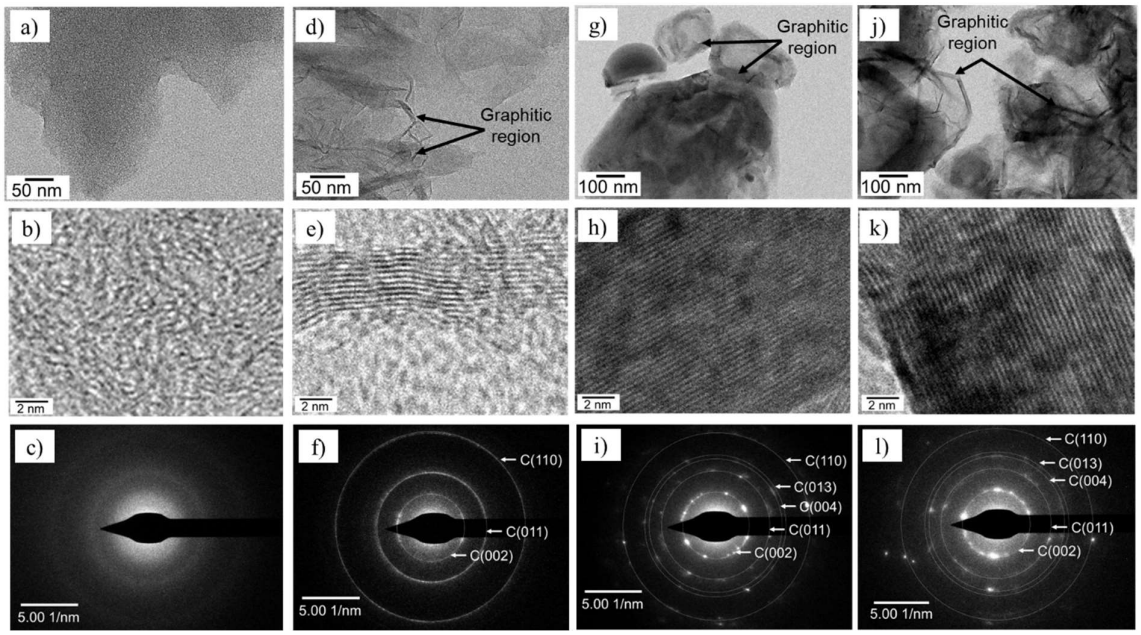

Figure 3-4. Low magnification TEM, HRTEM, and SAED images of (a−c) 1200-CC, (d−f) 1200-KOH, (g−i) 1200-ANi, and (j−l) 1200-ANi-KOH.

Process mechanism

The structure formed in all the carbon samples is strongly influenced by the mechanisms that occur during each fabrication method. When amorphous carbon from coconut coir was pyrolyzed up to 1200 °C under inert atmosphere, there was no significant structural change. During pyrolysis with increasing temperature to above 2500 °C, there is a typical stage that occurs causing atomic rearrangements[13,14], which are as follows: (I) high content of amorphous carbon and defects caused by dangling bonds on the aromatic rings; (II) amorphous carbon transforms to a more ordered structure by increasing aromatic structure and reducing defects; (III) sheets of aromatic structure grow turbostratically; and (IV) the aromatic structure sheet stack more ordered, graphitic carbon. The amorphous structure still dominates in the carbon sample of 1200-CC. It can be due to the stabilization of the defect sites such as dangling bonds by the high stability of aromatic network surrounding them[15].

Meanwhile, in the solely KOH chemical activation process of coconut coir carbon, KOH and carbon can react with the following probable reactions during the high temperature treatment:[16,17]

$$2C + 6KOH \rightarrow 3H_2 + 2K + 2K_2CO_3 \quad (3\text{-}1)$$

$$K_2CO_3 \rightarrow K_2O + CO_2 \quad (3\text{-}2)$$

$$K_2O + C \rightarrow 2K + CO \quad (3\text{-}3)$$

$$CO_2 + C \rightarrow 2CO \quad (3\text{-}4)$$

A certain amount of K compounds and gasses generated act as an activator and corrode the carbon skeleton. When the temperature exceeds 800 °C, the K compounds are further reduced and sublimated by carbon, producing K metal. The K metal then intercalates into the carbon layer, causing the carbon layer to expand and rearrange. This process leads to pore structure formation through the redox reactions between various potassium compounds with carbon (Eq. 3-1, Eq. 3-3, and Eq. 3-4), the gasification of carbon (Eq. 3-1, Eq. 3-2, and Eq. 3-4), and the intercalation effect of K into the carbon skeleton (Eq. (3-1) to Eq. 3-3). Additionally, the abovementioned characterization demonstrates that the samples subjected to the KOH chemical activation process at 1200 °C (1200-KOH) detected a little amount of an ordered carbon structure. The formation of an ordered carbon structure during this process could be attributed to the interaction between K metal and carbon[17], which causes internal heating, and localized graphitization formed subsequently[6,18].

When coconut coir carbon was treated with only the Ni-based catalytic graphitization process, the amorphous structure of the product (1200-ANi) was converted into a more ordered graphitic structure than the previous method. The graphitic structure was formed at a relatively lower temperature than using the pyrolysis process (≥2500 °C) as a catalytic graphitization effect involving the reaction of Ni nanoparticles with amorphous carbon. In general, the process occurs as follows: Ni salt initially decomposed into nickel oxide (NiO), which then undergoes

reduction to Ni nanoparticles by amorphous carbon[19]. Then, the Ni nanoparticles were diffused and moved into the amorphous carbon matrix because of the random diffusion effect and/or C−Ni interaction[20]. At a particular temperature, the high solubility of carbon in Ni allows amorphous carbon to dissolve and diffuse easily in Ni[21]. Graphitic carbon precipitation forms at the C−Ni interface when the Ni−C system approaches super saturation, as a result of the difference in free energy between amorphous carbon and graphitic carbon[22,23].

Furthermore, as previously stated, the combination process of KOH chemical activation and Ni-based catalytic graphitization carried out on coconut coir carbon in a one-pot system exposes the highest proportion of graphitic structure. The greatest graphitic structure of 1200-ANi-KOH can be attributed to the synergistic effect of the interaction of K and Ni metal with amorphous carbon, leading to internal heating and catalytic graphitization. In particular, as discussed in the preceding section, KOH and carbon react to form porous carbon and K metal[16]. According to the TEM analysis result (**Figure 3-4**e), during a high temperature process at 1200 °C, K metal plays two roles: it can graphitize the carbon locally due to internal heating around the K metal[17], and it corrodes the carbon skeleton, resulting in a pore structure on the carbon[16]. Simultaneously, a catalytic graphitization process of amorphous carbon using Ni nanoparticles occurs. These two interactions of K and Ni metals with carbon synergize to form a larger area of the graphitic structure (**Scheme 3-3**).

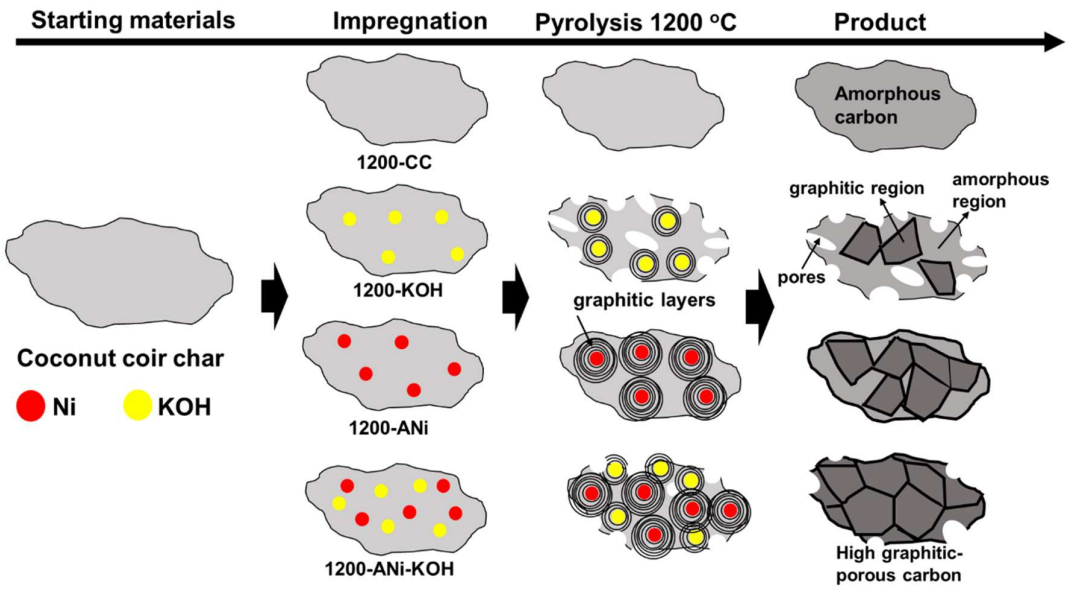

Scheme 3-3. Schematic illustration of the mechanism for the synthesis processes of carbon materials from coconut coir.

Textural properties analysis

The carbon material fabrication method mentioned above also affects the pore structure observed using the BET method. Shown in **Figure 3-5**(a−d) are nitrogen adsorption−desorption isotherms of all samples. On the isotherm of each sample, a hysteresis loop appears, displaying Type IV and a combination of Type I and IV isotherms, according to the IUPAC classification for 1200-ANi-KOH and the other samples, respectively. This suggests that the 1200-ANi-KOH sample contains a considerable number of mesopores, whereas the other three samples have a micro-/mesoporous texture[24]. This was verified by the pore size distribution curves (**Figure 3-5**(e-f)) derived from the nitrogen sorption isotherms. The 1200-CC sample exhibited the lowest surface area of 9.4 m^2/g. Its micro-/mesopores were generated by degradation of the lignocellulose compounds during the pyrolysis process, releasing volatile and gaseous byproducts. In contrast to structural order, the 1200-KOH sample displays the highest BET surface area (1314.52 m^2/g) and micropores compared to other samples. The activation process

using KOH has a significant effect on generating micropores and small mesopores to carbon material through the mechanism described above[16]. The catalytic graphitization process on sample 1200-ANi tends to produce a material with a surface area of 337.45 m^2/g. The existence of micro-/mesopores in the 1200-ANi originates from the etching reaction between the Ni and carbon during the catalytic graphitization, as well as Ni removal process. However, when the KOH chemical activation and the Ni-based catalytic graphitization procedure were carried out simultaneously, the surface area decreased to 162.31 m^2/g. Micropores were almost undetectable in the 1200-ANi-KOH sample, but the presence of mesopores was dominant compared to other samples. This phenomenon is thought to be caused by the graphitization and rearrangement of the carbon structure, which removes the nanoporous structure, thereby reducing the surface area. The interaction between Ni and carbon, which destroys the micropores formed due to the activation effect of KOH, is also thought to contribute to this reduction in surface area.

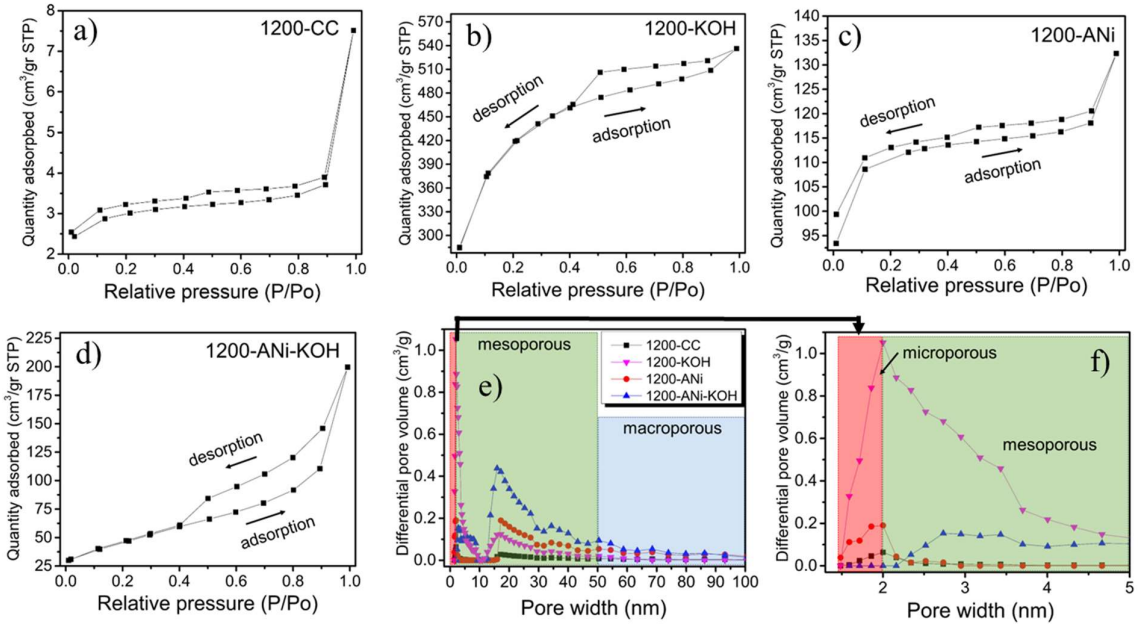

Figure 3-5. Nitrogen adsorption−desorption isotherms of (a) 1200-CC, (b) 1200-KOH, (c) 1200-ANi, (d) 1200-ANi-KOH, and (e-f) the BJH pore size distribution.

3.3.2. Pyrolysis temperature dependence of porous graphitic carbon from coconut coir developed by Ni-KOH reaction

Structural characteristic analysis

The structural transformations of Ni-KOH treated coconut coir carbon during the catalytic graphitization process at temperatures ranging from 600 to 1200 °C were investigated using XRD, Raman spectroscopy, XPS, and TEM analysis. The XRD pattern in **Figure 3-6**a depicts that two samples pyrolyzed at temperatures below 800 °C (600-ANi-KOH and 700-ANi-KOH) displayed the dominating amorphous phase with two broad peaks at ~23° and ~43°. Then, when the temperature rises over 800 to 1200 °C, the broad peaks at ~23° and ~43° decrease, while the (002) peak becomes sharper and stronger, indicating that the amorphous structure gradually transforms into a graphitic structure, with a portion of it growing dominant. The location of the (002) peak also shifted toward higher 2θ value, leading a decrease in the interlayer distance (d_{002}), as shown in **Figure 3-6**b, and approaching the (002) peak value of the commercial graphite powder (0.3362 nm)[25], suggesting the development of a more ordered graphitic structure. These finding reveals that the pyrolysis temperature in the KOH and Ni catalyst treatment process conducted in a one-pot system on coconut coir carbon has a positive effect on the structural transformation from amorphous to graphitic. In addition, this process was able to significantly reduce the initial temperature of graphitic nanostructure formation on coconut coir carbon from 1200 °C to 800 °C as compared to the Ni-based catalytic graphitization process solely as we previously reported in Chapter 2, through a mechanism that will be described in detail in the next section.

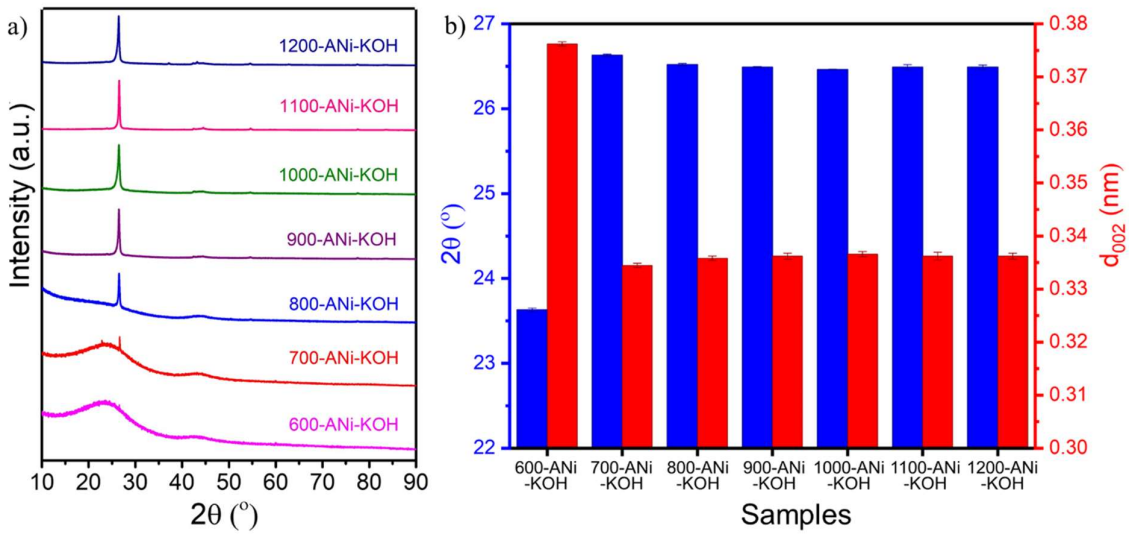

Figure 3-6. (a) XRD patterns and (b) (002) peak position, and interlayer spacing (d_{002}) of all carbon materials with increasing pyrolysis temperature.

The spectra of Raman spectroscopy shown in **Figure 3-7**a were utilized to confirm the XRD findings and to determine the degree of graphitization of all samples. The presence of the dominant amorphous carbon structure in samples 600-ANi-KOH and 700-ANi-KOH are confirmed by the appearance of two broad overlapping peaks at approximately 1346 cm^{-1} (D-band) and 1587 cm^{-1} (G-band). The D-band is related to structural defects or disorder induced by the presence of sp^3-hybridized carbon, and G-band is associated with the stretching vibrations of sp^2-hybridized bonds in graphitic carbon's hexagonal lattice[4]. As the pyrolysis temperature increases over 800 to 1200 °C, the G bands grow significantly sharper, with 2D bands appear around 2681-2691 cm^{-1}, indicating the presence of the graphene sheet stacking order along the c-axis. These confirmed the XRD findings by revealing that the graphite structure was formed, and its fraction became dominant at temperatures ranging from 800 °C during pyrolysis.

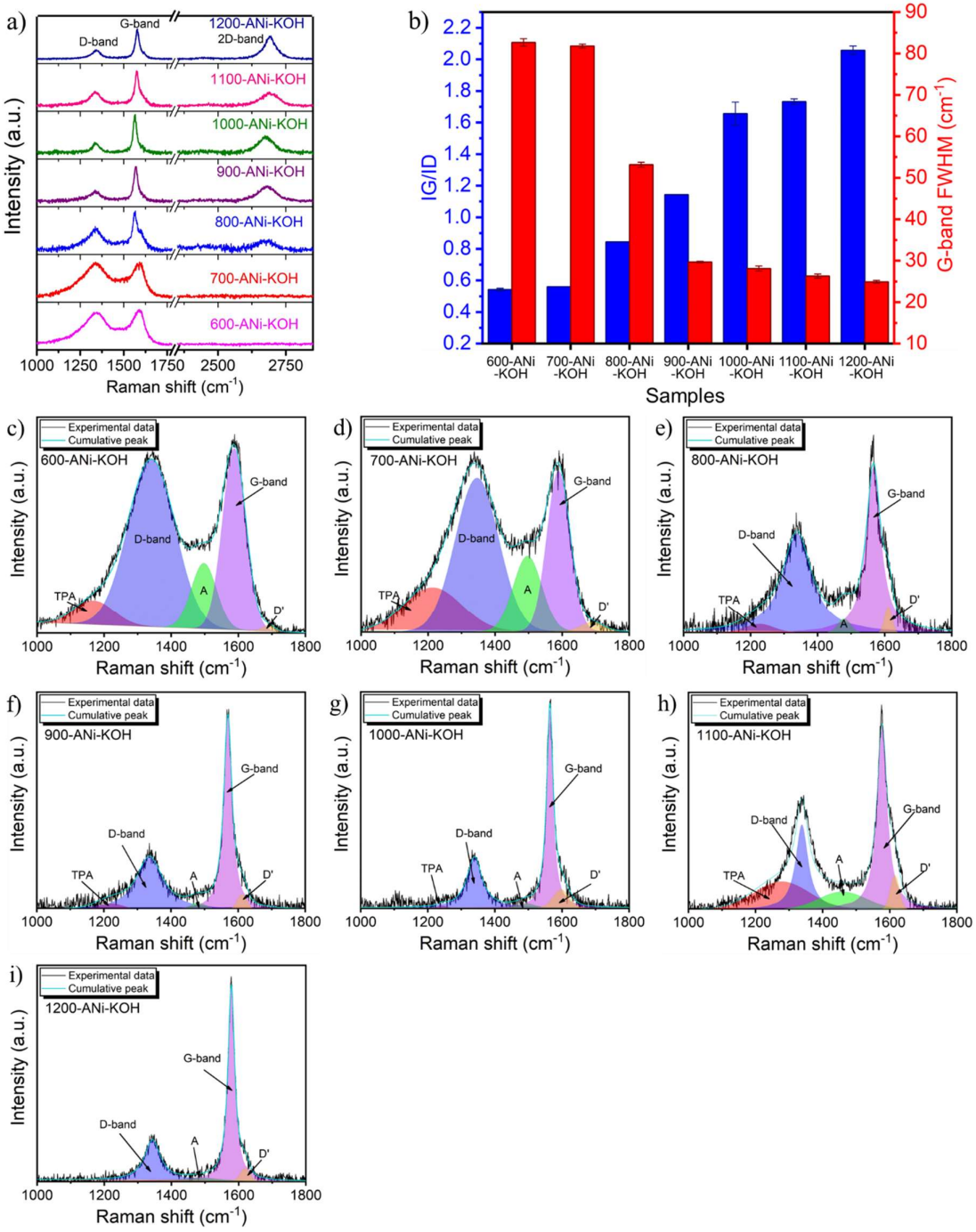

Figure 3-7. (a) Raman spectra of all carbon materials with increasing pyrolysis temperature, (b) Raman structural parameters according to the Raman fitting analysis: IG/ID ratios (area-based) and FWHM of G-band. Deconvolution of Raman spectra for (c) 600-ANi-KOH, (d) 700-ANi-KOH (e) 800-ANi-KOH, (f) 900-ANi, (g) 1000-ANi-KOH, (h) 1100-ANi-KOH, (i) 1200-ANi-KOH

Quantitative analysis based on the integral area ratio of the G-band to the D-band (IG/ID) and the full width at half maximum of the G-band (G-FWHM) was also performed to further analyze the structural order of all samples. Initially, using the Gaussian-Lorentzian curve fitting method, the spectra of all samples were deconvoluted into five components (shown in **Figure 3-7**(c-i)): the D and G bands; the TPA-band located to the left of the D-band which is related to transpolyacetylene-like structures; the A-band associated with amorphous structures, which contributes to the intensity between D and G band; and the D′-band located to the right of the G band, which is a defect-induced feature caused by intravalley double resonance scattering[5,8,26]. Then, as the pyrolysis temperature rises from 600 to 1200 °C, the calculated IG/ID ratio of the sample shown in **Figure 3-7**b gradually goes from 0.54 to 2.06, indicating a gradual increase in the degree of graphitization. On the other hand, as temperature goes up, the G-FWHM value decreases, indicating an improvement in the in-plane uniformity of polycrystalline graphite due to the removal of edge and point defects, resulting in a more ordered graphitic structure[27]. Moreover, samples pyrolyzed at temperatures between 900 to 1200 °C (900-ANi-KOH to 1200-ANi-KOH) appear to have G-FWHM values in the range of 23.8−30.3 cm^{-1}, which is typical for materials with a well-ordered graphitic structure[9]. These results demonstrate that the synthesis process using KOH and Ni-based catalytic graphitization in a single-pot system is able to produce highly structured graphitic materials at lower temperatures, than those required by the Ni-based catalytic graphitization process alone (Chapter 2).

XPS was also used to validate the structure of the carbon sample by determining its surface elemental composition, as reported in earlier studies[10,28,29]. In **Figure 3-8**a, the C1s and O1s photoemission peaks predominate in the XPS wide scan spectra of all samples with the binding energy from 0 to 900 eV, suggesting the carbon material primarily consists of carbon and oxygen components. The C=C/C-C carbon ratio was then analyzed quantitatively

by fitting the C1s peak using the CasaXPS software. As demonstrated by Eom et al.[27] and Smith et al.[11], the C1s spectrum was deconvoluted into the following peaks: C-C low of cyclopentane ring atoms within cluster, C=C of sp^2-hybridised carbon in aromatic, C-C of sp^3 bounded carbon, C–O of phenol or hydroxyl groups, C=O of carbonyl groups, COO of carboxyl and ester groups, and a $\pi-\pi^*$ transition peak, as depicted in **Figure 3-8**(c-i). The area-fraction calculation under each peak is summarized in **Figure 3-8**b. The C=C/C-C ratio increases as the pyrolysis temperature rises to 1200 °C, indicating an increase in the amount of amorphous carbon transformed into graphitic carbon at higher temperatures. These findings are consistent with XRD and Raman analyses, which reveal that introducing KOH to the Ni-metal catalyst in a one-pot system contributes significantly to reducing the carbon structural transformation temperature from amorphous to graphitic by a mechanism that will be described in detail in the next section.

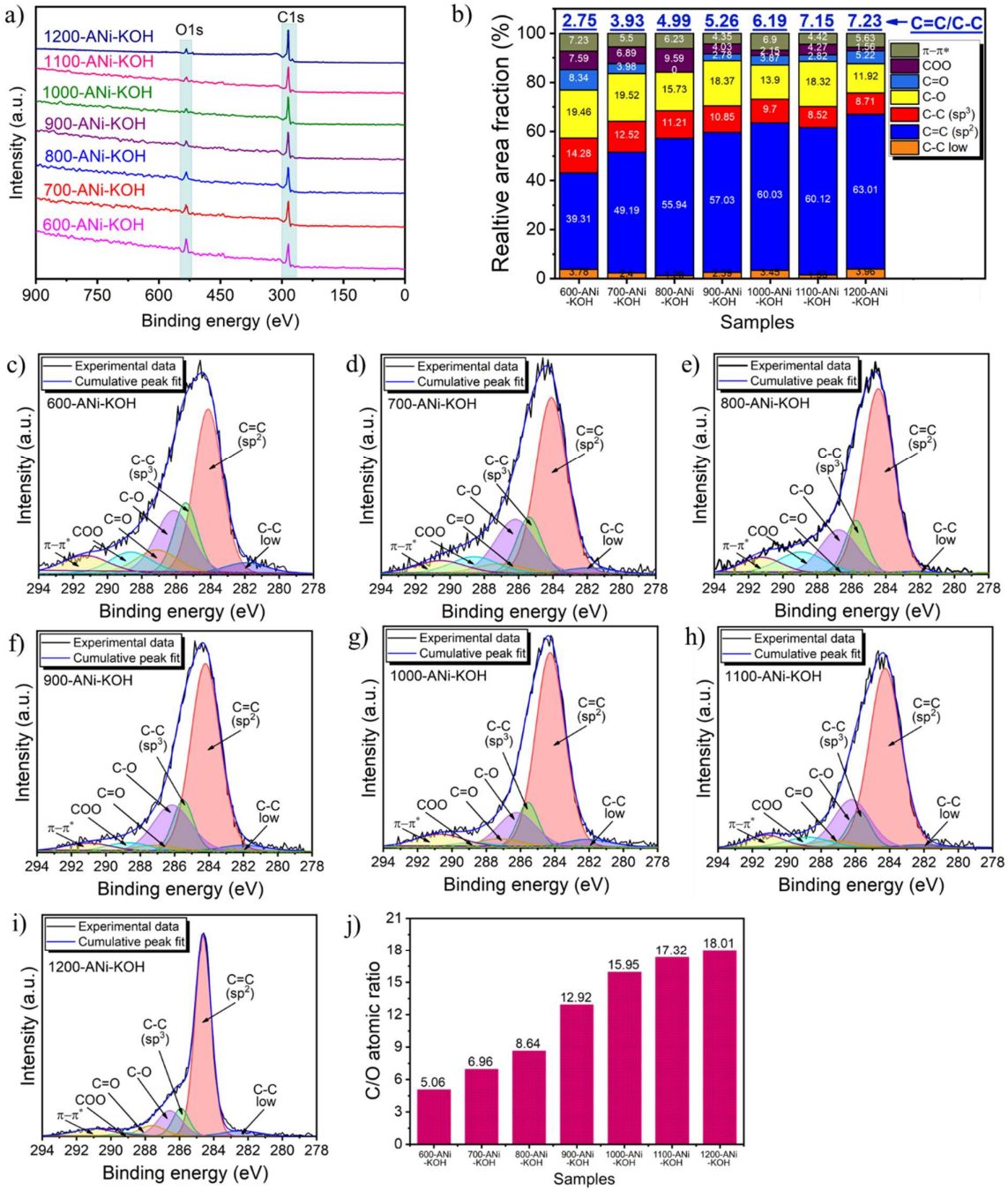

Figure 3-8. (a) XPS wide scan spectra, (b) Relative area fractions of deconvoluted C1s peak and C=C/C-C ratios of all samples. Deconvoluted XPS C1s peak for (c) 600-ANi-KOH, (d) 700-ANi-KOH (e) 800-ANi-KOH, (f) 900-ANi, (g) 1000-ANi-KOH, (h) 1100-ANi-KOH, (i) 1200-ANi-KOH, (j) C/O atomic ratio of all samples.

To validate the results of the abovementioned structural analysis, a transmission electron microscope (TEM) equipped with a selected area electron diffraction pattern (SAED) was applied to perform in-depth imaging observations on the samples prior to HCl washing. As can be seen in **Figure 3-9** samples pyrolyzed at 800 to 1200 °C demonstrated the presence of an ordered graph **Figure 3-9**itic region. In the low-magnification TEM images (**Figure 3-9**a, **Figure 3-9**d, **Figure 3-9**g, j, and **Figure 3-9**m), these structures can be observed as ribbon-like structures surrounding the Ni-nanoparticles (the dark-colored part). These ribbon-like structures show the well-defined lattice fringes when observed in more detail using HRTEM (**Figure 3-9**c, **Figure 3-9**f, **Figure 3-9**i, **Figure 3-9**l, and **Figure 3-9**o). The multilayer graphene sheets appear to be stacked in a planar arrangement with an inter-layer spacing of 3.3363–3.3526 Å, which is identified with graphitic carbon. These values appear to decrease with increasing pyrolysis temperature, getting closer to the inter-layer spacing value of commercial graphite. This trend is consistent with the results of the XRD analysis (**Figure 3-6**a). In addition, spot patterns observed on the SAED images (inset of **Figure 3-9**b, **Figure 3-9**e, **Figure 3-9**h, **Figure 3-9**k, and **Figure 3-9**n), confirming the formation of graphitic structure in these five samples. The results of this visual observation are in conformity with XRD, Raman, and XPS analysis, which demonstrate that the catalytic graphitization process combining KOH and Ni-based catalyst in a single pot system develops the graphitic structure with a major section starting at 800 °C.

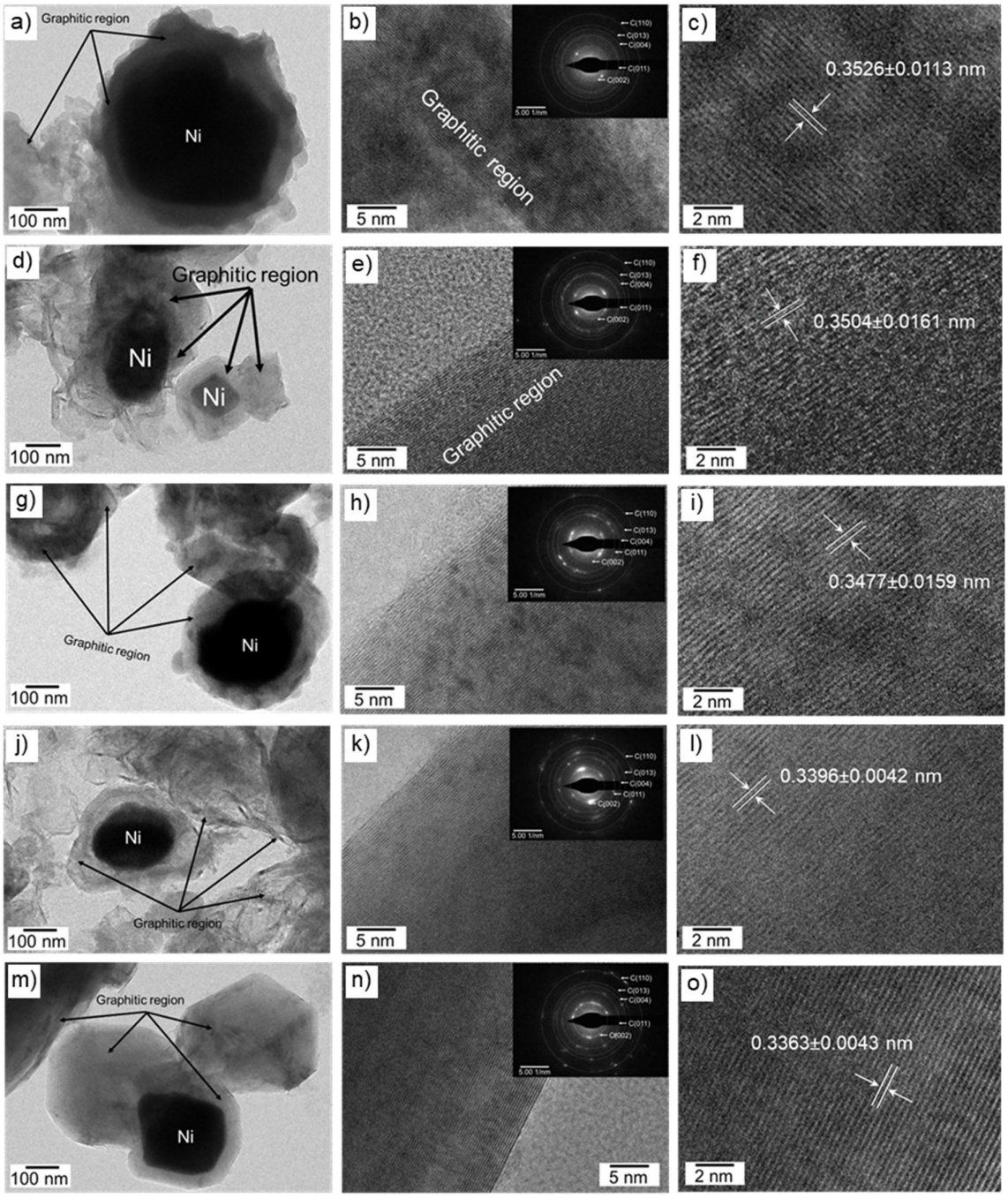

Figure 3-9. Low magnification TEM, HRTEM, and SAED images of Ni-KOH-treated samples pyrolyzed at (a-c) 800 °C, (d-f) 900 °C, (g-i) 1000 °C, (j-l) 1100 °C and (m-o) 1200 °C prior to HCl washing.

Textural properties analysis

Textural properties of Ni-KOH treated coconut coir carbon, including pore size and surface area in response to the pyrolysis temperature, was observed through the BET method. As seen in **Figure 3-10**(a-g), the shape of nitrogen adsorption−desorption isotherms graph of the obtained carbon samples changes with increasing pyrolysis temperature.

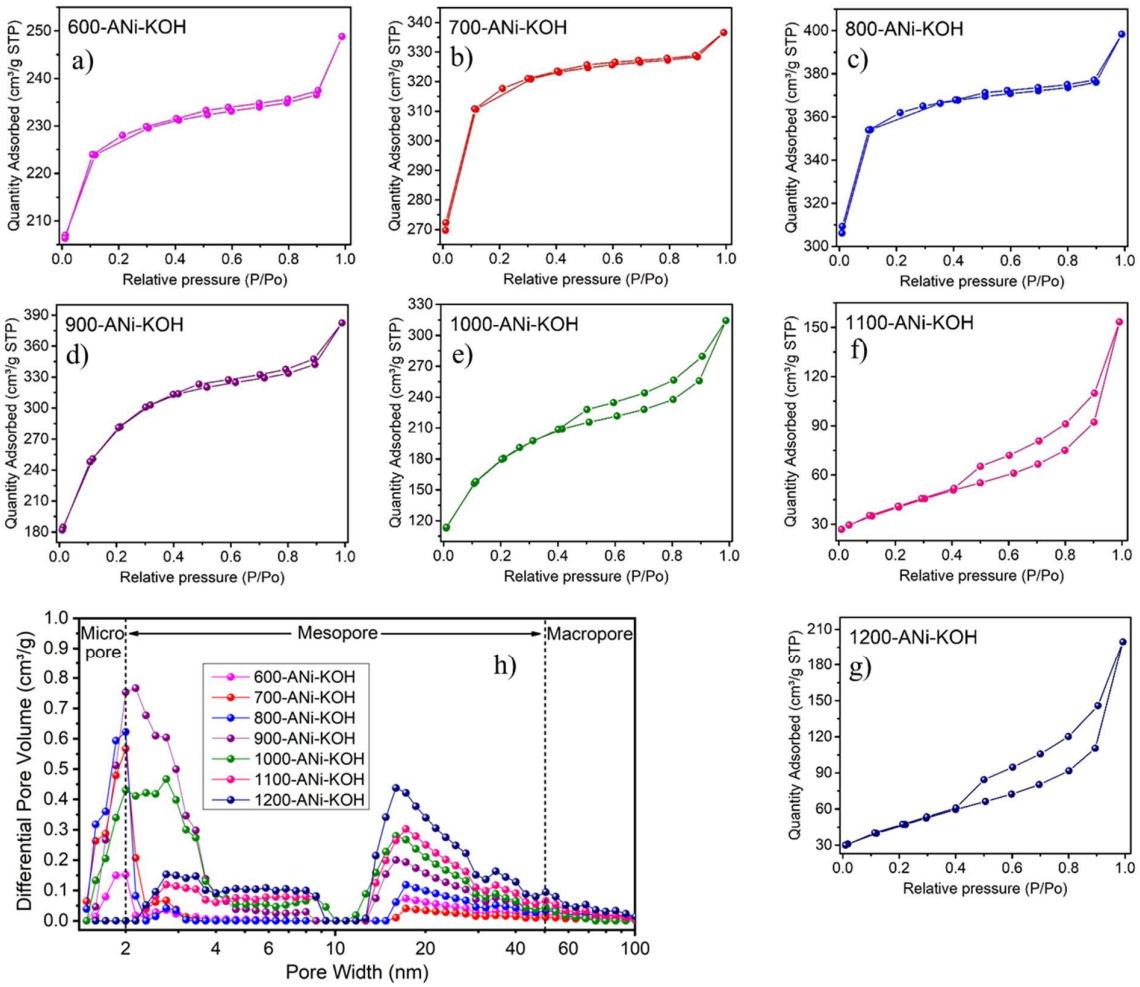

Figure 3-10. Nitrogen adsorption-desorption isotherms of (a) 600-ANi-KOH, (b) 700-ANi-KOH (c) 800-ANi-KOH, (d) 900-ANi, (e) 1000-ANi-KOH, (f) 1100-ANi-KOH, (g) 1200-ANi-KOH, and (h) pore size distribution of all samples.

According to IUPAC guidelines, samples pyrolyzed up to 800 °C (600-ANi-KOH to 800-ANi-KOH) exhibit a combination of Type I and Type IV. The steep rise in the relatively low-pressure area (P/Po < 0.1) and the appearance of a narrow hysteresis, indicate the presence of abundant micropores with few mesopores. Micropores were generated by the activation reaction between carbon and KOH which corrode the coconut coir carbon walls as shown in the SEM images in **Figure 3-11**(a-l), while Ni particles taken out of the sample leave space for mesopores to form. This reaction gradually increases the surface area and pore volume of carbon samples (**Table 3-1**). Then, as the temperature rises to 1000 °C, the hysteresis loop appearing at intermediate pressure section (0.4 < P/Po < 1) gets larger (**Figure 3-10**(d-e)), indicating an increase in mesopores but decreasing in micropores. However, when the temperature further increases up to 1200 °C, the isotherm graph of the samples changed to type IV (**Figure 3-10**(f-g)), suggesting the dominance of the mesopores over the micropores in the samples (**Figure 3-10**h). This can be driven by an increase in the diffusion rate of potassium ions at high temperatures, which accelerates the rate of the carbon-KOH reaction and leads to a greater consumption of carbon[30,31], subsequently reducing the specific surface area and pore volume. Furthermore, excessive collapse of the carbon skeleton, graphitization process, and carbon structural rearrangement at high temperatures that disrupts the microporous structure can also lead to a reduction in surface area and pore volume (**Table 3-1**)[32]. In this work, the pyrolysis process at a temperature of 800 °C produced a graphitic carbon sample (800-ANi-KOH) with the highest surface area and micropores (**Table 3-1**), as shown also by the dramatic increase in XRD diffraction intensity in the low angle region (**Figure 3-6**a).

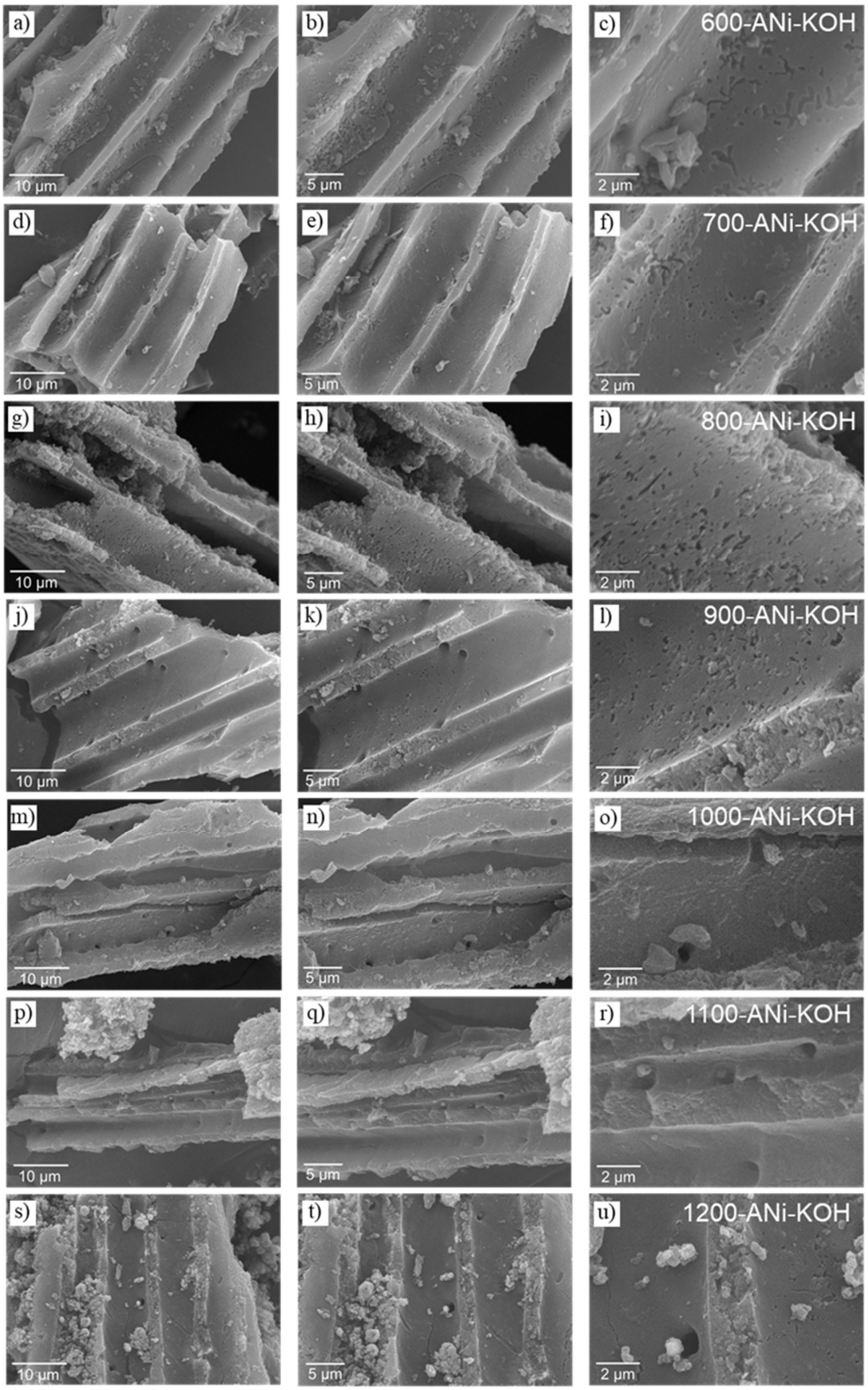

Figure 3-11. SEM image of (a-c) 600-ANi-KOH, (d-f) 700-ANi-KOH (g-i) 800-ANi-KOH, (j-l) 900-ANi, (m-o) 1000-ANi-KOH, (p-r) 1100-ANi-KOH, (s-u) 1200-ANi-KOH.

Table 3-1. Textural properties parameters of all samples.

Samples	Pore Volume (m^3/gr)				S_{BET}[e] (m^2/gram)	Av. pore width (nm)
	$V_{< 2nm}$[a]	$V_{< 50nm}$[b]	$V_{> 50nm}$[c]	V_{tot}[d]		
600-ANi-KOH	0.282 (89.9%)	0.028 (8.9%)	0.004 (1.3%)	0.313	694.280	2.308
700-ANi-KOH	0.392 (93.2%)	0.026 (6.1%)	0.003 (0.6%)	0.421	962.277	2.182
800-ANi-KOH	0.460 (90.8%)	0.040 (7.9%)	0.007 (1.3%)	0.506	1,043.820	2.419
900-ANi-KOH	0.284 (56.9%)	0.209 (41.8%)	0.007 (1.3%)	0.499	911.123	2.597
1000-ANi-KOH	0.163 (43.9%)	0.207 (55.5%)	0.002 (0.6%)	0.372	599.414	3.245
1100-ANi-KOH	0.036 (20.1%)	0.137 (77.3%)	0.005 (2.6%)	0.177	171.966	6.789
1200-ANi-KOH	0.024 (9.9%)	0.204 (84.7%)	0.013 (5.3%)	0.240	162.308	7.608

a represents micropore (d < 2 nm) pore volume calculated by DFT (slit pore model)
b represents mesopore (d < 50 nm) pore volume calculated by DFT (slit pore model)
c represents macropore (d > 50 nm) pore volume calculated by DFT (slit pore model)
d represents total DFT pore volume
e represents BET surface area

Graphitic and porous structure development mechanisms

The mechanism that occurs during the pyrolysis treatment has a significant impact on the structural and textural properties formed in the Ni-KOH-treated carbon samples. KOH acts as an activating agent with its well-known activation mechanism in creating porous structure. During the pyrolysis process, KOH interacts with carbon to produce potassium-based species such as potassium carbonate (K_2CO_3), potassium oxide (K_2O), and potassium metal (K), as well as volatiles including H_2, CO, H_2O, and CO_2. The resulting CO_2 and potassium-based species from Eq. 3-1 were capable of reacting with carbon (Eq. 3-2, Eq. 3-3, Eq. 3-4). By further reducing and sublimating potassium-based species with carbon and hydrogen, potassium metal is produced (Eq. 3-3, Eq. 3-5, Eq. 3-6). The metal potassium then intercalates within the carbon layer, expanding and rearranging it. These processes result in the development of pore

structures. In addition, as reported previously, the interaction between potassium metal and carbon also causes internal heating and localized graphitization during the pyrolysis process, which results in a small amount of graphitic structure[6,17,18].

$$K_2O + H_2 \rightarrow 2K + H_2O \quad (3\text{-}5)$$

$$K_2CO_3 + 2C \rightarrow 2K + 3CO \quad (3\text{-}6)$$

Meanwhile, Ni salts act as catalysts for the formation of graphitic structures on the coconut coir carbon. The graphitization process is typically preceded by the dehydration and decomposition of Ni salts into nickel oxide (NiO)[19], which is then reduced by amorphous carbon to form metallic Ni[33]. As a result of random diffusion and/or C-Ni interactions, the Ni particles move within the amorphous carbon matrix[20]. Amorphous carbon can readily dissolve and diffuse in Ni at a certain temperature, owing to the high solubility of carbon in Ni. As the C-Nisystem approaches a high level of saturation, carbon with a graphitic structure precipitate at the C–Ni interface due to the negative Gibbs free energy of graphite formation[34]. The solubility of carbon in Ni increases as pyrolysis temperature rises, resulting in a higher degree of graphitization as more amorphous carbon is converted to graphitic carbon[34].

Combining KOH and Ni-based catalysts in a one-pot system under the pyrolysis process leads the K and Ni metals to simultaneously interact with carbon to produce PGC. According to the findings of the structural analysis in the preceding section, the presence of KOH and Ni-based catalysts in one-pot catalyzed the graphitization process and reduced its initial temperature. This could be as a result of the synergistic interaction between K and Ni metals, which transformed the surrounding amorphous carbon into graphitic carbon and created the larger graphitic cluster. In addition, reducing gases resulting from the interaction of KOH and carbon, such as CO and H_2 (Eq. 3-1 to Eq. 3-6), can reduce nickel oxide via the reactions in equations 3-7 and 3-8[33], leading to the generation of more Ni metal that interacts with carbon to develop more graphitic clusters.

$$NiO + CO \rightarrow Ni + CO_2 \quad (3\text{-}7)$$

$$NiO + H_2 \rightarrow Ni + H_2O \quad (3\text{-}8)$$

As aforementioned, the role played by K and Ni metals leads to a porous and graphitic structure in carbon materials that exhibits contradicting trends as pyrolysis temperatures increase. A graphitic structure with a higher degree of graphitization can be generated at a higher pyrolysis temperature, however this results in a decrease in surface area. Furthermore, this work found that 1000 °C is optimal pyrolysis temperature for producing porous graphitic carbon material (1000-ANi-KOH) with a balanced level of graphitization (IG/ID = 1.66) and pore structure (S_{BET} = 599.414 m^2/gram).

3.3.3. Electrochemical Behavior Analysis as Anode of LIBs

The microstructure and graphitic arrangement of materials are known to have a significant impact on the electrochemical performance of carbon as an anode of LIB[35]. Furthermore, the electrochemical performance of coconut coir carbon samples treated with Ni-KOH at different temperatures were investigated by conducting electrochemical analysis using charge-discharge (CD) and cyclic voltametric (CV) test in a half-cell configuration with a Li counter electrode. CD curves for the first three cycles of all samples at a current rate of 0.05C are depicted in **Figure 3-12**(a-e). There was an irreversible loss of capacity in the initial cycle for all samples, indicated by the low initial Columbic efficiency (ICE). This behavior could be attributed to the anode material surface area of the electrode active material (**Table 3-1**). The high specific surface area of the electrode active material could increase the side reactions at the electrode-electrolyte solution interface, consuming more irreversible Li^+ ions to form a more solid electrolyte interface (SEI) and decreasing the initial coulombic efficiency[31,36]. The results of the CD curve analysis show that a higher pyrolysis temperature leads to a higher ICE value, which were 22.93%, 33.44%, 45.13%, 49.99%, and 51.39% for samples 800-ANi-KOH, 900-

ANi-KOH, 1000-ANi-KOH, 1100-ANi-KOH, and 1200- ANi-KOH, respectively, as an effect of decreasing the surface area of the anode material. As **Figure 3-12** shows, pyrolysis temperature also affects the shape of the CD curve. The 800-ANi-KOH sample, which has the lowest degree of graphitization and highest surface area, exhibits a sloping profile with a less obvious plateau profile in the low voltage region (<0.25 V vs Li/Li^+) of the CD curve (**Figure 3-12**a). A sloping profile is generated as a result of the disordered structure of carbon, which provides the electronically and geometrically nonequivalent sites, such as defect, edge, pores, and surface for Li^+ ion storage process[32,37]. Whereas the ordered carbon structure, indicated by a high degree of graphitization, provides equivalent sites for Li^+ ion to be stored, generating in a plateau profile[37]. Furthermore, samples obtained at higher temperatures (900-ANi-KOH to 1200-ANi-KOH) with higher degrees of graphitization and lower surface areas show a more distinct plateau profile appearance (**Figure 3-12**(b-e)). The 1000-ANi-KOH delivers the highest reversible capacity of 451.83 mAh/gr. The higher capacity of the 1000-ANi-KOH is associated with the appropriate surface area as well as the degree of graphitization, which allows more Li^+ ions to be stored. The derivative dQ/dV curves depicted in **Figure 3-12**(f-k) are used to clarify the Li^+ ion storage mechanism in this work. It clearly shows that all samples possess several anodic peaks in the plateau region (<0.25 V vs Li/Li^+), indicating the existence of graphitic structures as lithiation/delithiation processes at this site occur at very low potentials[38,39]. Whereas the role of the pore structure with large surface area of samples 800-ANi-KOH, 900-ANi-KOH, and 1000-ANi-KOH in providing Li^+ ion storage sites can be seen from the larger area inside the curve in the sloping region (0.25-3 V vs Li/Li^+) compared to samples 1100-ANi-KOH and 1200-ANi-KOH.

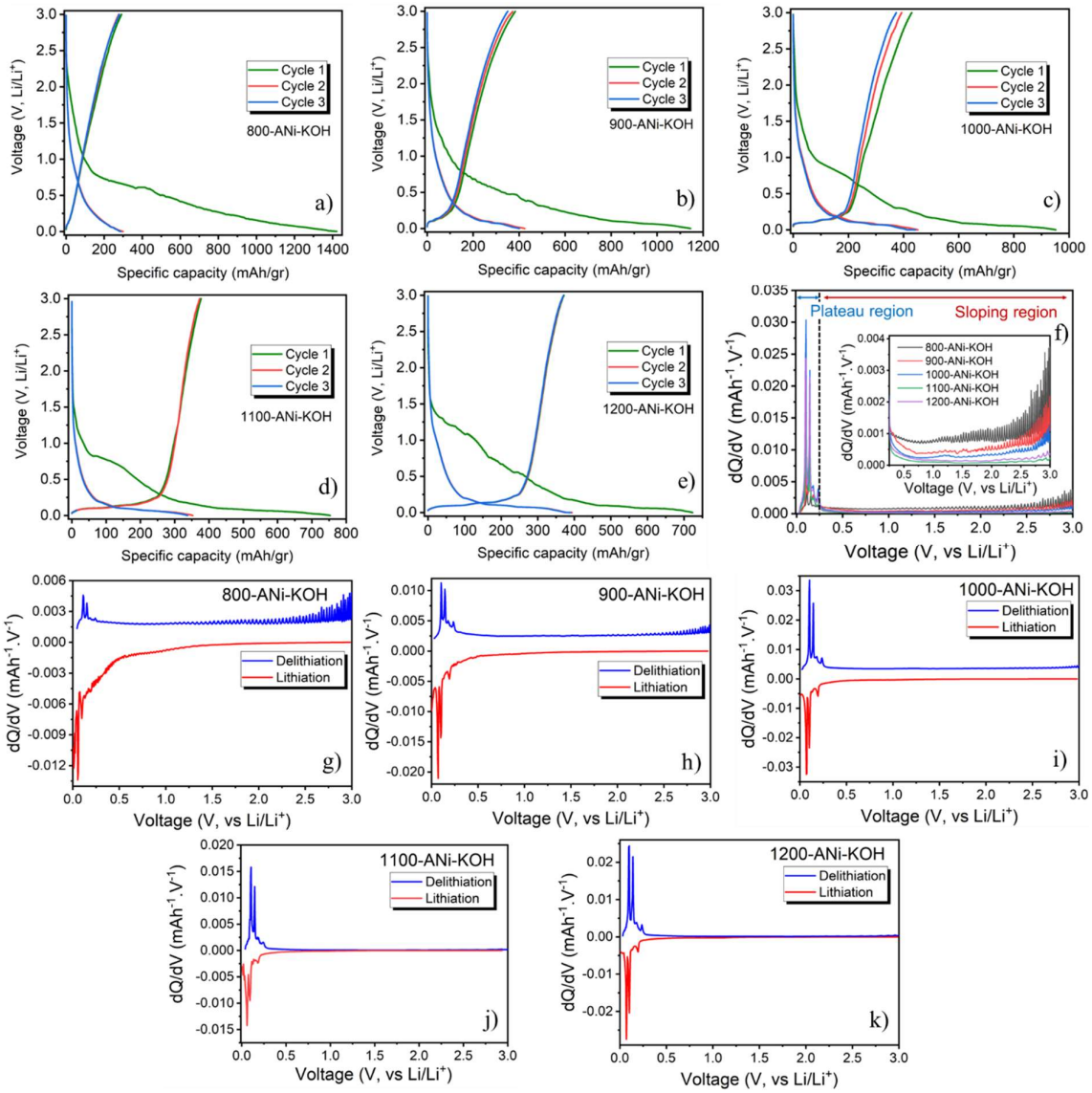

Figure 3-12. Charge−discharge plots for cycles 1, 2, and 3 for (a) 800-ANi-KOH, (b) 900-ANi-KOH, (c) 1000-ANi-KOH, (d) 1100-ANi-KOH, (e) 1200-ANi-KOH, (f) dQ/dV plot of the 2nd cycle delithiation process of all sample electrodes at 0.05C (0.0001–3.00 V, vs. Li/Li^{+}). dQ/dV plot of the 2nd cycle lithiation-delithiation process of (g) 800-ANi-KOH, (h) 900-ANi-KOH, (i) 1000-ANi-KOH, (j) 1100-ANi-KOH, (k) 1200-ANi-KOH in LIBs

In order to comprehend the Li^{+} ion storage mechanism in t-ANi-KOH samples with varying graphitic structural ordering and surface area, CVs were recorded at increasing scanning rates (0.1– 1 mV/s) over a potential range of 0.001–2.5 V. As seen in **Figure 3-13**(a-

e), the current responses of all electrode samples tend to rise but maintain a consistent shape as the scanning rates increase, indicating a good rate capability[40] and kinetic reversibility[41] of the electrode material. The Li^+ ion storage mechanisms were evaluated according to the relationship of $i = av^b$, where i represents the peak current, v the CV scan rate, and b the charge storage kinetics within the electrode[42]. The slope of the linear fit plot of log i vs log v at a fixed potential (**Figure 3-13**f) was used to determine the b values (inset of **Figure 3-13**f) of all electrode samples. As the pyrolysis temperature of the sample increases, the b value approaches 0.5, as in samples 1100-ANi-KOH and 1200-ANi-KOH with b values of 0.56 and 0.62, suggesting that the sample shows progressively dominant diffusion charge storage (Li^+ ion store in the graphitic interlayer storage sites) due to a more ordered graphitic structure and a decreased surface area. Conversely, samples obtained at lower pyrolysis temperatures such as 800-ANi-KOH (0.96) showed b values close to 1, signifying that the samples exhibited increasingly dominant capacitive charge storage (Li^+ ion store in the micropore surface, defect, and edges storage sites) owing to their larger surface area[31] and the smallest graphitization degree. Meanwhile, the b values of 900-ANi-KOH and 1000-ANi-KOH are between 0.5 and 1, which are 0.88 and 0.90, respectively, indicating that they behave as a combination of diffusive and capacitive charge storage as a result of the presence of graphitic structure and moderate surface area. This finding is consistent with the results of XRD, Raman, TEM, and BET structural analyses. Furthermore, the capacitance and diffusion contributions to the electrode samples were identified using the following formula: $i = k_1 v + k_2 v^{1/2}$ [42]. The percentage of capacitive and diffusion charge storage obtained from calculating the slope (k_1) and Y-intercept (k_2) of the plot $i(V)/v^{1/2}$ vs $v^{1/2}$ at a specific potential is shown in **Figure 3-13**g. The percentage contribution of capacitive charge storage is seen to increase with an increasing scan rate. In line with the b value analysis, 800-ANi-KOH exhibited a capacitive contribution dominating at all scan rates, with values increasing from 75% at 0.1 mV/s to 90% at 1 mV/s. For 900-ANi-KOH

and 1000-ANi-KOH samples showed nearly equal contribution between capacitive and diffusive charge storage at low scan rates. However, at a high scan rate of 1 mV/s, capacitive charge storage tended to be dominant due to their moderate surface area. In the meanwhile, samples 1100-ANi-KOH and 1200-ANi-KOH confirmed that the diffusive charge storage contributed dominantly to all scan rates due to their high graphitic structure.

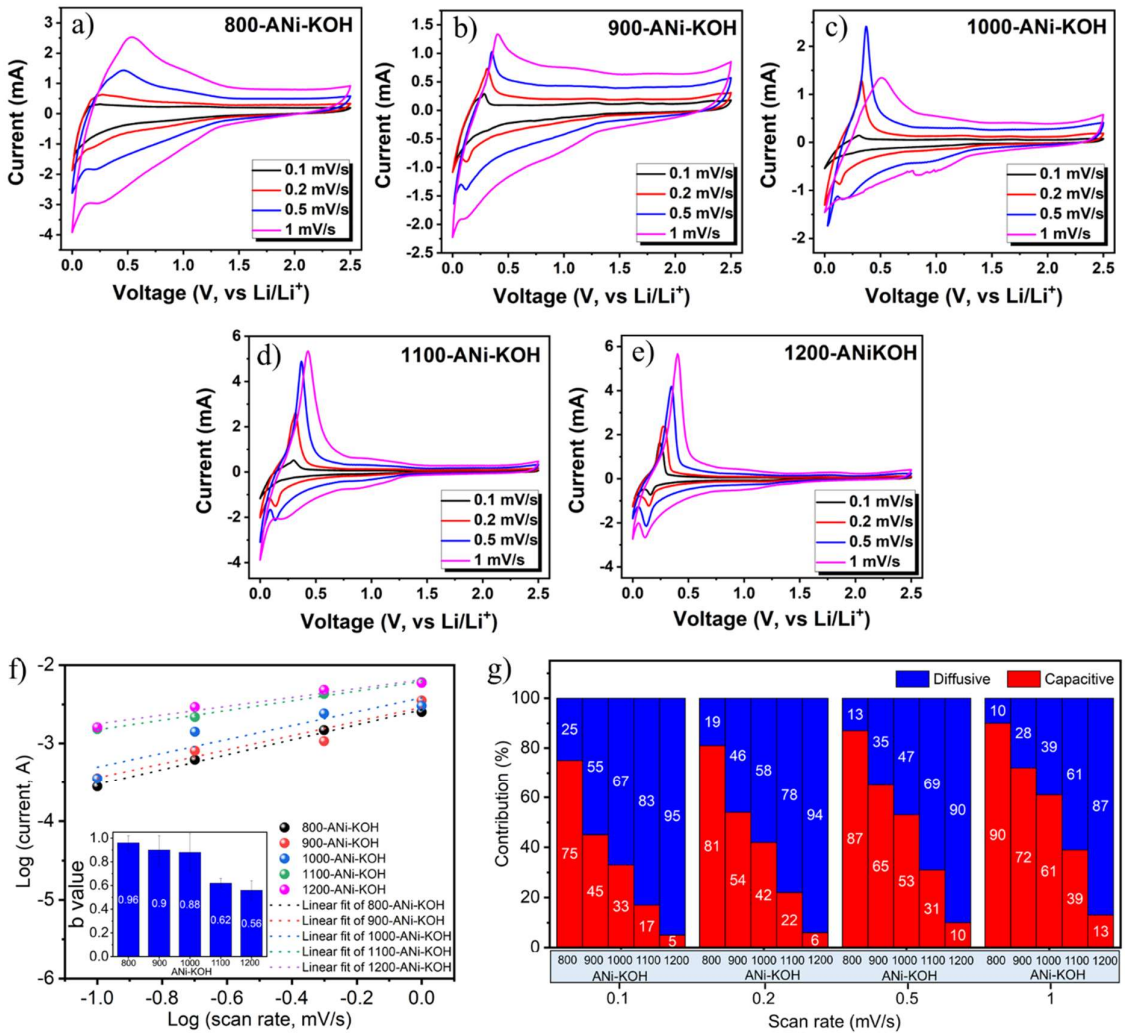

Figure 3-13. CV curves at various scan rates from 0.1 to 1.0 mV/s for (a) 800-ANi-KOH, (b) 900-ANi-KOH, (c) 1000-ANi-KOH, (d) 1100-ANi-KOH, (e) 1200-ANi-KOH in LIBs. (f) Relationship between log (i) and log (v) plots (inset is the b value); and (g) Contribution ratios of the diffusive and capacitive-based capacities vs scan rate of all electrodes in LIBs.

Rate performance at increasing current rates (0.05 - 1C) and cycling stability at a constant rate (0.5C) throughout a voltage range of 0.001-3.00 V vs Li/Li^+ were also carried out to further analyze the electrochemical performance of all carbon electrodes. In **Figure 3-14**a, the specific capacity of all samples decreased with increasing current density owing to diffusion limitation of the ions in the electrolyte and not having enough time to reach all the storage site of the carbon electrodes at high current densities. The specific capacity of each sample then almost recovered to its initial specific capacity when its current density was restored to 0.05C, indicating good electrochemical reversibility. The 1000-ANi-KOH electrode demonstrated the highest specific capacity in almost all current rates when compared to the carbon samples obtained at other temperatures. This can be attributed to the unique hybrid properties of its high degree of graphitic structure and balanced micro-mesoporous structures. The above hybrid characteristic provides more storage sites for lithium-ions and enhances electron/ion transfer at the electrodes, making the anode material have good rate performance. In contrast, the 800-ANi-KOH sample had the lowest specific capacity at almost all current rates. This can be attributed to the graphitization degree of this sample (IG/ID) is the lowest compared to the other electrodes, limiting the amount of storage sites available in the graphitic interlayer. The durability of all carbon electrodes was further evaluated at a constant rate of 0.5 C. After 150 cycles, the cycling performance and Coulombic efficiency are displayed in **Figure 3-14**b and **Figure 3-14**c, respectively. The 1000-ANi-KOH sample also appears to have the highest reversible capacity among the other samples, reaching 273.24 mAh/gram and a capacity retention ratio of 85.2%. Thus, the 1000-ANi-KOH is considered as the carbon material that has the most optimal properties for LIB anodes. Then, sample 1200-ANi-KOH is in the next order with a reversible capacity of 165.76 mAh/gram and a retention ratio of 93%, and followed by samples of 1100-ANi-KOH, 900-ANi-KOH, and 800-ANi-KOH with a reversible capacity of 102.94 mAh/gram (91.1%), 91.42 mAh/gram (86.3%), and 90.45 mAh/gram (82%),

respectively. **Figure 3-14**c depicted that the 800 ANi-KOH sample has the lowest initial coulombic efficiency (19.9%), and this value increases with increasing pyrolysis temperature, reaching 40.49% for the 1200 ANi-KOH sample. These results are in agreement with those of the CD test performed at a low current rate of 0.05C.

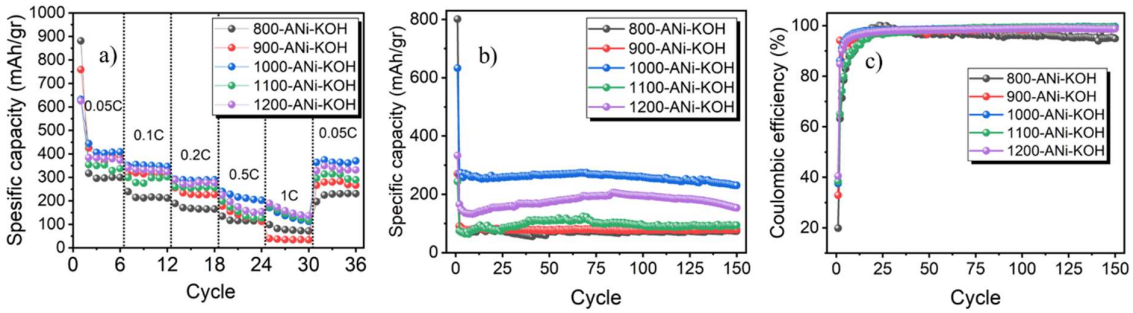

Figure 3-14. (a) C-rate performance of all samples at increasing current densities from 0.05C to 1C, then back to 0.05C to demonstrate rate capability, (b) cycling performance and (c) Coulombic efficiency at 0.5C current density for 150 cycles (1C=372 mA/g).

3.4. Conclusions

In conclusion, combining KOH chemical activation and Ni-based catalytic graphitization in a one-pot process produces porous graphitic carbon material from coconut coir with the highest degree of graphitization compared to other treatments. The synergistic effect of K and Ni metal interaction with amorphous carbon promotes internal heating and catalytic graphitization, resulting in an ordered carbon structure and increased graphitic area. Ion diffusion in the graphite interlayer serves as the dominant ion storage mechanism for the 1200-ANi-KOH sample, comparable to commercial graphite. This simple fabrication method combining KOH and Ni-based catalytic graphitization enhances the performance of coconut coir as a Li-ion battery anode. Furthermore, we also found that the pyrolysis temperature affects the development of porous and graphitic structures. The degree of graphitization increases with higher pyrolysis temperatures, facilitated by enhanced carbon solubility in Ni. However,

specific surface area and pore volume decrease at temperatures above 800 °C due to disruptions in the microporous structure caused by increased potassium ion diffusion rates, carbon skeleton collapse, and structural rearrangement. Optimizing the pyrolysis temperature at 1000 °C yields porous graphitic carbon material with a balanced graphitization degree (IG/ID = 1.66) and pore structure (S_{BET} = 599.414 m^2/gram). As anodes in Li-ion batteries, these materials demonstrate good electrochemical performance, with the 1000-ANi-KOH sample exhibiting the highest reversible capacity of 451.83 mAh/g at 0.05 C due to its high-order graphitic structure and surface area. This work presents a straightforward and efficient method to convert coconut coir waste into a porous graphitic carbon material at lower temperatures, offering excellent potential as a Li-ion battery anode.

3.5. References

[1] C. N. Barnakov, G. P. Khokhlova, A. N. Popova, S. A. Sozinov, Z. R. Ismagilov, *Eurasian Chem. J.* **2015**, *17*, 87–93.

[2] M. W. Smith, I. Dallmeyer, T. J. Johnson, C. S. Brauer, J. S. McEwen, J. F. Espinal, M. Garcia-Perez, *Carbon N. Y.* **2016**, *100*, 678–692.

[3] F. Destyorini, Y. Irmawati, A. Hardiansyah, H. Widodo, I. N. D. Yahya, N. Indayaningsih, R. Yudianti, Y. I. Hsu, H. Uyama, *Eng. Sci. Technol. an Int. J.* **2020**, *24*, 514–523.

[4] D. B. Schuepfer, F. Badaczewski, J. M. Guerra-Castro, D. M. Hofmann, C. Heiliger, B. Smarsly, P. J. Klar, *Carbon N. Y.* **2020**, *161*, 359–372.

[5] J. R. Dennison, M. Holtz, *Spectroscopy* **1996**, *11*, 38–46.

[6] Kovummal Govind Raj, P. A. Joy, *J. Am. Ceram. Soc.* **2017**, *100*, 5151–5161.

[7] M. M. Gaikwad, C. S. Sharma, *J. Mater. Res.* **2020**, *35*, 2989–3003.

[8] C. Hu, S. Sedghi, A. Silvestre-albero, G. G. Andersson, A. Sharma, P. Pendleton, F. Rodrı, M. J. Biggs, *Carbon N. Y.* **2015**, *85*, 147–158.

[9] S. Zhang, Q. Liu, H. Zhang, R. Ma, K. Li, Y. Wu, B. J. Teppen, *Carbon N. Y.* **2020**, *157*, 714–723.

[10] A. Fujimoto, Y. Yamada, M. Koinuma, S. Sato, *Anal. Chem.* **2016**, *88*, 6110–6114.

[11] M. Smith, L. Scudiero, J. Espinal, J. S. McEwen, M. Garcia-Perez, *Carbon N. Y.* **2016**, *110*, 155–171.

[12] T. Nunney, R. White, *Micros. Today* **2011**, 22–29.

[13] Q. Chen, X. Tan, Y. Liu, S. Liu, M. Li, Y. Gu, P. Zhang, S. Ye, Z. Yang, Y. Yang, *J. Mater. Chem. A* **2020**, *8*, 5773–5811.

[14] M. Shi, C. Song, Z. Tai, K. Zou, Y. Duan, X. Dai, J. Sun, *Fuel* **2021**, *292*, 120250.

[15] K. H. Ko, T. J. Park, V. Sahajwalla, A. Rawal, *Fuel* **2021**, *291*, 120153: 1–14.

[16] J. Wang, S. Kaskel, *J. Mater. Chem.* **2012**, *22*, 23710–23725.

[17] K. Liu, J. Zhang, R. Ding, X. Zheng, T. Yang, C. Wang, M. Chen, *Carbon N. Y.* **2019**, *155*, 326–333.

[18] K. W. McNamara, P. Ayyappan, R. Rajagopalan, J. G. Chen, H. C. Foley, *Carbon N. Y.* **2013**, *56*, 109–120.

[19] S. K. Mishra, S. B. Kanungo, *J. Therm. Anal.* **1992**, *38*, 2417–2436.

[20] R. Anton, *Carbon N. Y.* **2008**, *46*, 656–662.

[21] T. Kim, J. Lee, K. H. Lee, *RSC Adv.* **2016**, *6*, 24667–24674.

[22] Y. Kodama, K. Sato, K. Suzuki, Y. Saito, T. Suzuki, T. J. Konno, *Carbon N. Y.* **2012**, *50*, 3486–3496.

[23] Q. Yan, J. Li, X. Zhang, E. B. Hassan, C. Wang, J. Zhang, Z. Cai, *J. Nanoparticle Res.* **2018**, *20*, 1–20.

[24] Y. Shu, J. Maruyama, S. Iwasaki, C. Li, Y. Shen, H. Uyama, *Bull. Chem. Soc. Jpn.* **2017**, *90*, 1058–1066.

[25] F. Destyorini, W. C. Amalia, Y. Irmawati, A. Hardiansyah, S. Priyono, F. Aulia, H. S. Oktaviano, Y. I. Hsu, R. Yudianti, H. Uyama, *Energy and Fuels* **2022**, *36*, 5444–5455.

[26] A. C. F. and J. Robertson, *Phys. Rev. B* **2000**, *61*, 632–645.

[27] Y. Eom, S. M. Son, Y. E. Kim, J. E. Lee, S. H. Hwang, H. G. Chae, *Carbon N. Y.* **2019**, *150*, 142–152.

[28] M. Sevilla, A. B. Fuertes, *Chem. Phys. Lett.* **2010**, *490*, 63–68.

[29] X. Zhang, K. Zhang, H. Li, Q. Wang, L. Jin, Q. Cao, *J. Appl. Electrochem.* **2018**, *48*, 415–426.

[30] A. C. Lua, T. Yang, *J. Colloid Interface Sci.* **2004**, *274*, 594–601.

[31] X. Liu, H. Tao, C. Tang, X. Yang, *Chem. Eng. Sci.* **2022**, *248*, 117200.

[32] L. Han, X. Zhu, F. Yang, Q. Liu, X. Jia, *Powder Technol.* **2021**, *382*, 40–47.

[33] H. Rastegar, E. Mansorizadeh, *Carbon Lett.* **2022**, *32*, 835–848.

[34] S. Khoshk Rish, A. Tahmasebi, R. Wang, J. Dou, J. Yu, *Diam. Relat. Mater.* **2021**, *120*, 108699.

[35] M. P. Illa, C. S. Sharma, M. Khandelwal, *Mater. Today Chem.* **2021**, *20*, 100439.

[36] V. Etacheri, C. Wang, M. J. O'Connell, C. K. Chan, V. G. Pol, *J. Mater. Chem. A* **2015**, *3*, 9861–9868.

[37] A. Shellikeri, V. Watson, D. Adams, E. E. Kalu, J. A. Read, T. R. Jow, J. S. Zheng, J. P. Zheng, *J. Electrochem. Soc.* **2017**, *164*, A3914–A3924.

[38] T. Kim, C. Jo, W. G. Lim, J. Lee, J. Lee, K. H. Lee, *Carbon N. Y.* **2016**, *104*, 106–111.

[39] H. S. Oktaviano, K. Waki, *J. Electrochem. Soc.* **2016**, *163*, A442–A446.

[40] Y. S. Choudhary, L. Jothi, G. Nageswaran, *Electrochemical Characterization*, Elsevier Inc., **2017**.

[41] K. Wang, Y. Xu, H. Wu, R. Yuan, M. Zong, Y. Li, V. Dravid, W. Ai, J. Wu, *Carbon N. Y.* **2021**, *178*, 443–450.

[42] D. Qiu, C. Kang, M. Li, J. Wei, Z. Hou, F. Wang, R. Yang, *Carbon N. Y.* **2020**, *162*, 595–603.

Concluding Remarks

In this dissertation, several facile and efficient synthesis approaches are described for converting coconut coir, an Indonesian biomass waste that has not been utilized optimally, into cost-effective and sustainable functional carbon materials. These materials pose promising potential for applications in energy conversion and storage fields. The electrochemical performance of the developed carbon materials was carefully evaluated, with a specific focus on their performance as electrodes in PEMFC and LIB. The findings obtained from this dissertation can be summarized as follows.

In Chapter 1, an innovative and practical approach is presented to convert coconut coir into carbon functional materials that are suitable for use as electrodes in PEMFCs. Carbon materials utilized in this study were obtained through direct pyrolysis process of coconut coir and were subsequently employed in the fabrication of conductive carbon composite paper. Combinations of 70 wt% carbon fibers and 10 wt% carbon powder achieved an optimal composition notably the highest electrical conductivity, reaching 2.22 S/cm. However, CCP-8 shows slightly lower cell performance compared to CCP-1, wherein CCP-1 did not contain carbon fiber. It is important to highlight that, for GDL, apart from electrical conductivity, the surface roughness and pore size also contribute greatly to the cell performance. Low surface roughness with small pores prevents the catalyst ink from spreading into pores of the carbon paper, which reduces the contact resistance between the catalyst layer and GDL and blocking gas distribution into GDL matrixes. There is a good relationship between electrical properties and morphological surface characteristics of biomass-based functional carbon materials for PEMFC GDL performance.

Subsequently, in Chapter 2, a comprehensive study to explore structural performance of carbon material is introduced as further strategy for next stage functional carbon application. This strategy employs a Ni-based catalytic graphitization process, which exhibits outstanding efficiency in producing graphite nanostructures at relatively lower temperatures compared to conventional graphitization methods. As a result, this strategy not only contributes to energy savings but also ensures a more efficient and simpler production process. By implementing this advanced process, the transformation of the amorphous carbon structure occurs at an initial temperature of 1200 °C for three hours, resulting in a well-ordered graphitic structure. This strategic intervention significantly enhances the structural integrity and crystalline arrangement of the carbon material, leading to improvements in electrical conductivity. Moreover, the graphitic carbon sample demonstrates great potential as an anode material for lithium-ion batteries (LIBs), exhibiting a specific capacity of 192.6 mAh/g at a current density of 0.05C, excellent cycling stability, and outstanding rate performance which have an impact on the overall LIB performance.

Expanding upon these achievements, Chapter 3 focuses on further exploring structural properties aimed at refining the properties and incorporating additional features into carbon materials. In this chapter, a combined approach utilizing Ni-based catalyst and KOH in a one-pot graphitization process is employed to elevate the graphitization degree and develop a porous structure, resulting in the production of porous graphitic carbon materials. The synergistic interaction between K and Ni metals with the amorphous carbon generates internal heating and catalytic graphitization, respectively. Both interactions boost the formation of a high degree of graphitization with a large surface area. This synergistic interaction also initiates the formation of an early-stage graphitic structure at a relatively lower temperature, around 800 °C, promoting the growth of larger graphitic clusters. Moreover, the reactions between K metal and carbon generate porous structures, that offer increased surface area for effective site of Li-ion as Li-

ion storage system. The unique characteristics of porous graphitic carbon offer an advantageous and efficient pathway for Li-ion and electron transport, resulting in increased active sites for Li-ion storage and enhanced performance. The incorporation of the Ni-KOH reaction in the one-pot graphitization process has proven to be a highly effective and energy-efficient method for converting coconut coir waste into a porous graphitic material suitable for LIB anodes.

All of the statements describe the presence of prospective technology for biomass conversion into functional carbon material as new insight on shifting technology from fossil based to biobased resources. The valorization of biomass waste plays a pivotal role in unlocking significant value from this resource, elevating it from a mere byproduct to a valuable commodity. This approach not only addresses environmental concerns by providing an eco-friendly waste management solution but also creates economic opportunities and reduced reliance on fossil-based resources. Furthermore, this research opens doors to further exploration and utilization of agricultural waste as a valuable resource for the development of functional carbon materials in the pursuit of sustainable energy solutions.

List of Publications

1. Preparation and characterization of carbon composite paper from coconut coir for gas diffusion layer.

   Fredina Destyorini, Achmad Subhan, Nanik Indayaningsih, Bambang Prihandoko, Anne Zulfia Syahrial

   International Journal of Technology, **2016**, 8, 1283-1290

   https://doi.org/10.14716/ijtech.v7i8.6888

2. Properties and performance of gas diffusion layer PEMFC derived from coconut coir.

   Fredina Destyorini, Yuyun Irmawati, Henry Widodo, Deni Shidqi Khaerudini, Nanik Indayaningsih

   Journal of Engineering and Technological Sciences, **2018**, 50, 3, 409-419

   https://doi.org/10.5614/j.eng.technol.sci.2018.50.3.7

3. Formation of nanostructured graphitic carbon from coconut waste via low-temperature catalytic graphitization.

   Fredina Destyorini, Yuyun Irmawati, Andri Hardiansyah, Henry Widodo, Ilham Nur Dimas Yahya, Nanik Indayaningsih, Rike Yudianti, Yu-I Hsu, Hiroshi Uyama

   Engineering Science and Technology, an International Journal, **2021**, 24, 514–523

   https://doi.org/10.1016/j.jestch.2020.06.011

4. Temperature driven structural transition in the nickel-based catalytic graphitization of coconut coir.

   Fredina Destyorini, Rike Yudianti, Yuyun Irmawati, Andri Hardiansyah, Yu-I Hsu, Hiroshi Uyama

   Diamond & Related Materials, **2021**, 117, 108443

   https://doi.org/10.1016/j.diamond.2021.108443

5. High graphitic carbon derived from coconut coir waste by promoting potassium hydroxide in the catalytic graphitization process for lithium-ion battery anodes.

   Fredina Destyorini, Windi Cahya Amalia, Yuyun Irmawati, Andri Hardiansyah, Slamet Priyono, Fauzan Aulia, Haryo S Oktaviano, Yu-I Hsu, Rike Yudianti, Hiroshi Uyama

   ACS Energy & Fuels, **2022**, 36, 10, 5444–5455

   https://doi.org/10.1021/acs.energyfuels.2c00632

6. Porous graphitic carbon from coconut coir biochar developed by Ni-KOH reaction for lithium-ion battery anodes.

   Fredina Destyorini, Slamet Priyono, Haryo S Oktaviano, Yu-I Hsu, Rike Yudianti, Hiroshi Uyama

   Waste Biomass Valorization (2023).

   https://doi.org/10.1007/s12649-023-02343-w

Acknowledgements

I express my deepest appreciation to my Japanese supervisor, Prof. Dr. Hiroshi Uyama, and Indonesian supervisor, Prof. Dr. Rike Yudianti. Their guidance was very meaningful, providing very valuable knowledge and experience for me during my five years as a JSPS RONPAKU (Dissertation PhD) Program fellow.

I am grateful for the chance to pursue graduate studies at Osaka University and the financial support provided by the Japan Society for the Promotion of Science RONPAKU (Disertation PhD). Additionally, I would like to express my gratitude to the Indonesian Institute of Sciences (LIPI), which is currently the National Research and Innovation Agency (BRIN), for providing me with facilities and research opportunities throughout my PhD program.

I am also indebted to Associate Prof. Yu-I Hsu and Assistant Prof. Akihide Sugawara for their insightful guidance and advice. My profound gratitude is extended to Ms. Yoko Uenishi and Ms. Tomoko Shimizu for their dedicated assistance as secretaries of the Uyama Laboratory.

I express my gratitude to all of the Uyama Laboratory's members, both past and present. Most notably, I would like to say special thanks to: Dr. Yankun Jia, Dr. Naharullah Bin Jamaluddin, Dr. Mark Adam Malaluan Ferry, Airi Ozaki, Dr. Toshiki Tamiya, Dr. Shunsuke Mizuno, Dr. Masatoshi Kato, Dr. Raghav Soni, Dr. Hanyu Wen, Yuka Kashihara, Dr. Yuxiang Jia, Dr. Nontarin Roopsung, Izzah Durrati, Madhurangika Panchabashini Horathal Pedige, Binti Haji Abdul, Emil Hajili, Kazuki Shibasaki, Sooyeon Noh, May Myat Noe, Hasinah binti Mohamed Rafiq, An Thuy Le Huynh, Rika Onishi, Judit Rebeka Molnar, and Qolby Sabrina.

The most special tributes are given to my supporting husband, Rully Sugiharto, and our two adorable children, Narasatya Zaffar Sugiharto and Nazafarin Zaffira Sugiharto. It would

not have been possible to finish this PhD degree without their consistent encouragement and support. Furthermore, I would like to thank Joko Setyono & Tri Widiantini (parents), Tondo Sugiharto & Lilik Suprijati (parents-in-law), my siblings: Weida Fredika Setiawan, Fredita Agustina & Fredian Muktiestri, siblings-in-law, nieces, and nephews. Their good support and motivation are the main factors for me to keep moving forward and complete my doctoral study here, at Osaka University. I love you with all. Alhamdulillah.

Fredina Destyorini
December 2023